University of Genoa

School of Mathematical, Physical and Natural Sciences

This dissertation is submitted for the degree of Doctor of Philosophy in Material Science and Technology
Ph.D. cycle XXXV

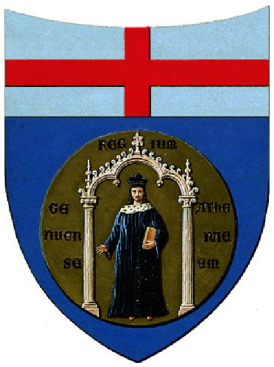

Development of new materials for next-generation astroparticle physics experiments

School Director: Ch.ma Prof. Renata Riva

Supervisor: Ch.mo Prof. Silvano Tosi

Co-supervisor: Ch.ma Dott.sa Gemma Testera

Candidate: Anna Marini

February 17, 2023

"There are more things in heaven and earth, Horatio, than are dreamt of in your philosophy". W. Shakespeare - *Hamlet*

"«Rotup!» strillò Sunny, e aveva ragione. Quando gli occhiali di Klaus erano rotolati sul pavimento, avevano colpito le cataste piuttosto forte, e ora sembravano una scultura moderna fatta da una mia amica anni fa. La scultura si intitolava *Ritorto, spaccato e irrimediabilmente rotto*." L. Snicket - *Una serie di sfortunati eventi - la sinistra segheria*

Introduction

Materials science is a multidisciplinary approach to various fields of physics and chemistry. The choice of the proper materials is crucial during design, R&D, and construction of an experiment where construction materials are the main source of background during data taking. Keeping materials-induced background under control is a key point for rare events physics searches. In this field, the background is due to particles whose interactions with the materials of the experimental apparatus can mimic a signal similar to the events that the experiment is looking for. Other unwanted particles can be detected and distinguished from the desired signal, but their detection affects the so-called dead time, in which the detector is blind for the tracing of the desired events.
To avoid these drawbacks, detection strategies of unwanted particles are adopted through the construction of specific detectors, or vetoes, which have the objective of shielding the active volume of the experiment (i.e. the part used for the detection of the rare event). This thesis work is focused on these devices: on one hand, I worked on the construction of a neutron veto for the DarkSide-20k experiment, on the other I tested some commercial organic scintillators in cryogenic environments. The latter project may pave the way for the integration of the aforementioned devices into rare-event physics experiments. Firstly I introduce the DarkSide-20k experiment, whose aim is the direct search for dark matter, based on the Weakly Interacting Massive Particle (WIMP) model. In this context, one of the main sources of background is represented by neutrons, whose interaction with the liquid argon, which is the active target material, could simulate a signal due to a WIMP. In order to overcome this issue, a neutron detector used as veto apparatus was designed, consisting of a 15 cm thick wall of polymethyl methacrylate (PMMA) loaded with gadolinium. The use of gadolinium is due to its high cross-section (which is a physical parameter that expresses the probability of a process) for neutron capture.
All the materials involved in the veto construction must meet severe radiopurity criteria: all the compounds are subjected to screening, in order to measure the presence of isotopes such as ^{40}K, ^{238}U, and ^{232}Th. Therefore, an R&D project was conducted for the development of an innovative and radiopure hybrid material consisting of PMMA containing a gadolinium-based compound. For our purposes,

it was chosen gadolinium oxide (Gd_2O_3) in the form of nanoparticles (indicated as NPs in this work). Since this compound is not miscible in methyl methacrylate (MMA, the starting monomer), it is necessary to functionalize the NPs in order to overcome the sedimentation and to obtain a quite homogeneous sample, still maintaining all the additives in a small concentration in order to avoid possible background sources. During the research activity, I worked on the gadolinium oxide R&D, which proposes a possible strategy to produce radiopure and homogeneous samples that meet the experiment requirements. This process is also scalable to industrial productions. Also, several characterizations were performed in order to test the thermomechanical properties of the composite material.

In chapter 1, I will introduce the state of the art in the dark matter (referred to in this work as DM) research field, where the DarkSide-20k experiment is inserted. In chapter 2, I will illustrate the DarkSide purpose and the detector (whose construction started in 2022). Mainly, I will focus on the veto apparatus and I will briefly discuss the background control requirements. In chapter 3 I will focus on the R&D project on the gadolinium-loaded PMMA, so the mixing and the polymerization procedures that have been developed. Also, I will show some results of the analyses conducted on the treated NPs, in order to evaluate the effectiveness of the functionalization and the stability of these grains in a colloidal solution. Chapter 4 is fully devoted to the characterizations of the polymeric samples, investigating the effect of the NPs doping on the thermomechanical properties of the polymeric matrix and testing the prototypes in a cryogenic environment (reproducing the conditions that will be encountered in the experiment). Chapter 5 is devoted to the description of the purification strategy which was adopted for a commercial surfactant involved in the synthesis process. In chapter 6, I will illustrate the work that has been done for the scaling of our production procedure to a partner industry. Also, in this chapter are reported some tests that have been done on the industrial samples. In chapter 7, finally, I will illustrate what has been done for the PESCE project, which is a grant funded by INFN for the past 3 years, whose purpose was the characterization of some organic scintillators in cryogenic environments. In the appendix, I briefly report additional projects that I followed during my Ph.D. years, related to astrophysics and space science, to which I contributed with my knowledge of materials science for the choice and characterization of the experimental apparata.

Contents

Acronyms

AAr Atmospheric Argon. XII, 14, 20, 21, 26

AIBN 2,2'-Azobis(2-methylpropionitrile). XIV, 44, 46, 49, 83

CCD Charge-Coupled devices. 115

CLTE coefficient of linear thermal expansion. XVI, XXII, 93–95

CMB Cosmic Microwave Background. XI, 1, 4

DLS Dynamic Light Scattering. XIV, 42, 43

DM dark matter. III, IV, XI, 1, 3–11, 13–15, 21, 22, 33, 64

DSC Differential Scanning Calorimetry. 52, 56, 58

ER Electron Recoil. XII, 17–20, 27

ESA European Space Agency. 115

ESR Enhanced Specular Reflector. 10

GAr gaseous argon. XI, 9

HP-Ge High Purity germanium. XX–XXII, 24, 71, 72, 74, 79, 80, 86, 97, 98

ICP-AES Inductively Coupled Plasma Atomic Emission Spectroscopy. 78, 79

ICP-MS Inductively Coupled Plasma Mass Spectrometer. XX, XXII, 24, 73, 79, 80, 96

ICSM Instrument Characterisation for Space Missions. 115

INFN Istituto Nazionale di Fisica Nucleare. IV, 100, 115

IR infrared. XIII, XIV, XVI, 39–42, 48, 88, 89

LAr liquid argon. XI, 9, 12–16, 19, 21, 25, 28, 29, 33

LN_2 Liquid Nitrogen. 64, 65, 91, 92

LNGS Laboratori Nazionali del Gran Sasso. XX–XXII, 11, 13, 21, 26, 74, 78, 79, 98

LSC Laboratorio Subterráneo de Canfranc. XXI, 79, 80

LZ LUX-ZEPLIN. 10–12, 32, 33

MMA methyl methacrylate. IV, XIV, XIX, XXII, 28, 35–39, 43, 44, 46–49, 52, 82, 83, 96, 97, 108

MOONLIght MOON seismicity detection with ultra-stable Laser Interferometry. 115

NPs nanoparticles. IV, V, XIV, XV, XIX, XX, 35, 37–45, 47–49, 51, 52, 56–60, 63–65, 68, 69, 75, 82, 84–86, 89, 91, 95, 96

NR Nuclear Recoil. XII, XIX, 13, 17–19, 21, 26, 27

OARPAF Osservatorio Astronomico Regionale Parco Antola Comune di Fascia. 115

PDU Photo Detection Unit. XIII, 21, 22, 28, 31

PEN polyethylene naphthalate. XIII, 29, 31

PESCE Plastic Economic Scintillators in Cryogenic Environment. IV, XVII, XXII, 99, 100, 103, 104, 113

PMMA polymethyl methacrylate. III, IV, XIII, XV, XVI, XIX–XXII, 8, 21, 28, 29, 31, 35, 38, 49, 51, 52, 55, 56, 68–70, 75, 80–82, 89–92, 94, 95, 97, 108, 113, 114

PMT photomultiplier tube. XVI, 11, 13, 101, 102

PSD Pulse Shape Discrimination. XII, 15, 17–20, 27

R&D Research and Development. III, IV, XIV, 35, 37, 47–50, 69, 75, 82, 108, 113

S1 Signal 1, the signal coming from the scintillation of a noble gas. XI, 8, 9, 11, 18

S2 Signal 2, the signal coming from the escaping electrons emitted during the ionization processes of a noble gas. XI, 8, 9, 11

SiPM silicon photomultiplier. 8–10, 21, 30

TGA Thermo-Gravimetric Analysis. XV, XX, 52, 58–61

TPB 1,1,4,4-tetraphenyl-1,3-butadiene. XIII, 29, 30

TPC Time Projection Chamber. V, XI, XII, 7–11, 13, 14, 21, 22, 25, 27, 29, 30, 69, 79–81

UAr Underground Argon. XII, XIII, 14, 19–21, 25, 28, 33

VUV vacuum ultraviolet. 10, 16

WIMP Weakly Interacting Massive Particle. III, V, XII, 5–7, 10–14, 19, 20, 22, 25, 33

List of Figures

List of Tables

Chapter 1

Dark Matter

In this chapter I will briefly illustrate the state of the art in DM research, to contextualize the work of this thesis. In the first section, I will analyze some examples of evidence of the existence of DM, citing some of the best-known cases. I will then briefly outline the best candidates and, consequently, the DM models. Finally, I will introduce the methods of research of the DM, focusing in particular on the detection with noble gas targets, since the latter is the experimental context in which this work is inserted.

1.1 Evidences

At present, the scientific community agrees that ordinary (or baryonic) matter represents only about 5% of what makes up the universe. The remaining part is made up of dark energy (about 68%) and DM (about 27%) [1]. This statement is supported by various pieces of evidence, from the galactic to the cosmological scale. Here I quote some of the most shining examples:

- Galactical evidences:
  - Rotation curve of spiral galaxies
  - Galaxies clusters
- Intergalactical evidences:
  - Gravitational lensing
- Cosmological evidences:
  - Cosmic Microwave Background, or CMB
  - Big Bang Nucleosynthesis

The deepening of each of these pieces of evidence is beyond the scope of this work, therefore I will limit myself to briefly treating only a few examples.

1.1.1 Rotation curve of spiral galaxies

Spirals galaxies are characterized by circular symmetry, a bright nucleus surrounded by a thin outer disk, and a superimposed spiral structure [2]. The rotation curve of these galaxies is the representation of the speed of rotation as a function of the distance from the center of the galaxy, according to the Newtonian gravity formula given in equation 1.1.

$$v(r) = \sqrt{\frac{GM(r)}{r}} \tag{1.1}$$

Where $M(r) = 4\pi \int \rho(r) r^2 dr$ is the mass as a function of the distance from the center, and ρ is the density. Thus, the rotation speed is expected to decrease in areas far from the center as $1/\sqrt{r}$. In the early 1970s, the astronomer Vera Rubin, however, found that the experimental data largely contradicted what was predicted. In particular, thanks to spectroscopic redshift measurements of the spectral lines of hydrogen [3], a huge difference was noticed: in fact, the rotation speed is higher than what was predicted. This could be explained both by the failure of Newtonian gravity or by the presence of a large mass of non-luminous matter whose density is predicted to be $\rho \propto 1/r^2$. For any further information, see [4].

1.1.2 Gravitational lensing

The deflection of light due to gravitational effects was predicted by General Relativity theory in 1915 and then confirmed in 1919, thanks to a solar eclipse, which represented an excellent opportunity to measure the light-bending effect around the Sun. As predicted by Einstein, massive celestial objects located within the line of sight between us and a background light source, cause a sufficient curvature of spacetime for the path of light emitted by the objects in the background to deviate, as happens with lenses. This phenomenon is known as gravitational lensing. The object causing such effect is indicated as a gravitational lens [5]. This effect has been widely used in astrophysics to trace the mass of celestial objects, studying their gravitational lensing effect, since the strength of the deflection is proportional to the square root of object mass. The gravitational lens effect is partly due to luminous matter and partly to non-luminous matter, therefore the study of celestial objects through this phenomenon has allowed us to observe discrepancies between the mass due to the luminous matter alone (detected with luminosity measurements) and that obtained through observation of gravitational lensing [6]. This observation constitutes another proof of the presence of a large mass of non-luminous matter in the universe. The ratio between mass inferred by gravitational lensing and from luminosity measurements assumes values between 10 and 20 for galaxies,

while they are between 100 and 300 for clusters, suggesting thus the presence of non-luminous matter. An excellent example of these observations is the Bullet Cluster, which is the product of the collision of two galaxy clusters. If we assume that each cluster is composed mainly of stars, intergalactic hot gas, and DM, it is possible to study each component separately with different techniques. The gravitational lensing measurements showed that the overall mass largely exceeded that predicted based on the baryon matter signal alone. A shining example of this phenomenon is the Bullet cluster case, shown in figure 1.1. This

Figure 1.1 – The bullet cluster. Image credits: X-ray: NASA/CXC/CfA/M.Markevitch et al.; Optical: NASA/STScI; Magellan/U.Arizona/D.Clowe et al.; Lensing Map: NASA/STScI; ESO WFI; Magellan/U.Arizona/D.Clowe et al.

figure shows several measurements acquired with different instruments: the optical measurement, which highlights the objects such as galaxies or galaxy clusters, the pink masses, which represent the measure of interstellar hot gas, and the blue masses. This latter mass is the result of the measurement of gravitational lensing, acquired with Chandra. The key point is that gravitational lensing can testify to the presence of non-luminous matter. The fact that there is no overlap of the pink mass (which is due just to luminous matter) and the blue mass (due to all matter), represents a possible proof of the existence of a large amount of DM.

1.1.3 Cosmic Microwave Background

One of the most accredited cosmological models takes into account DM as one of the major constituents of our universe: this is the ΛCDM (Lambda Cold Dark Matter), whose name refers both to the cosmological constant (Λ) and the cold DM (that is DM characterized by low kinetic energy), thus recognizing the presence of a large missing mass. In this scenario, the total universe energy

density ρ has three main contributions: the density of energy in form of radiation ρ_r, the dark energy density ρ_Λ and energy density in form of matter (exploiting the E=mc^2 relationship) ρ_m; the latter can be further divided into a baryonic component ρ_b and a cold DM component ρ_{CDM} [7]. These values are commonly expressed as density fractions $\Omega_i = \rho_i/\rho_c$, where ρ_c is the critical density required so that the universe is flat and isotropic. This comes from the general relativity theory, in which the geometry of space-time is defined [8]. In this context, it is possible to investigate the DM contribution thanks to measurements on the CMB, as it was done by the Planck mission. Planck was a space observatory, operating between 2009 and 2013, that performed a mapping of the anisotropies in the CMB, which led to a more precise definition of the average of DM populating the universe [9]. The CMB mapping by Planck is reported in figure 1.2 [10].

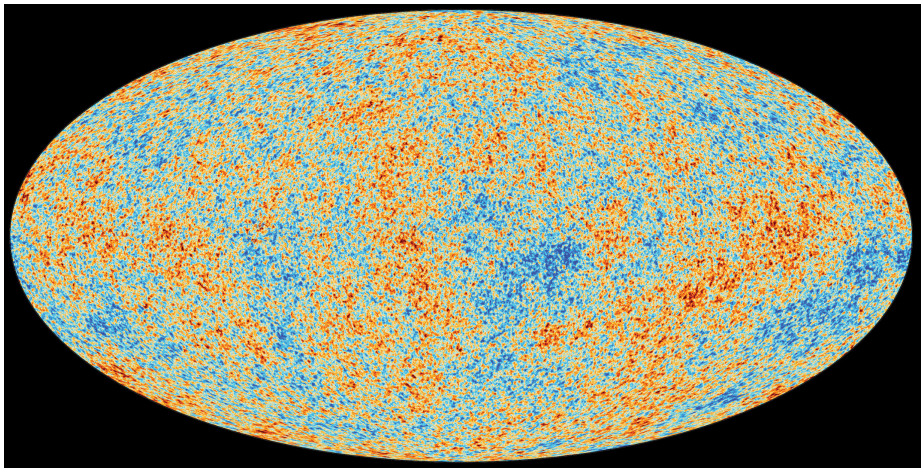

Figure 1.2 – Cosmic Background Microwave mapping with Planck observatory, showing the anisotropies of the CMB.

1.2 Candidates

Following the evidence that testifies to the existence of a large portion of still unknown non-luminous matter, numerous hypotheses have been produced about the nature of this matter, with the consequent birth of many theories. An overview of the DM candidates is reported in figure 1.3 [11].
There are three possible explanations for this evidence:

- a failure of the general relativity (the modified gravity ensemble in figure 1.3)
- the missing mass is due to non-luminous macroscopic objects (the macroscopic ensemble in figure 1.3)

- the missing mass is due to the DM, which consists of particles

Based on the observations (see section 1.1), it is possible to draw a generic profile for DM candidates, which therefore must be:

- Stable on cosmological times;
- Electrically neutral (they don't feel electromagnetic interactions)
- With no color change (they don't feel strong interactions)

This latter hypothesis is not included in the Standard Model [12] of particle physics, therefore many extensions of it have been hypothesized. This work was

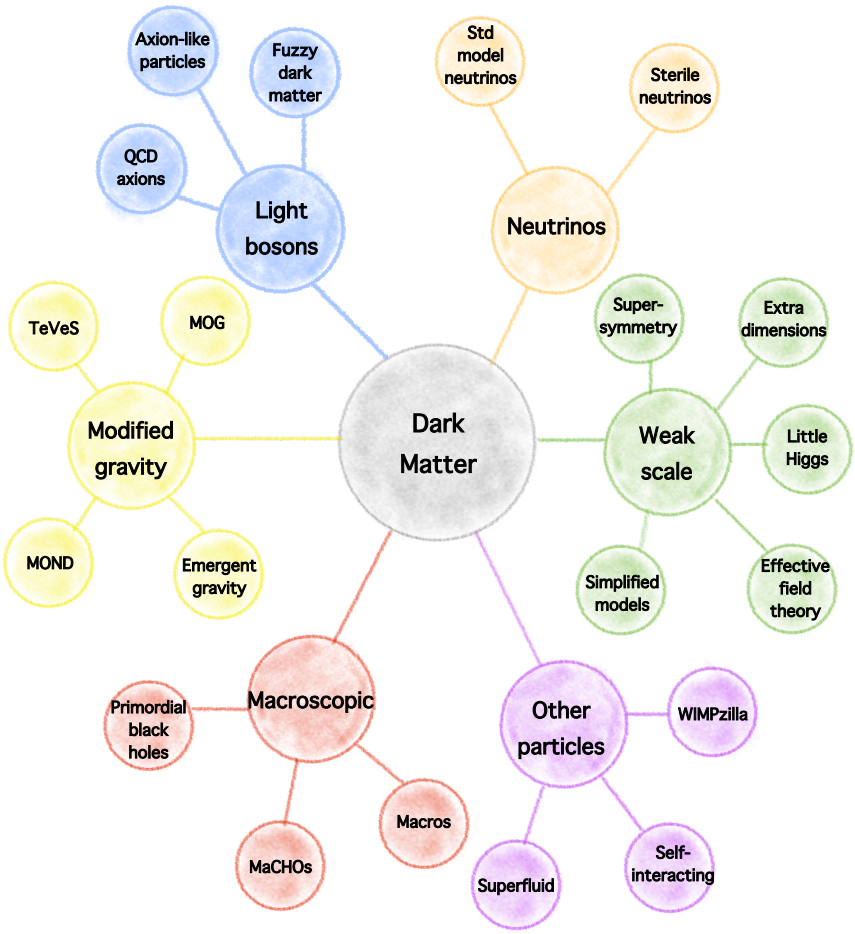

Figure 1.3 – An overview of the DM candidates.

done as part of the DarkSide-20k experiment (described in chapter 2), which is a direct DM research experiment that assumes that the preferred DM candidate is the WIMP.

1.2.1 WIMPs

The Weakly Interacting Massive Particle is the leading class of DM candidates. A WIMP is a stable and neutral particle, whose mass lies in a range between a few GeV/c^2 to around tens of TeV/c^2 (in particle physics it is customary to indicate the mass of particles in eV, as follows from the equation $E = mc^2$, thus $m = E/c^2$). Just to give an order of magnitude, an electron has a mass of 0.511 MeV/c^2, therefore WIMPs have a much larger mass than most of the common elementary particles. For this reason, the existence of WIMPs can only be partially investigated with the use of particle accelerators, contrary to the other candidates.

1.3 Dark Matter search

Following what has been illustrated in the previous sections, it follows that DM detection is constructed strictly on the basis of the candidate in question. A very simplistic scheme of the detection mechanisms (assuming the particle nature of the DM) is shown in figure 1.4. Following this scheme, there are three

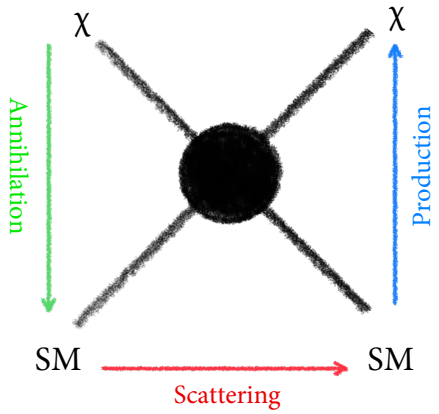

Figure 1.4 – Interactions mechanism of DM. The SM acronym stands for standard matter, while the letter χ represents a generic DM particle.

basic mechanisms of DM interaction. In the case of the production, the DM is supposed to be produced as a result of the interaction of ordinary matter, following a mechanism similar to equation 1.2, where p represents an ordinary matter particle, while χ is the typical symbol for a DM particle.

$$p + p \rightarrow \chi + \chi \tag{1.2}$$

In the case of annihilation, according to the so-called indirect DM search, reaction products are sought to result from an annihilation process of two DM particles, following the equation 1.3:

$$\chi + \chi \rightarrow p + p \tag{1.3}$$

This detection mechanism exploits anomalies, possibly due to DM annihilation, in the fluxes of Standard Model's particles. In the last case, which represents the context in which the direct search for DM is inserted, we are looking for interactions of DM particles with ordinary matter, i.e. energy transfer. This mechanism is represented by equation 1.4, where the letter N represents a generic ordinary matter nucleus [13].

$$\chi + N \rightarrow N + \chi \tag{1.4}$$

The direct search for DM is based on a careful selection of the optimal target. The identification of DM (or, in any case, rare events) consists in looking at the effects on temperature (due to nuclear recoils that generate the formation of phonons), ionization charge (following the deposition of energy in the target, which therefore leads to ionization) or scintillation light (de-excitation of excited atoms in the form of photon emission). Not all materials are suitable for this purpose, because only some reach the radiopurity (i.e. the absence of unstable isotopes whose radioactive decay could induce unwanted nuclear reactions) requirements required for this purpose. In fact, in the search for rare events, the background induced by the impurities present in the construction materials must be kept under very strict control.
Up to now, the Borexino experiment represents excellence in terms of ray radiopurity levels [14]. Typical scintillating materials that can reach these radio-purity standards are inorganic crystals (NaI (Tl)), as in the SABRE experiment [15] or TeO_2 as in the CUORE experiment [16]) or liquefied noble gases.

1.4 Dark Matter search with Time Projection Chambers

One of the most promising techniques, as previously mentioned, is noble gas detection. In fact, it is assumed that the WIMPs can interact with the target nuclei of the detector and that this can lead to the emission of scintillation light and ionization charge which could therefore testify to the effective interaction of a DM particle. Noble gas detectors are considered extremely promising since about thirty years ago, due to their high scintillation rate (around 10^4 photons per each MeV of deposited energy) [17], the possibility of large-scale production of

scintillators and, in the case of argon, the cost-effectiveness. Furthermore, thanks to noble gases it is possible to satisfy an important requirement of the detection of rare events, namely the need to have a low background to avoid competitive processes at the event itself: in fact, noble gases can be easily purified (as an example we can report the purification of DarkSide-20k argon from 39Ar, as reported in section 2.2.3). Finally, one of the great advantages of these detectors is the possibility of having a double signal following a possible interaction with DM, thanks to the realization of Time Projection Chamber (or TPC). A TPC is a detector consisting of a liquified noble gas, which also includes an anode and a cathode, used for the creation of a drift electric field that deals with the transport and extraction of the electrons that are emitted as a result of the interaction mechanisms of the noble gas nuclei with the target particles. The uniformity of the field is maintained through a proper metallic cage. Once drifted, the electrons slam into a grid that allows for the 3D reconstruction of the interaction [18]. In the context of rare event physics through noble gas TPC, two types of signals are produced: a first one, called S1, is produced following a scintillation mechanism of the noble liquid (and therefore it is detected via dedicated photosensors), while the second one, called S2, comes from the production of free electrons following the ionization of the noble liquid atoms. DarkSide-20k, which is the experiment this work is inserted in, uses a double-phase TPC, which is filled with a noble scintillator (argon) in both liquid and gaseous phase. An operating diagram of the DarkSide-20k TPC is shown in figure 1.5. As it can be seen from the figure, in the case of DarkSide-20k, the double phase TPC consists of a volume of liquid argon above which there is a layer of the same target but in the gas phase (this part is called the gas pocket). The TPC is in the shape of an octagonal-based prism, at the bases of which there are two planes, which constitute the anode and the cathode, made of PMMA.

Since it is essential, for the implementation of the electric field, that the anode and the cathode are conductive, their surfaces are covered with a layer of commercial paint, named Clevios™F ET [19], which is made up of a conductive polymer, which is the PEDOT:PSS (see the structure formula reported in figure 1.6). An electric field is generated between the cathode and the anode, and its uniformity throughout the volume is guaranteed by a field cage, which is constituted by grooves carved into the plastic wall covered by conductive paint. The drifting field transports the electrons up to the grid, where they are extracted through a suitable extraction field, thus ending up in the gaseous phase. Here, finally, they are accelerated by a third electric field and can undergo two processes: in the first case, they ionize the present argon atoms or they excite them, with consequent emission of light (with the phenomenon of electroluminescence) [20]. This electroluminescence signal constitutes S2.

The DarkSide-20k detector is equipped with suitable photosensors (silicon photo-

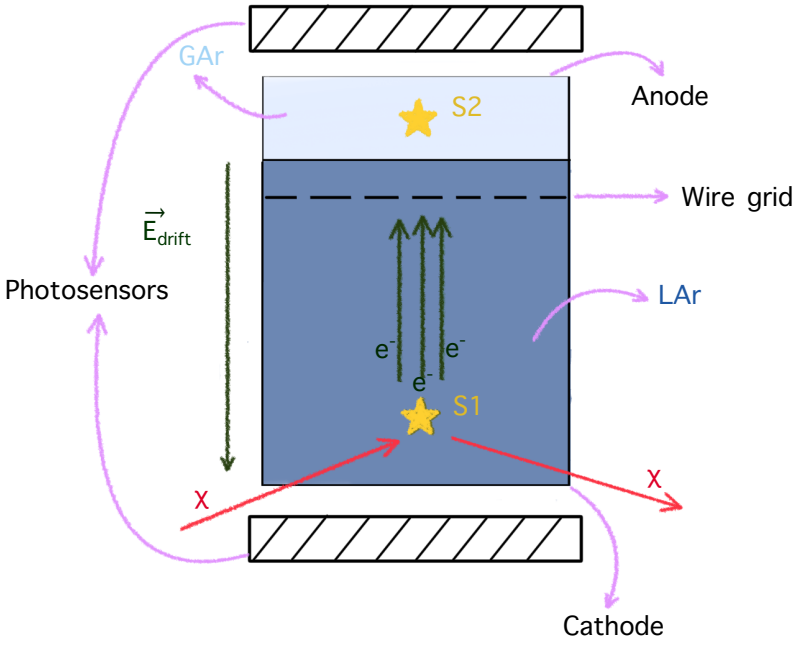

Figure 1.5 – Operating diagram of the DarkSide-20k TPC. The chamber is filled with argon, in both liquid (LAr) and gaseous (GAr) phases. The letter χ represents a DM particle, which interacts with the argon nuclei in the liquid phase, generating S1 and escaping electrons, which are drifted and extracted in the gaseous phase, where they generate S2.

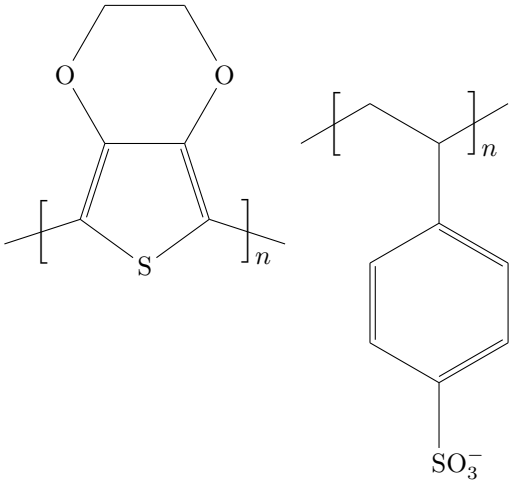

Figure 1.6 – Structure formula of PEDOT:PSS.

multipliers, or SiPMs, see section 2.3) to read the luminous signals. To maximize the light yield, some reflective foils are secured to the exterior of the TPC barrel.

These foils are made of Enhanced Specular Reflector (ESR) [21]. The photons emitted by argon during the scintillation (whose mechanism is described in section 2.1) have a wavelength of 128 nm, and therefore this signal is not readable by the SiPMs, since VUV light is absorbed by the protective layers of these devices [22]. Therefore, this light is wavelength shifted to 420 nm (as illustrated in section 2.3).

1.5 State of the art in dark matter searches in TPCs

To date, noble gas detectors use xenon or, as in the case of DarkSide, argon. Currently, the main experiments with similarities to DarkSide-20k are LZ, Xenon 1T, and Xenon NT. In this section, I will briefly illustrate their main characteristics, and I will illustrate the results, in terms of WIMP detection limits, referring to the most recent results that are illustrated in the figure 1.7 [23]. This plot contains

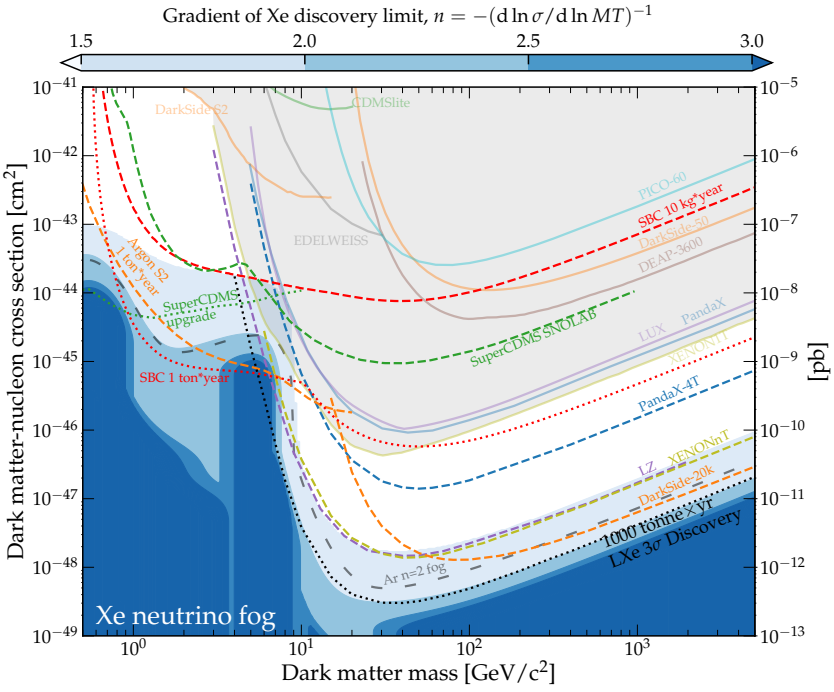

Figure 1.7 – DM discovery plot for the most recent generation of direct search detectors. The interaction cross-section is reported as a function of the hypothetical DM mass. Each curve is associated with an experiment, and represents its limit of detection at a 90% confidence level.

the results of the main experiments in the field of direct detection of DM. The interaction cross-section of the WIMP is shown as a function of its hypothetical

mass. Therefore, each experiment is associated with a curve, which delineates its limit of detection of DM, at 5σ (so with an uncertainty of about $3{\cdot}10^{-7}$) or, as in this case, at 90% confidence level.

1.5.1 LUX-ZEPLIN

The LUX-ZEPLIN (LZ) experiment [24] is a DM detector consisting of a dual phase xenon-based TPC. It is installed and operating at the Sanford Underground Research Facility, in South Dakota. The TPC has a cylindrical shape with a radius of 1.5 m, and it is placed in a double-wall titanium cryostat that is filled with 10 tonnes of liquid xenon (at a temperature around 165 K). The light signals are read by 494 photomultiplier tubes (PMTs), divided into two groups and positioned one on the top, and the other on the bottom. As with the DarkSide experiment, two signals are produced, namely S1 and S2 (as explained in section 1.4). In the DM detection experiments, based on the exposure time and the particle cross-section, the detector is capable to explore different regions and different possible masses of the particle. LZ is capable to set a 90% confidence level limit for the spin-independent WIMP cross-section as a function of WIMP mass equal to what is illustrated in figure 1.7. For what concerns LZ, the curve has a minimum at $m_\chi = 30$ GeV/c^2 with a limit of $\sigma_{SI} = 5.9{\cdot}10^{-48}$cm^2 [24]. This scenario can be enriched by considering the results achieved by the Xenon collaboration, with the Xenon 1T and Xenon NT experiments.

1.5.2 XENON1T and XENONnT

The Xenon collaboration has produced results, setting increasingly stringent limits in terms of WIMP interaction cross-section, through generations of experiments: the most recent, currently in the data capture phase, is XENONnT, while the previous one is XENON1T. XENON1T was located in at LNGS. The detector was a cylindrical dual-phase xenon-based TPC, that has been active and in the data collection phase between 2016 and 2018. The active target consisted of 2 tonnes of ultrapure liquid xenon. The signals (also in this case, luminous signals S1 and S2) were read by two arrays of 127 PMTs [25]. As it can be seen from figure 1.7, XENON1T placed a limit in the WIMP-nucleon spin-independent elastic scatter cross-section underlined by the blue curve. There is a minimum for the cross-section value of σ_{SI}=4.1$\cdot10^{-47}$cm^2, for masses values around 30 GeV/c^2 and 90% confidence level [26].
XENONnT, on the other hand, is part of the most recent generation of detectors, and it consists of a double-phase TPC, again based on xenon, again of cylindrical geometry, whose active volume is made up of 5.9 tonnes of xenon. Once again, the S1 and S2 signals are detected with two arrays of PMTs [27]. This detector's generation has not only allowed obtaining a new expected limit on the spin-

independent cross-section of the WIMPs, but has also allowed greater control of the background induced by tritium and radon. Regarding the sensitivity of this generation, it is expected that XENONnT reaches (as illustrated in figure 1.7), a cross-section for spin-independent interaction of σ_{SI}=1.4·10^{-48}cm^2 for a mass of 50 GeV/c^2 at 90% confidence level.
The results of LZ and XENON largely represent the scenario DarkSide-20k fits into. The main difference with these experiments is the use of LAr (and not xenon) as a target. This choice is due to an important characteristic of argon, as it will be illustrated in section 2.2.

Chapter 2

The DarkSide-20k experiment

In this chapter I will describe the DarkSide-20k experiment, starting with the liquid argon (indicated as LAr) detector (focusing on the mechanism for detecting rare events with LAr) and in particular focusing on the neutron veto; the context in which this thesis is carried on.

2.1 The DarkSide project

The DarkSide-20k detector will be installed at Laboratori Nazionali del Gran Sasso, and it deals with the direct search of DM particles based on the hypothesis of the WIMP. This experiment uses a detection technology based on a double-phase LAr TPC. Interactions of WIMP are expected in the form of Nuclear Recoil (or NR), having energies around 10^2 keV. The DarkSide project has developed through a few steps, which led to the creation of DarkSide-20k predecessors. From 2011 until 2013, the collaboration worked on DarkSide-10, a prototype consisting of an active volume of 10 kg of LAr in a dual phase TPC. This prototype was installed at LNGS and made it possible to measure (via some photo-multiplier tubes, PMTs) the scintillation light yield of double-phase argon-based TPC by studying the scintillation spectra obtained from the γ-emitting radioactive sources positioned outside the cryostat [28]. Later, DarkSide-10 was replaced by DarkSide-50, which was located in Hall C at LNGS until the decommissioning (started in 2022), consisting of an active volume of 50 kg of ultrapure LAr, which is extracted from an underground site (as illustrated in section 2.2.3). In addition to the TPC, which is the heart of the experiment, DarkSide-50 also had a neutron veto consisting of a borate liquid scintillator, located in an aqueous muon veto that exploits the Cherenkov effect [29]. Thanks to this design, DarkSide-50 was able to prove the ability to reach the low levels of background necessary for the detection of DM, acting in all respects as a

demonstrator for subsequent upgrades [30] and, not secondarily, by placing limits on the revelation of the WIMPs which represented the best result of its time. Moreover, DarkSide-50 showed the huge abatement in the background by comparing the performance between filling the TPC with Atmospheric Argon (or AAr) and with Underground Argon (or UAr) [31]; this aspect will be explored in section 2.2.3.
Finally, the last experiment of the DarkSide collaboration is DarkSide-20k, which will be installed again in Hall C of the Gran Sasso underground laboratories. Starting from the evidence shown by DarkSide-50, DarkSide-20k includes an active neutron veto to maintain a low level of background suitable for the detection of DM events. The realization of a hybrid material for the realization of the neutron veto constitutes the context in which this work is inserted.

2.2 Dark matter search with liquid argon

Argon is the third most abundant gas in the Earth's atmosphere and has a boiling temperature of 87.3 K at a pressure equal to 1 atm. Up to date, the best limit with a LAr detector was achieved by the experiment DEAP-3600 [32].
A simple overview of the scintillation mechanisms of argon is reported in figure 2.1 [20], and described in detail in section 2.2.1. Argon represents an ideal

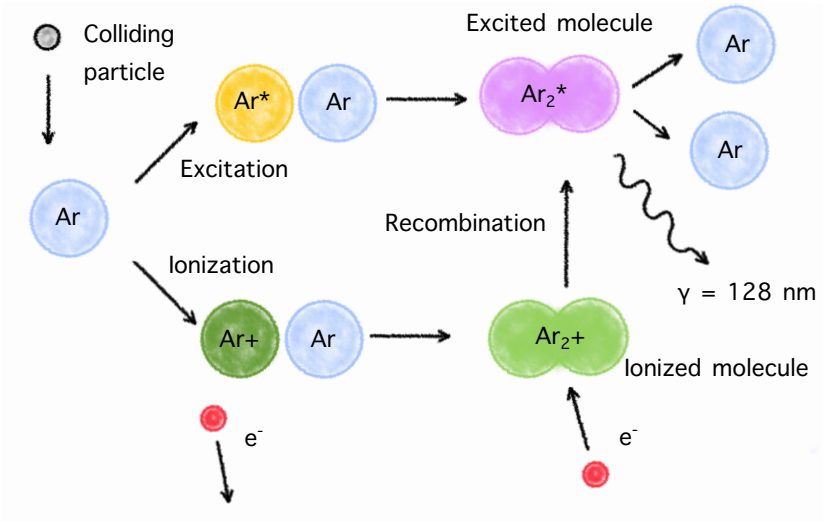

Figure 2.1 – A schematic overview of argon scintillation mechanisms induced by excitation and ionization. In the case of excitation, the formation of the dimers occurs, with subsequent de-excitation and emission of photons at 128 nm. In the case of ionization, the formation of an ionized molecule occurs, from which the dimer is formed (again, with subsequent emission of photons at 128 nm).

candidate for the construction of DM detectors, as it can be used for the realization of large masses of targets (and this is crucial, due to the cross-section of DM particles), it features excellent Pulse Shape Discrimination, or PSD (this aspect will be explored in section 2.2.2) and is cheap. LAr produces about 40,000 photons for each MeV of energy deposited and is transparent to its own scintillation light, since it is produced in a molecular continuum [33].
The hypothesis on which the DarkSide-20k technology is developed is that when a DM particle (χ) interacts with an Ar nucleus, several processes can arise. These processes are summarised in figure 2.2. As can be seen, the interaction involves

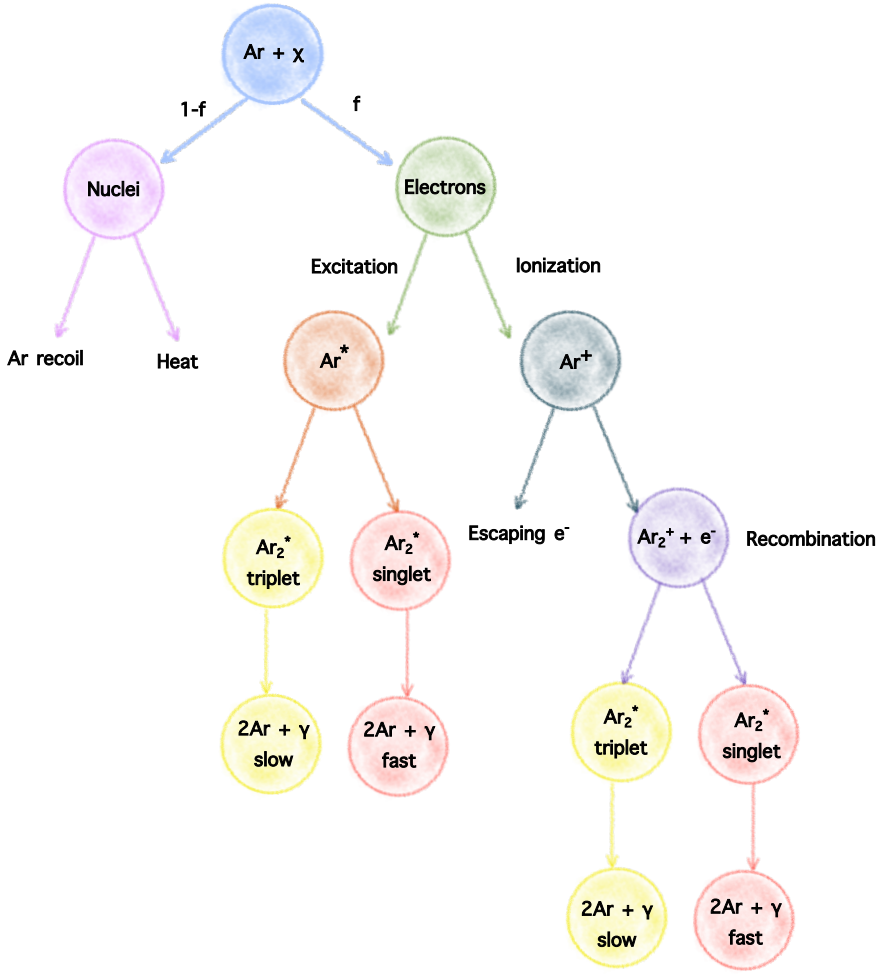

Figure 2.2 – Argon nucleus interacting with a DM particle.

the recoil of the argon nucleus. The recoiling nucleus partly loses its energy through electronic collisions, and partly transfers it to other nuclei. As far as electronic processes are concerned, they can give rise to excitation and ionization.

The excited atoms can form the so-called excimers (that are complexes formed by two atoms of the same type, one of these is in the ground state and the other in the excited state, typically linked by π interactions [34]), from whose de-excitation the scintillation light is produced (all the details can be found in section 2.2.1). For what concerns the ionization, as it can be seen in figure 2.2, the creation of positive Ar^+ ions and free electrons can occur. These ions can therefore form molecular $Ar_2{}^+$ ions with a time scale around some picoseconds. A fraction of the electrons (the so-called escaping electrons) can be drifted away by the electric field (as illustrated in section 1.4), while the remaining part recombines with the $Ar_2{}^+$, leading again to the production of scintillation light.

2.2.1 Scintillation

The scintillation light is produced both from excitation and recombination mechanisms illustrated before. In particular, the excitation light that can be observed in a LAr target (and thus in the DarkSide-20k experiment) is due to different phenomena, as follows:

- Excitation luminescence
- Recombination luminescence

Excitation luminescence can occur when a particle (let's take an electron for example) interacts with an argon atom generating an excited atom Ar^*, in which an electron in the valence band passes to the next orbital: this configuration energetically favors a state of dimerization, therefore an $Ar_2^{*,\nu}$ molecule is formed, which is a molecule that is in an excited vibrational state. This molecule goes into an excited electronic state Ar_2^* with a non-radiative mechanism, as shown in equation 2.1.

$$Ar_2^{*,\nu} + Ar \rightarrow Ar_2^* + Ar \tag{2.1}$$

Finally, de-energizes itself by emitting VUV light. This last step is reported in equation 2.2.

$$Ar_2^* \rightarrow Ar + Ar + h\nu \tag{2.2}$$

In the case of recombination luminescence, however, as described above, there is the formation of Ar^{**}. One of the cations recombines with a free electron, (previously produced by ionization effects), resulting in the formation of neutral argon in an excited configuration Ar^{**}, which is de-excited by emitting energy in the form of heat (Δ), as reported in the passages of equation 2.3.

$$\begin{aligned} Ar^{**} + Ar &\rightarrow Ar^* + Ar + \Delta \\ Ar^* + Ar + Ar &\rightarrow Ar_2^* + Ar + \Delta \end{aligned} \tag{2.3}$$

At this point, VUV light is emitted again according to the mechanism reported in equation 2.2. Light emission can occur in two different ways (and thus at different times), depending on whether the excited molecule is in a singlet (whose configuration is shown in equation 2.4) or triplet (equation 2.5) state.

$$\left\{ \frac{1}{\sqrt{2}}|\uparrow\downarrow\rangle - |\downarrow\uparrow\rangle \quad \text{singlet} \right. \tag{2.4}$$

$$\left\{ \begin{array}{l} |\uparrow\uparrow\rangle \\ \frac{1}{\sqrt{2}}|\uparrow\downarrow\rangle + |\downarrow\uparrow\rangle \quad \text{triplet} \\ |\downarrow\downarrow\rangle \end{array} \right. \tag{2.5}$$

The singlet state has a decay time $\tau_s \sim 6\ ns$ (called fast in the figure 2.2), while the triplet state is associated with a time constant $\tau_t \sim 1.5\ \mu s$ (called slow in the figure 2.2) [35]. There are some competitive non-radiative mechanisms that can lead to a reduction of the light emitted, called bi-excitonic quenching, photoionization, and the Penning process. They are illustrated in equation 2.6 [36].

$$\begin{aligned} Ar^* + Ar^* &\rightarrow Ar + Ar^+ + e^- \\ Ar^* + Ar_2^* &\rightarrow Ar + Ar_2^+ + e^- \\ Ar_2^* + Ar_2^* &\rightarrow 2Ar + Ar_2^+ + e^- \end{aligned} \tag{2.6}$$

2.2.2 Pulse Shape Discrimination

As was seen in the previous sections, the emission of light in argon can occur starting from two different states, the singlet and triplet states, characterized by two very different time constants. This characteristic is the basis of one of the advantages of argon as a detector for rare events, namely it's Pulse Shape Discrimination, (or PSD), which consists in the ability to distinguish signals associated with Nuclear Recoils (or NRs) events from the ones from Electron Recoils, (or ERs). These two types of events, in fact, are characterized by different fractions of singlet and triplet states, thus resulting in profoundly different light spectra as a function of time, as can be seen in figure 2.3 [37]. The NR events have a greater fraction of singlet, resulting thus in a more rapid signal as a function of the time. The ER events, on the contrary, have a greater fraction of triplets, leading to a slower signal as a function of the time. In order to better distinguish between NR and ER events, it is possible to develop a parameter to look at light distribution in time ($S1(t)$) and normalized by the total emitted light. In DarkSide-50 we use the so-called $f90$, which is obtained from the equation 2.7:

$$f90 = \frac{\int_0^{90\ ns} S1(t)dt}{\int_0^{t_{end}} S1(t)dt} \tag{2.7}$$

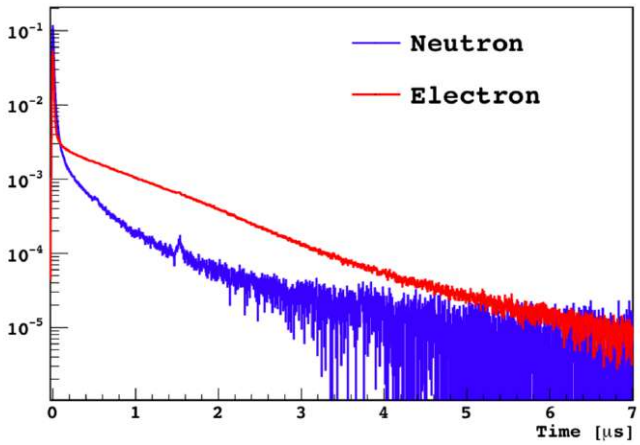

Figure 2.3 – PSD capability of argon. The ER events are caused by electrons, and they are depicted by the red curve. The blue curve represents the NR events, which are caused by interactions with neutrons. The huge difference between the two curves is strictly related to the different fractions of singlet and triplet states, which have different time constants.

This parameter has been optimized (especially as regards the numerator, which is the integration window) with neutron sources of AmBe. In figure 2.4, it is

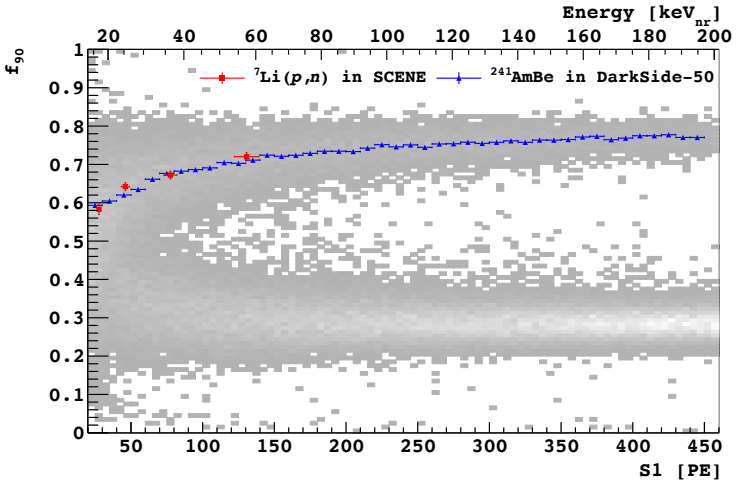

Figure 2.4 – Results of the calibration campaign performed for DarkSide-50. The calibration was conducted with a AmBe neutron source. The population with $f90 \approx 0.7$ corresponds to NR events, while the population carrying $f90 \approx 0.3$ corresponds to the ER events.

possible to observe the values of the parameter $f90$ as a function of S1. The NR events are located in the region around $f90 = 0.7$, while the ER events around $f90 = 0.3$: the nuclear recoils have a larger $f90$ because of the major light fraction in the first 90 ns, while in the case of ER the light is more distributed

in time. The essence of advantage of using argon instead of xenon is the big difference in time constants, which allows us to clearly distinguish ERs and NRs [38]. In this context, it is assumed that WIMPs interact with LAr by inducing NR. The PSD therefore allows eliminating the ERs, since they are a source of background. The results of the PSD for 532 days of taking data in DarkSide-50 are illustrated in figure 2.5 [37]. In the image, the blue area represents the

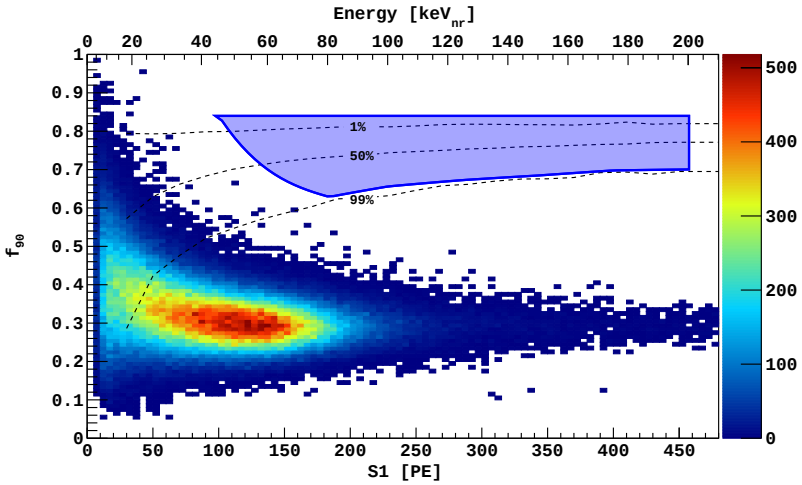

Figure 2.5 – Results from DarkSide-50 in 532.4 days of data taking with UAr. The plot shows the distribution of events in f90 (after some cuts to maximize efficiency). The dashed lines identify the lower limits of the NR signal regions and their acceptances. The region with the blue background highlights the WIMP search region. The energy scale for NRs relevant to WIMP scattering is shown above, while below the energy scale in terms of the number of photo-electrons is reported. The different colors refer to the number of events per energy.

WIMPs search region: as it can be noticed, no background events are found in that area. This is due to the excellent argon's PSD, but most importantly to the DarkSide-20k neutron veto.

As was previously mentioned, the expected WIMP signals are NR in the UAr, this means that the most dangerous background for DarkSide is all those events that could induce NRs, which could then be mistaken for WIMP events. The particles that most of all induce unwanted NRs are neutrons, which therefore must be detected and captured as much as possible. In this regard, an active neutron veto has been developed within the DarkSide collaboration, the operation of which is described in detail in section 2.3.2.

The presence of this detector allows DarkSide to eliminate all possible neutron-induced NR events from the WIMP search region.

2.2.3 Underground argon

The most abundant argon isotopes in nature are ^{40}Ar, ^{38}Ar and ^{36}Ar, in the proportion shown in the graph in Figure 2.6 [39], [40]. Some isotopes, such as ^{42}Ar, ^{37}Ar and ^{39}Ar are not inherently natural in AAr; the latter in particular is generated in AAr thanks to the activation due to cosmic rays, as reported in equation 2.8.

$$^{40}Ar + n \rightarrow \ ^{39}Ar + 2n \tag{2.8}$$

^{39}Ar is particularly harmful to the physics experiments of rare events, as it is an unstable isotope, which then decays with consequent emission of $\bar{\nu}$ (antineutrinos) and β particles (electrons), as shown in equation 2.9 [41]. The β particles generate a background signal that can affect the detection efficiency for rare events, since, being electrons, they induce ERs, as it was discussed in section 2.2.2.

$$^{39}Ar \rightarrow \ ^{39}K + \beta^{-} + \bar{\nu} \tag{2.9}$$

Therefore, as will be shown below, in these contexts it is mandatory to keep a concentration of ^{39}Ar as low as possible. This is important because even if we are able to reject ERs with the PSD, the presence of β emitters limits the sensitivity increasing the so-called dead time. For this purpose, the DarkSide

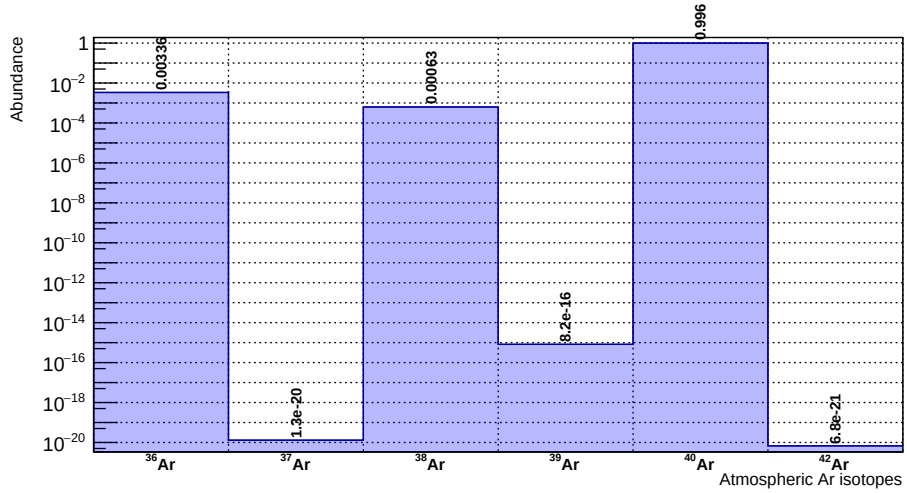

Figure 2.6 – An overview of the natural AAr isotopes abundance. It is interesting to note that the presence of ^{39}Ar seems very scarce ($8.2{\cdot}10^{-16}$), but it is actually sufficiently high to make the AAr not usable in the detection of WIMPs.

collaboration has developed two facilities suitable for the extraction of argon from deep underground sources (UAr) and for consequent distillation. UAr is expected to be poor in ^{39}Ar content, due to the rocks shielding of cosmic rays. DarkSide-50, in fact, measured a content of ^{39}Ar in UAr equal to 1/1400

compared to AAr [42]. DarkSide-50, in fact, was operated both with AAr and UAr [43]. First of all, UAr is extracted and purified in Colorado, thanks to the Urania plant, which is capable to provide 330 kg/day of UAr with a 99.99% purity, extracting it from underground CO_2 wells [44]. Then, the argon will undergo a final purification step in Sardinia, a unique plant that consists of a 350 m high distillation column in the Carbosulcis coal mine, where a final purification is performed [45].

2.3 The DarkSide-20k detector

DarkSide-20k is a direct DM research experiment based on a dual-phase TPC filled with approximately 20 tonnes of ultra-pure UAr. One of the main features of DarkSide is the low detector-induced background, in fact the goal is to have 0.1 NR events (most of which are generated by (α, n) processes in the detector itself) in the full exposure of the detector. This goal can be achieved thanks to the exceptional screening of each material used for the construction of the detector, the extraction (with subsequent purification) of ultra-pure UAr, and thanks to the neutron veto, whose function is to moderate, capture and detect neutron signals that would otherwise be completely indistinguishable from DM signals. The detector will be located in Hall C in the underground laboratories of LNGS, in Assergi (Italy). A sketch of the detector is represented in figure 2.7. The inner part of the detector is the TPC (described in section 1.4), whose walls coincide with the neutron veto. This inner part is enclosed in a stainless steel vessel and filled with UAr. Outside the vessel, there is a volume of atmospheric LAr (700 tonnes). The whole apparatus is kept at temperature through a membrane cryostat, inside which there is an insulating layer. The internal dimensions of the cryostat (taking as reference the distance between the insulating walls) are around 8.5 m. A detail of the innermost part of the detector (neutron veto and TPC) is shown in figure 2.8a and 2.8b [46]. In figure 2.8a it is possible to see, from the outside to the inside, the metal vessel (the gray profile that delimits the perimeter of the image), the light reflector sheets of the veto in blue, the anode and cathode surfaces in PMMA covered in Clevios™in pink, respectively, the walls of the neutron veto (in gadolinium-loaded PMMA) and finally the internal volume of the TPC, surrounded by a reflective cage (in gray). In figure 2.8b, a view of the veto walls is shown with detail on the vPDUs, which are the Photo Detection Unit modules of the veto (the golden squares on the walls) [46]. There are 528 PDUs for the TPC which form two optical planes of 264 each. Each PDU consists in 16 tiles of 5x5 cm^2, which contains 24 SiPM of size 12x8 mm^2 each. Four of such tiles form one readout channel that covers 10x10 cm^2 area. There are 120 vPDUs for veto (with the same form factor), 20 on top, 20 at the bottom, and 10 on each of the 8 TPC side barrel walls.

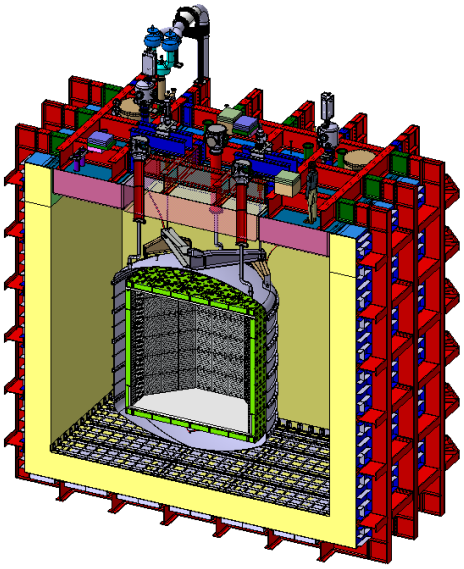

Figure 2.7 – An overview of the DarkSide-20k detector. In the figure, all the parts of the detector can be seen. From the outside: the outside of the cryostat is depicted in red, the insulating layer in yellow, while a metallic vessel is depicted in gray inside which, in green, is the neutron veto, which forms the structure of the TPC, where the active volume for WIMPs detection is located.

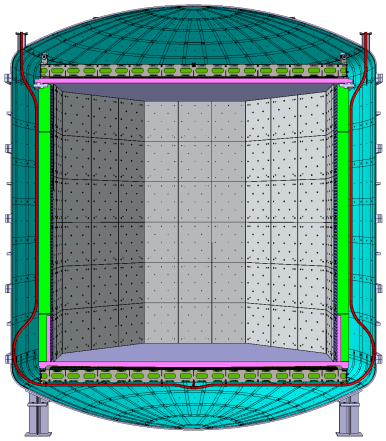

(a) Detail of a section of the stainless steel vessel, the neutron veto, and the TPC.

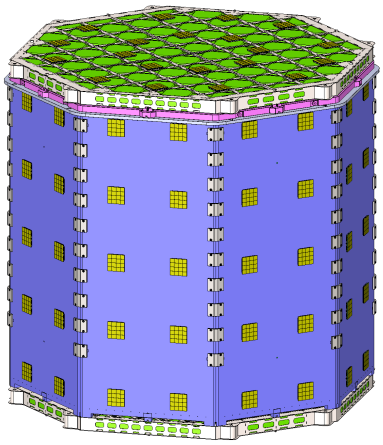

(b) External view of the walls of the Veto with the veto PDUs.

2.3.1 Background control requirements

As already discussed, in this kind of experiment one of the crucial points is to keep under control the background level that could induce competitive signals to those of the desired target or, even, indistinguishable from the event itself. In the direct search for DM, the interaction's cross-sections are dramatically low; in absence of targeted mitigation strategies, the background would completely

spoil the experiment sensitivity. This involves the need to subject each detector material to careful screening to identify traces of isotopes whose decay could lead to the production of unwanted particles. Above all, some isotopes must be kept under constant control by the DarkSide collaboration, since they are naturally abundant primordial radionuclides [47]:

- ^{238}U, which arises a decay chain (described in figure 2.9).
- ^{232}Th, also arises a decay chain (described in figure 2.9).
- ^{40}K, which at 90% decays by emitting a β-particle, while at 10% it emits γ particles

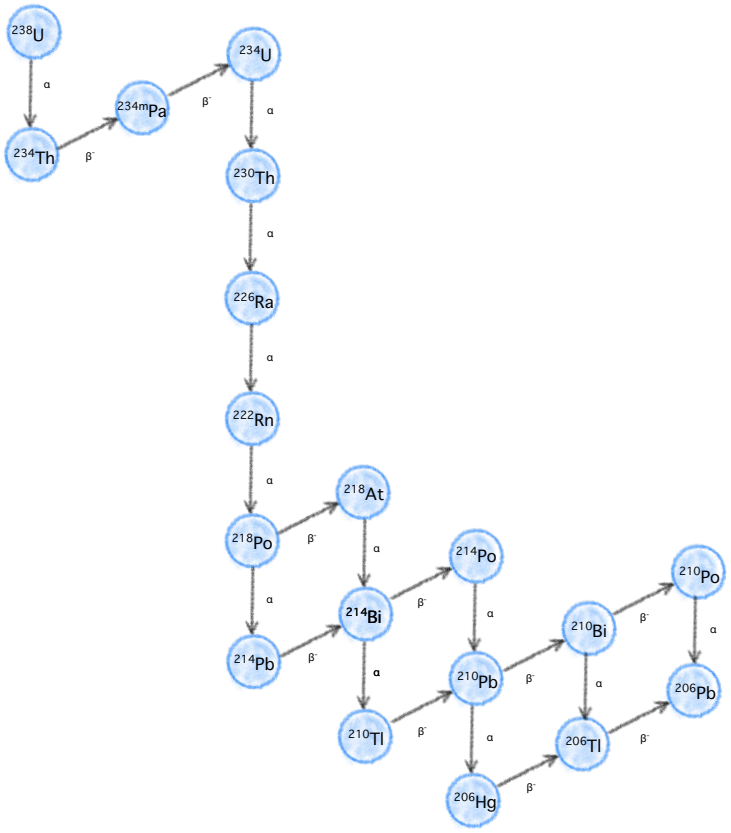

Figure 2.9 – Decay chain of ^{238}U. The chain segment that goes from ^{238}U and ^{230}Th is considered the upper part, while up to ^{214}Po is considered the middle, and, finally, from ^{210}Pb it is considered the lower part.

As mentioned above, isotopes such as ^{238}U and ^{232}Th have complex decay mechanisms, which are characterized by chains, in which multiple unstable isotopes are produced (accompanied by emissions of various particles). The decay of ^{238}U is illustrated in figure 2.9, that for ^{232}Th in figure 2.10.

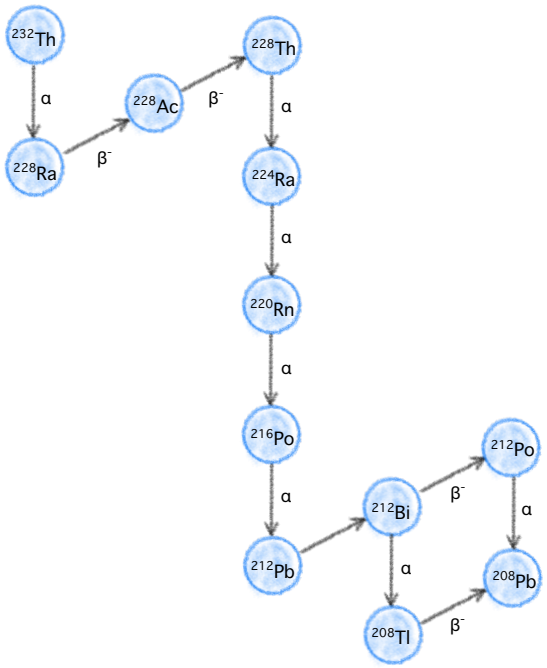

Figure 2.10 – Decay chain of ^{232}Th. The chain segment that goes from ^{232}Th and ^{228}Ac is considered the upper part, while up to ^{212}Pb is considered the middle part. The subsequent decays, finally, are considered to be in the lower part.

Usually, these decays are divided into several parts (typically referred to as upper, middle, and lower parts). Measurements of contamination from these isotopes refer to different parts of the chain, as they can be more or less sensitive to different parts. In order to precisely identify the level of contamination, the practice in the DarkSide collaboration foresees the use of three different techniques, namely Inductively Coupled Plasma Mass Spectrometer (ICP-MS) [48], High Purity germanium detector screenings (HP-Ge) and polonium extraction. The ICP-MS determines the concentration of an isotope in a sample, since it measures the mass/charge ratio, while HP-Ge counts the decays due to certain isotopes [49]. Finally, the polonium extraction technique is particularly useful in determining the concentration of ^{238}U, especially as regards the lower part of its decay chain (as shown in figure 2.9) [50].
In the next sections, I will describe in detail the background sources of the DarkSide-20k experiment.

Alpha particles

Alpha particles are ^{4}He nuclei (so, basically, bound systems of two neutrons and two protons), that are emitted by heavy nuclei which have too many nucleons

to be stable. The emission of these agglomerates can be more favorable due to the high binding energy of the α-particle. The emission of the particle occurs according to the mechanism reported in equation 2.10 [51].

$$(Z, A) \rightarrow (Z-2,\ A-4) + \alpha \tag{2.10}$$

Generally, α-particles have energies in the range of the order of the MeV. Because of their high charge ($+2e$), usually they are characterized by a high energy loss per unit of distance traveled in the matter (in the air they have a range of just a few centimeters), therefore they are not strictly part of the background for DarkSide (because they are outside the energy region of interest), unless they emit neutrons through reactions (α, n) (see an example in equation 2.11) [52], or they are in the form of grains of dust: in this case, because only a small portion of energy was released in LAr, it could give rise to a signal indistinguishable from that of a WIMP.

$$\alpha + {}^{13}\mathrm{C} \rightarrow {}^{16}\mathrm{O} + n \tag{2.11}$$

While they do not make up a significant part of the background, they are still a nuisance to the experiment. Therefore, to avoid α emitters, purification strategies are carried out from the elements that could induce these decays (as it happens for UAr for the ^{39}Ar).
Furthermore, the possibility of the spatial reconstruction of events is exploited, in such a way as to exclude from the signals the events that occurred near the walls, where the decay products of α-emitters could accumulate.

Radiogenic neutrons

Radiogenic neutrons are the most dangerous background source in this experiment. The main source of radiogenic neutrons background in DarkSide-20k is the cryostat foam and the alpha n reactions due to the impurities naturally present in the gadolinium compounds [46] in PMMA. There are some ways to avoid disturbances due to this phenomenon: firstly, decide to exclude from the signals of interest those due to multiple recoils (since the probability that a WIMP makes multiple recoils is approximate to zero, therefore the event is due to a radiogenic neutron). Another way could be to introduce the use of specific devices for the capture of unwanted particles (the so-called "vetos"), as in the case of DarkSide, whose TPC surrounded by a neutron veto loaded with specific additives for neutron capture. The efficiency of these devices is directly related to the probability of neutron capture.

Muons and cosmogenic neutrons

Muons are the result of the interaction of cosmic rays with the atmosphere. These particles are typically shielded by the location of the detector itself (in rare event physics, detectors are located underground, where muons are shielded by the overlying rock). This allows the muon rate to be reduced by a factor of 10^6 in Hall C at LNGS, but this is not enough, since the residual muon flux is equal to $(3.432 \pm 0.003) \cdot 10^{-4} m^{-2} s^{-1}$, as measured by the Borexino experiment during its data taking [53]. Furthermore, muons interacting nearby the materials of a detector can produce cosmogenic neutrons, which are a dangerous background source. The possible sources of neutron background have been calculated on the basis of the most updated data available and thanks to Monte Carlo simulations, and are listed in the table 2.1 [46].

Neutron background source:	Background events in the region of interest [200 t·year]$^{-1}$:
(α,n) neutrons from U and Th	$9.5 \cdot 10^{-2}$:
Fission neutrons from ^{238}U	$< 2.3 \cdot 10^{-3}$
Neutrons from ^{222}Rn diffusion and surface plate-out	$1.4\ 10^{-2}$
Cosmogenic neutrons	$6.0 \cdot 10^{-1}$:
Neutrons from the lab rock	$1.5 \cdot 10^{-2}$
Random surface α decay + S2 coincidence	$5 \cdot 10^{-2}$

Table 2.1 – Neutron sources in the DarkSide-20k experiment. As it can be seen, cosmogenic neutrons are the main source of unwanted NR events.

For this reason, additional shielding to the neutron veto system (consisting of AAr) must be added to the detector [46].

Beta and gamma particles

Beta particles are electrons (or positrons) emitted following the decay of a neutron or proton into a nucleus containing an excess of that nucleon to be stable (see equation 2.12). Their energy interval goes from ≈10 keV to MeV.

$$\begin{aligned} n &\rightarrow p + e^- + \overline{\nu} \\ p &\rightarrow n + e^+ + \nu \end{aligned} \tag{2.12}$$

In the DarkSide-20k experiment, the main source of β particles are the ^{39}Ar nuclei (see equation 2.9), and this is a serious issue because they produce electrons in the active part of the LAr volume. Instead, γ rays are mainly produced by sources external to the detector, but those produced by construction materials, in any case, are not negligible. Their danger lies in their high penetrating power: the shielding of the detector can in fact attenuate its energy, but does not guarantee

the insulation of the TPC. Since, in both cases, the interaction of the particle is associated with ER events, it is possible to recognize them thanks to the argon PSD (as described in section 2.2.2), but a large number of these events can induce problems of dead time and pile-up, which would therefore affect the performance of the experiment, as mentioned in section 2.2.3.

Neutrinos

Neutrinos produce NR due to elastic (or coherent) scattering on argon nuclei, thus introducing an unavoidable background source. In the DarkSide-20k experiment, however, the region affected by the background induced by neutrino scattering is outside the DarkSide exploration window, even though 3.2 coherent neutrino scattering events are expected which cannot be rejected (see section 2.3.3 for further information).

2.3.2 The neutron veto

Since, as discussed, neutrons are the most dangerous source of background, a detector entirely dedicated to them has been developed. One of the peculiar characteristics is the fact that the neutron veto constitutes the walls of the TPC and both the TPC endcaps, guaranteeing coverage at 4π. A cross-section of the veto and TPC is shown in figure 2.11.

The DarkSide-20k neutron veto is made up of materials that allow the slowing of

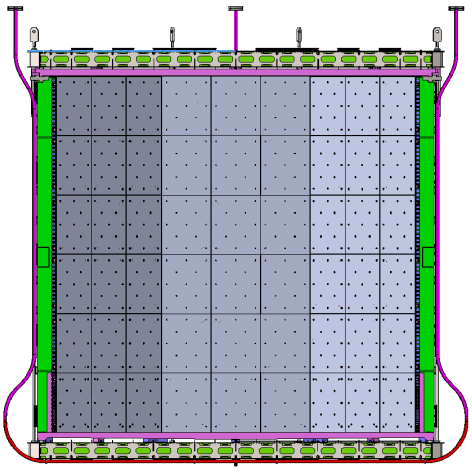

Figure 2.11 – Open view of a section of the TPC and the veto of the DarkSide-20k experiment. Gd_2O_3 loaded PMMA parts are in green: so the veto walls and the endcaps. The pipes are used for calibrations. The veto photosensors are placed on the external surfaces of the endcaps.

incident neutrons (a process known as moderation) and, once thermal energies

are reached, the capture of the aforementioned neutrons, with subsequent emission of γs which then interact with LAr, finally giving rise to a signal which is then detected by the photosensors. The working principle of the DarkSide-20k veto is schematized in figure 2.12. The materials involved in the neutron

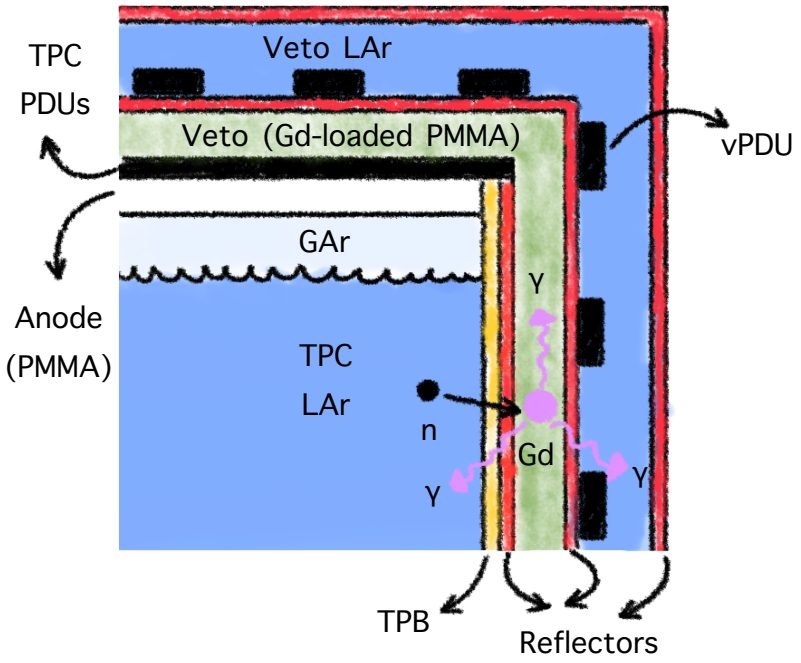

Figure 2.12 – The veto working principle (not in scale), with the main parts of the inner detector. When a neutron (the black particle) passes through the veto (the part in green), is moderated and then captured by gadolinium, resulting in the emission of γs that interact with the UAr of the veto (in blue). The signals that follow these signals are then detected by dedicated veto photo sensors (vPDUs).

veto are polymethyl methacrylate (PMMA) and gadolinium. PMMA, with its hydrogen-rich composition (see structure formula in figure 2.13), allows neutron moderation. The use of polymers-based materials as neutron moderators is widely addressed in different scientific fields [54], [55]. The choice of PMMA comes from a variety of reasons, which include:

1. stringent radiopurity criteria (since PMMA can be produced with excellent radiopurity standards [56]), and this is due to the possibility to obtain methyl methacrylate (MMA), i.e. the starting monomer, with an excellent degree of radiopurity.

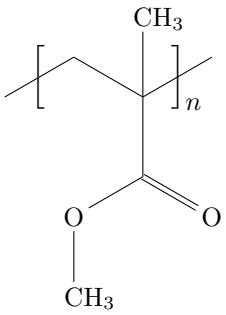

Figure 2.13 – Structure formula of polymethyl methacrylate.

2. in order to minimize the number of materials in the detector for the reasons of point 1, another criterion is the compatibility of the material veto with that of TPC optical windows (and in this case PMMA is indicated due to its transparency, which is necessary for the correct functioning of the TPC optical windows, as illustrated in section 1.4)

3. the resistance of the material in cryogenic environments, already tested by experiments like DEAP-3600 [57].

Gadolinium, on the other hand, has a high cross-section for thermal neutron capture (see table 2.2 [58]).

Isotope	n capture cross-section [barn]
^{1}H	0.3326
^{157}Gd	$2.57 \cdot 10^{5}$

Table 2.2 – Neutron capture cross-section values for the most common isotopes of hydrogen and gadolinium. For hydrogen, the isotopic abundance is equal to 99.9844%, while for ^{157}Gd it is equal to 15.65%.

Hydrogen has a mass comparable to that of the neutron, therefore when a neutron with certain energy collides with a hydrogen atom, part of the energy is transferred to the latter, according to the process shown in figure 2.14 [59]. When the neutrons reach thermal energies they are then captured by the gadolinium nuclei, according to the process reported in equation 2.13.

$$n_{th} + {}^{157}\text{Gd} \rightarrow {}^{158}\text{Gd} + N\gamma \tag{2.13}$$

The overall process leads to the emission of a certain amount (marked with N, which is equal to 3 or 4) of γs carrying energy up to 7.9 MeV [60]. These γs then interact with the LAr, resulting in the emission of light which is wavelength shifted at 420 nm, using 1,1,4,4-tetraphenyl-1,3-butadiene (TPB, see structure formula om figure) coatings in the veto and polyethylene naphthalate (PEN,

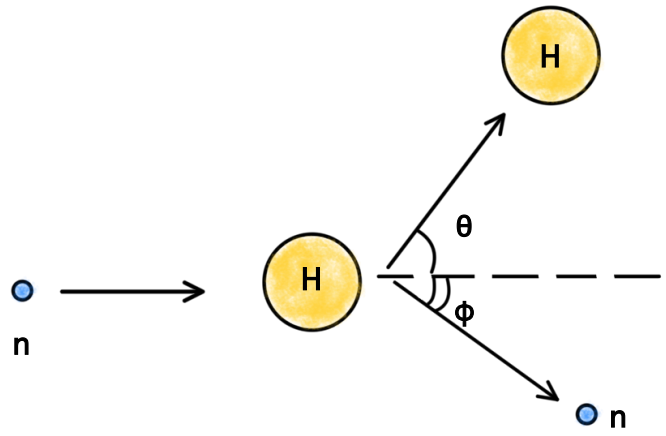

Figure 2.14 – Neutron moderation scheme by the hydrogen atoms present in the polymeric matrix.

see structure formula in figure 2.16) foils in the TPC, and then detected by the SiPMs.

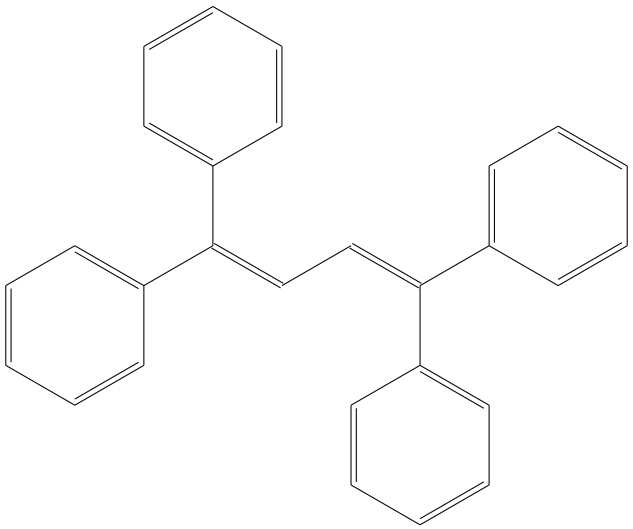

Figure 2.15 – Structure formula of 1,1,4,4-tetraphenyl-1,3-butadiene.

In order to understand what was the correct concentration of gadolinium in the polymer matrix to maximize the neutron detection efficiency, Monte Carlo simulations were conducted (see figure 2.17, [46]). These simulations use radiopurity screenings carried out at the collaboration facilities as ingredients. If the screenings have been able to set only upper limits, these values are taken as a reference for the simulations, since they represent the worst-case scenario. The

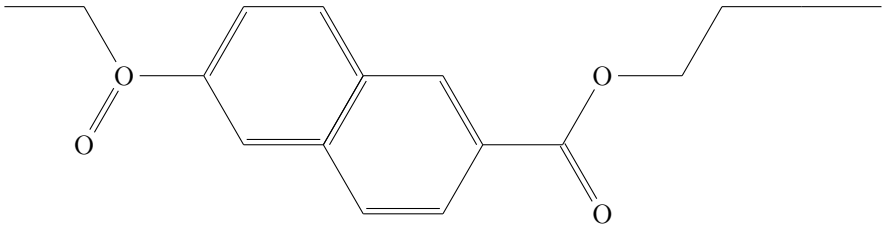

Figure 2.16 – Structure formula of polyethylene naphthalate.

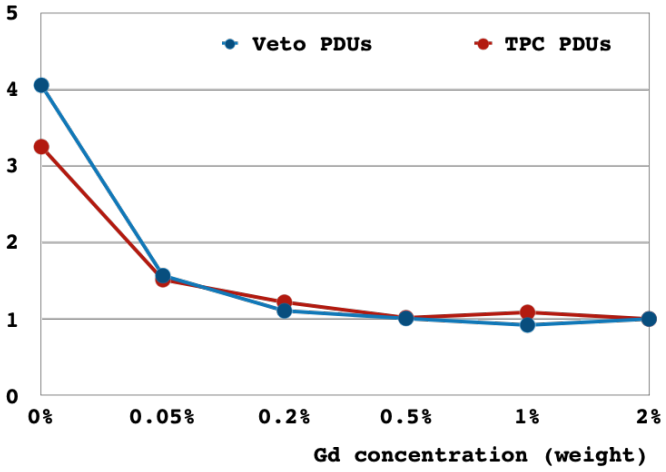

Figure 2.17 – Relative inefficiency of neutron tagging versus the gadolinium concentration in mass for neutrons generated by the contamination carried by the constituent materials of the PDUs. The curves are normalized to have a value of 1 at the concentration value of 2%.

Monte Carlo simulations showed that the achievement of maximum efficiency occurs at concentrations between $0.5\%_w$ and $1\%_w$ (with respect to the mass of the PMMA). For reasons of background minimization induced by any gadolinium impurities, it was decided to converge on a nominal value of around $1\%_w$, also taking into account any non-homogeneity of the gadolinium distribution.
For the realization of all the components of the mechanical structure of the veto, roughly 20 tonnes of material are required. The development of such a large mass of an innovative material brings with it numerous challenges, including fine-tuning the material at the laboratory scale, transferring the technology to one partner industry, and, finally, controlling the cleanliness of the environment of production to avoid any contamination during polymerization. This thesis work fits into this context.

2.3.3 Expected sensitivity

As was hinted at for the LZ and XENON experiments, based on the exposure time of the experiment and the particle cross-section, the detector is capable to explore different regions and different possible masses of the particle. In figure 2.18a, it is possible to see the 5σ (so with an uncertainty of about $3{\cdot}10^{-7}$) expected discovery plot of DarkSide-20k, comparing it with what it was previously seen for LZ and XENONnT, while figure 2.18b shows the discovery plot at 90% confidence level [46]. Notice that the nominal run time of the DarkSide-20k

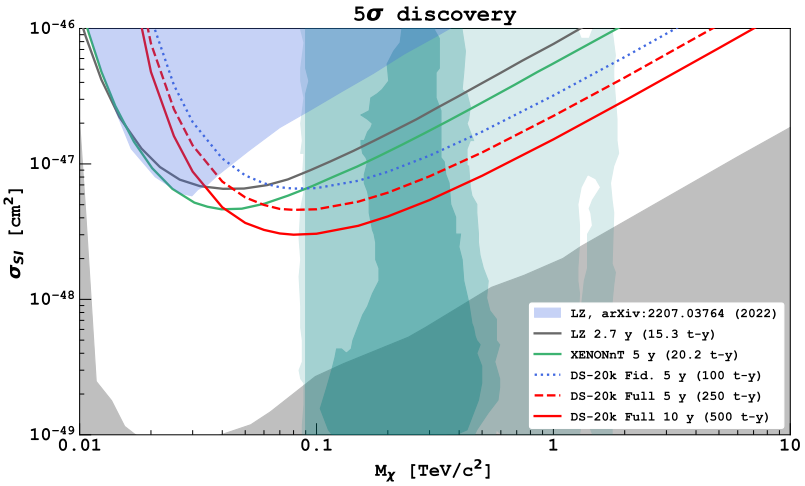

(a) Detection areas exploited by the DarkSide-20k experiment at 5σ discovery.

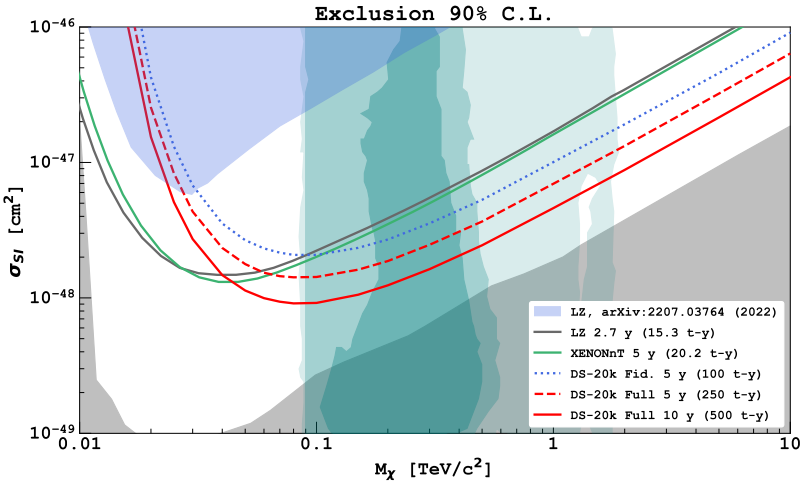

(b) Detection areas exploited by the DarkSide-20k experiment at 90% confidence level.

Figure 2.18 – Expected sensitivity of the DarkSide-20k experiment.

detector is 10 years, corresponding to an exposure of the fiducial volume (20 tonnes of UAr) of 200 tonnes·year (the dashed blue line in the plots). The region in grey represents the so-called neutrino floor (that is the region where coherent scattering from atmospheric neutrinos starts contributing to the background rate) in argon, while the turquoise area underlines the most favored areas for the WIMP mass (at 1σ, 2σ and 3σ) for some specific models [61]. The area above the green line is the region excluded by XENON1T, as was shown in section 1.5.2. The median sensitivity of the DarkSide-20k experiment shown in figure 2.18a and figure 2.18b is calculated using a profile likelihood approach and it is based on a Monte Carlo simulation to predict the event rate in the WIMP region of interest, in which systematic uncertainties affecting the various sources of backgrounds are taken into account. The projected sensitivity are $6.3{\cdot}10^{-48}$ cm^2 for the 90% confidence level exclusion and $2.1{\cdot}10^{-47}$ cm^2 for the 5σ discovery for a WIMP mass of 1 TeV/c^2. As shown in the plots, DarkSide-20k with a 5-year data taking (blue dashed line) would cover and extend the limits explored by LZ and XENONnT for WIMP masses above 0.1 TeV/c^2.
Through an analysis that takes into consideration the overall instrumental background of all the active volume of the DarkSide-20k detector (using the full mass of LAr), it would be possible to reach an exposure of 500 tonnes·year and, therefore, achieve greater sensitivity. The consequent sensitivities would be $4.6{\cdot}10^{-48}$ cm^2 for the 90% confidence level exclusion and $1.5{\cdot}10^{-47}$ cm^2 for the 5σ discovery of a 1 TeV/c^2 WIMP, that is much beyond current. This result is evidenced by the red dashed line in figure 2.18a and figure 2.18b. This would lead to the discovery or the confirmation or exclusion of the DM hypothesis of the WIMP, down to the level of the neutrino floor. Moreover, if LZ or XENONnT were to measure a DM signal during their operation, with a nominal acquisition duration of 2.7 and 5 years respectively, DarkSide-20k is the only detector, to date, that could confirm this result. This aspect would be crucial in the perspective of a historical discovery such as that of the confirmation of the hypothesis of the WIMP.

Chapter 3

The gadolinium oxide R&D

For the realization of the neutron veto, the DarkSide collaboration has given rise to several R&D projects for the development of the gadolinium doped PMMA. As illustrated in the previous sections, any material entering the detector must meet stringent radio purity requirements. Therefore, the selection of the raw materials for the realization of the veto was carried out with careful screening procedures to verify if these raw materials met the requirements. Starting from this, three R&Ds were conducted, both with compounds containing inorganic gadolinium and with organometallic-based compounds. Specifically, three candidate compounds were selected:

- Gadolinium oxide in the form of NPs (Gd_2O_3) (see the structure formula in figure 3.1). Several samples of Gd_2O_3 in the form of NPs have been purchased from different companies and have been screened using the collaboration facilities. Finally, it was found a company capable to provide a radiopure enough material, which was then used for the R&D. The selected producer company is called Shin-Etsu [62]. Despite the simplicity

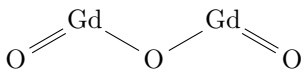

Figure 3.1 – Structure formula of gadolinium oxide.

  of the supply, the biggest obstacle consists in the non-solubility of the NPs in the liquid monomer (methyl methacrylate, MMA), which involves the sedimentation of the solute and, consequently, the production of solid samples with an inhomogeneous concentration of gadolinium

- Gadolinium acetylacetonate anhydrous ($Gd(C_5H_8O_2)_3$) (see the structure formula in figure 3.2), [63]. This compound is produced from gadolinium oxide [46], passing through many steps, which allow performing purifications of the compound. However, the anhydrous compound must be

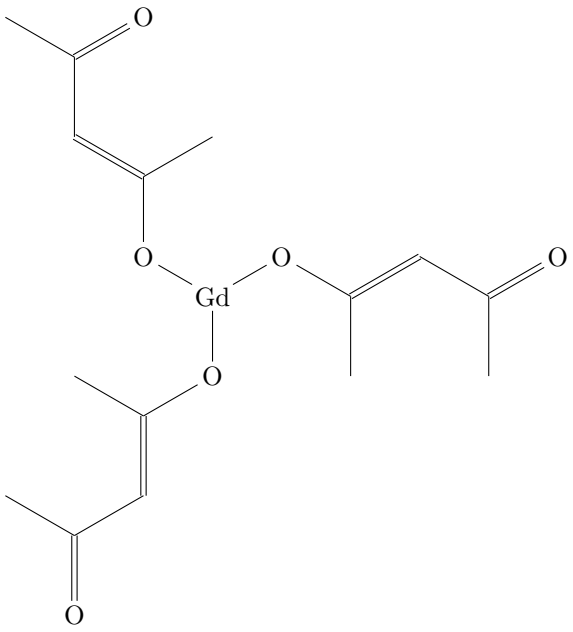

Figure 3.2 – Structure formula of anhydrous gadolinium acetylacetonate.

treated very carefully to keep it away from moisture, so its introduction into an industrial chain is quite complex.

- Gadolinium methacrylate ($C_{12}H_{18}GdO_6$) (see the structure formula in figure 3.3) [64]. Also, this compound is produced starting from gadolinium oxide, also in this case it is therefore possible to select the most radiopure supply. The making of this compound is proprietary, as well as the process

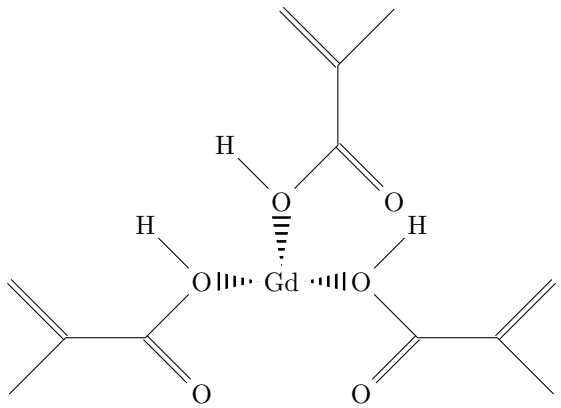

Figure 3.3 – Structure formula of gadolinium methacrylate.

that makes this compound soluble in MMA. However, the solubility is guaranteed by the manufacturer. The biggest problem lies in the impossibility of obtaining information on the production process of the compound and

on any additives used, therefore the final samples must be screened to find out if the radiopurity levels are satisfactory. In any case, it is possible to screen the finished products for radiopurity.

The veto group in Genoa was involved in the R&D on gadolinium oxide, which is the essence of this work. I will then report the extensive R&D work that I did, bringing the Gd_2O_3 option to a stage that can be transferred to the industry for final production.

3.1 Gadolinium oxide

Gadolinium oxide (Gd_2O_3) is a very stable inorganic molecule, and it is one of the most common gadolinium-based compounds. Some of its properties are listed in table 3.1. In our specific case, it was decided to use Gd_2O_3 in the form of NPs, to favor the dispersion in MMA, the liquid monomer. All the details about the mixing procedure will be described in the next sections. The typical dimensions of the chosen NPs are reported as well in table 3.1. Gadolinium oxide does not have particular indications of safety or toxicity and can be handled easily [65]. Gadolinium oxide can be produced through the thermal decomposition of

Property	Description
Chemical formula	Gd_2O_3
Form	NPs
Molar mass	362.50 g/mol
Gd mass fraction	0.868
Appearance	white odorless powder
Density	7.4 g/cm^3
Melting point	2420°C
NPs diameter	20-80 nm

Table 3.1 – Gadolinium oxide main properties

oxalates, nitrate, hydroxide, or carbonate, and it constitutes itself on the surface of metallic gadolinium. There are several fields of application for this compound, including [66], [67]:

- Production of fluorescent materials and luminescence and electroluminescence devices
- Realization of UV detectors
- Contrast medium for biomedical imaging
- Chemical catalysis
- Detector of thermal neutrons

Regarding the latter use, in the literature the use of nanocrystals based on gadolinium oxide is reported [68], since the high thermal neutrons capture cross-section (as reported in paragraph 2.3.2).
The main issue with this compound is represented by its non-solubility in the liquid monomer methyl methacrylate (MMA). Consequently, in order to use this compound (for its availability and the possibility of production with good radiopurity), it is necessary to find a suitable mixing and polymerization procedure. In the next sections, I will illustrate both the strategy used to obtain products with a satisfactorily homogeneous concentration of gadolinium oxide and our polymerization procedure. For clarity, I will divide the two steps.

3.2 NPs functionalization

As it will be shown in chapter 5, Gd_2O_3 NPs exhibit good radiopurity and are commercially available.
The state of the art in the realization of gadolinium oxide NPs dispersions in polymeric matrices is very poor in literature, except for the realization of polymeric thin films containing gadolinium [69]. Some processes of incorporation of transition metal oxides into polymeric matrices (such as, for example, titanium oxide, [70]) have been investigated. There are different approaches that could be followed in order to obtain a homogeneous distribution of NPs in a polymeric matrix, such as solution casting, which might be a good procedure when the NPs are not soluble in the monomer [71], [72]. Nevertheless, for this application, the most convenient approach is to polymerize MMA with the NPs, since the construction of the DarkSide-20k veto requires roughly 20 tonnes of material (as illustrated in section 2.3.2), so the procedure must be simple enough to be scalable to the industry, but most importantly, because of the stringent radiopurity requirements of the DarkSide-20k experiment, it is preferable to identify a procedure which allows the radiopurity of the product to be controlled, and this would not be possible, for example, in the solution casting process, since in that case it would not be possible to control the radiopurity of the pellets. The use of the MMA monomer instead of PMMA, on the contrary, allows to keep the radiopurity of the final product under control [73], [74].
In order to avoid sedimentation, the adopted procedure involves functionalizing the surface of the NPs (or NPs clusters), to establish repulsive forces that help to counteract sedimentation, thus obtaining colloidal solutions that remain stable on time scales compatible with the polymerization times of PMMA. In our case, two functionalization procedures were investigated: one with octylphosphonic acid and one with Igepal CO-520®.

3.2.1 Octylphosphonic acid

To perform a functionalization of the NPs with the acid, the following procedure was developed, following what was found in the literature for the realization of coatings on TiO_2 particles [70]: first, a certain amount of gadolinium oxide was withdrawn and brought into solution with deionized water. Thereafter, this solution was sonicated for 30 minutes. Then a solvent composed of methanol and deionized water in a 3:1 ratio was added to the solution, together with a certain amount of octylphosphonic acid (see the structure formula in figure 3.4). This solution was then again subjected to 40 minutes of sonication and then

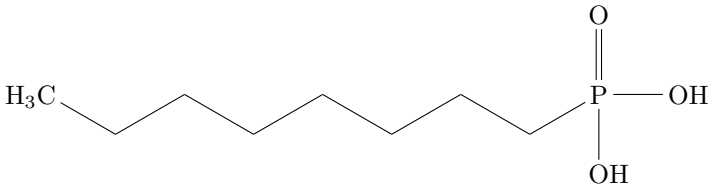

Figure 3.4 – Structure formula of octylphosphonic acid.

left under mechanical stirring for about 72 hours. Afterward, the solution was centrifuged, the solute was washed three times with acetone to remove excess acid, and, finally, centrifuged again after each wash. Finally, the solute was left to dry in an oven for one night at 60°C.
To evaluate the validity of the mixing procedure, it was decided to carry out an infrared spectroscopy analysis on the untreated gadolinium oxide, on the acid, and finally on a treated sample, to verify the presence of the characteristic peaks on the latter of both contributions. One of the performed IR spectra is shown in figure 3.5. As can be seen from the graph, the presence of octylphosphonic acid in the treated sample is evident.
Unfortunately, the stability of the NPs in MMA was not improved by the acid: the sedimentation still occurred in a few seconds. So it was decided to investigate other options.

3.2.2 Igepal CO-520

As attempts to treat the NPs proved unsatisfactory in terms of stability, it was decided to try another commercial surfactant, namely Igepal CO-520® (see the structure formula in figure 3.6), by Merck.

In the first place, it was simply decided to replace it with acid, leaving the procedure unchanged; some quantities of gadolinium oxide were then taken, subjected to sonication for 30 minutes in deionized water, then incorporated into the solvent consisting of methanol and deionized water and, after mechanical stirring, the centrifuge was carried out. Similarly to what was done with octylphosphonic acid, the effectiveness of the procedure was first evaluated

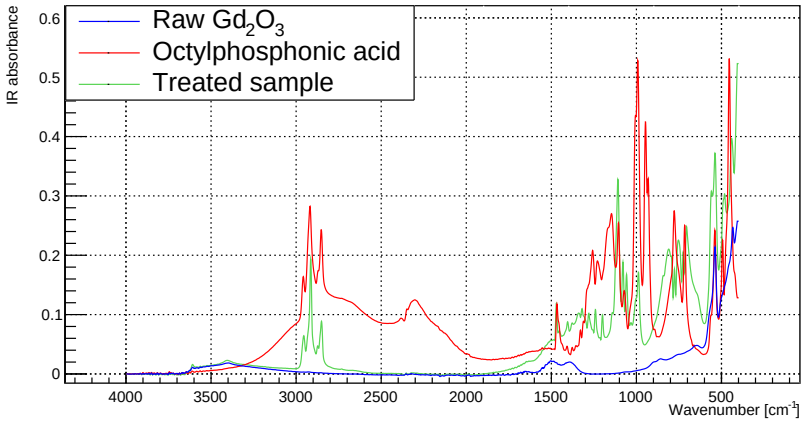

Figure 3.5 – Comparison of the IR spectra of Gd_2O_3, octylphosphonic acid, and a treated sample. As it can be seen, the contribution of gadolinium oxide is evident for high wave numbers, around 3500 cm^{-1}, and at 1500 cm^{-1}, where however it is covered by the contribution of the acid (as happens in 500 cm^{-1}). On the treated sample, however, the presence of both characteristic peaks is evident. As for the acid, its presence is denoted by the peaks in the area between 500 and 1500 cm^{-1} (peaks completely absent in the spectrum of pure Gd_2O_3), and in the area around 3000 cm^{-1}.

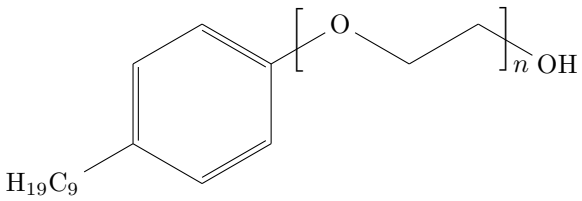

Figure 3.6 – Structure formula of Igepal CO-520. The repetition number n is ≈ 5.

thanks to IR spectroscopy. The spectra are shown in figure 3.7. As can be seen from this figure, there is no evidence of the presence of Igepal. This phenomenon has been attributed to the mixing procedure, as it is a different surfactant from octylphosphonic acid from the one for which this procedure was carried out. Therefore, it was decided to review this procedure, starting with the final washes with acetone (as with this technique most of the surfactant was washed away). Therefore, modifications were made to the mixing procedure to produce samples with a good surface treatment of the NPs. First, acetone washes after spinning were eliminated. The effectiveness of this modification was again tested with IR spectroscopy, the results are shown in figure 3.8. Still, the presence of surfactant is still rather scarce. Therefore, it was decided to further modify the mixing procedure. The definitive procedure has therefore been reached, more suited to our purposes and with the most satisfactory results. It involves the preparation of a solution containing a certain quantity of gadolinium oxide, an equal mass of Igepal in 2-butanone solvent (see the structure formula in figure 3.9). The

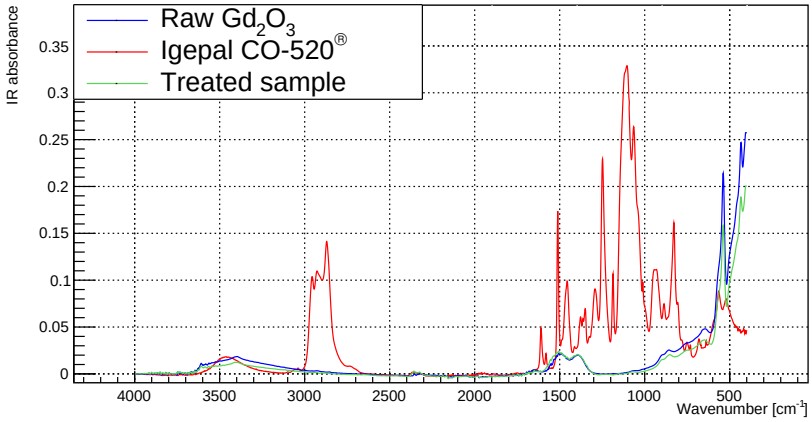

Figure 3.7 – Comparison of the spectra of raw Gd_2O_3, Igepal, and a treated sample. As can be seen, the Igepal has some characteristic peaks located in a spatial frequency range between 700 and 1600 cm^{-1}, between 2600 and 3000 cm^{-1}, and around 3500 cm^{-1} (here, however, the peak is at a lower intensity than that due to gadolinium oxide). All these families of peaks are in no way found in the treated sample, which has an IR spectrum almost identical to that of gadolinium oxide.

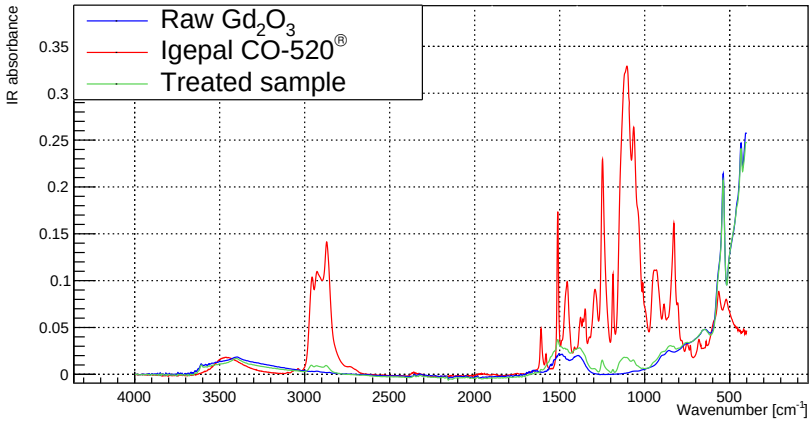

Figure 3.8 – Comparison of the spectra of raw Gd_2O_3, Igepal, and a treated sample. Unlike the previous sample, it is possible to see a weak presence of some characteristic peaks of the surfactant on the treated sample (for example in the range between 1000 and 1500 cm^{-1} and around 3000 cm^{-1}).

butanone was chosen as a common low-boiling organic solvent, being though compatible with the developed polymerization procedure, described in section 3.3. The solution is then subjected to sonication for the disintegration of any aggregates of NPs and to favor the adhesion of the surfactant. This procedure leads to the creation of stable colloidal solutions on time scales of the order

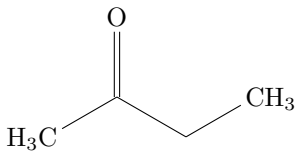

Figure 3.9 – Structure formula of 2-butanone.

of 24-25 hours. The presence of the surfactant was again evaluated with IR spectroscopy, taking a solution of Gd_2O_3, Igepal, and butanone and leaving it to dry in an oven, in order to remove the solvent. The results are shown in figure 3.10. In this case, it is possible to notice both the characteristic peaks of the

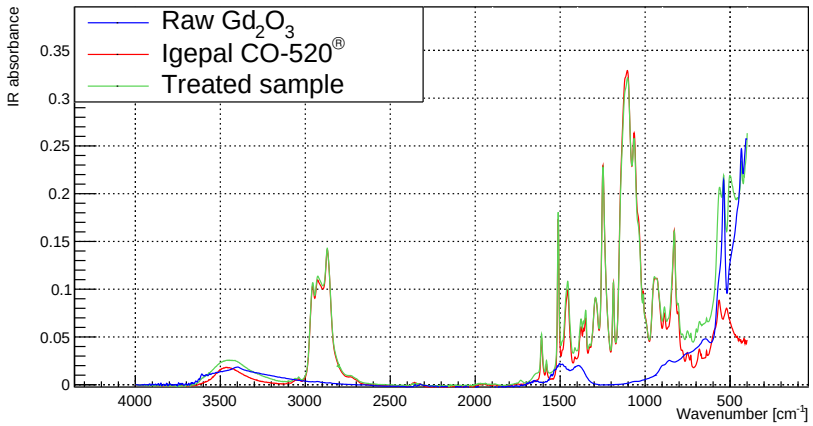

Figure 3.10 – Comparison of the IR spectra of raw Gd_2O_3, Igepal, and a treated sample. In this case, the successful adhesion of the surfactant is shown by both the peaks of the Gd_2O_3 (at low spatial frequencies, around 500 cm^{-1}) and the surfactant peaks, in the ranges between 700 and 1500 cm^{-1} and between 2600 and 3000 cm^{-1}.

surfactant and of the Gd_2O_3: this result suggests that in this case the surfactant was not washed away, but it is present on the NPs surface.
The effect of this mixing procedure is visible in figure 3.11, which shows a Dynamic Light Scattering (DLS) measurement carried out on a treated sample, using 2-butanone as a solvent. From the figure it is possible to observe how, thanks to the mixing procedure developed, it is possible to obtain stable colloidal suspensions after 110 minutes: this time scale is compatible with our polymerization strategy. The surfactant's effect is also visible macroscopically, as shown in figure 3.12. This procedure was subsequently tested during the polymerization phase and allowed the production of samples of satisfactory homogeneity.

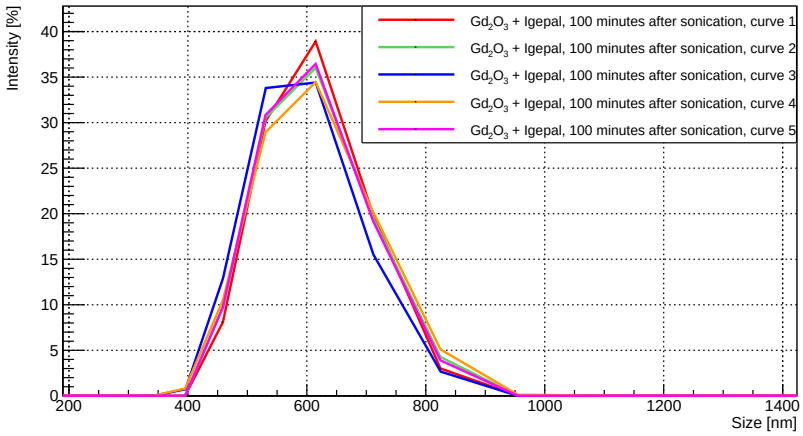

Figure 3.11 – DLS measurement performed on a Gd_2O_3 sample treated with Igepal CO-520®. This experiment plot consists of five different measurements and each one is obtained through an average of 13 runs. This experiment was performed 110 minutes after the sample's preparation.

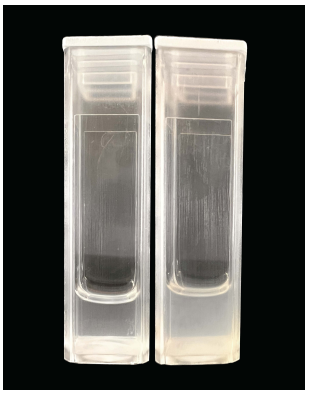

Figure 3.12 – Macroscopic evidence of the effect of surfactant on the stability of colloidal suspensions. On the left, there is a cuvette containing a solution containing just Gd_2O_3 NPs in 2-butanone, while on the right there is a cuvette containing Gd_2O_3 NPs treated with Igepal in 2-butanone. With the same concentration of NPs, the solution on the right appears more opaque, while the other is more clear, and this is symptomatic of the sedimentation of the NPs.

3.3 Polymerization procedure

The first polymerization tests proceeded almost in parallel with the mixing and surface treatment tests of the NPs. After a literature search [70], it was learned that the best way for our purposes was the creation of a solution as viscous as possible for the dispersion of NPs in the liquid monomer (MMA) avoiding sedimentation. Consequently, the procedure was developed also including this

increase in viscosity and, at the same time, trying to reduce the polymerization time as much as possible, to ensure that the formation of the solid structure in a reasonably short time would help the consolidation of a structure as homogeneous as possible (compatibly with the requirements of the DarkSide-20k experiment, see section 2.3.2). For laboratory tests, methyl methacrylate was purchased from the company Merck [75], which is inhibited with hydroquinone monomethyl ether (MEHQ) in amounts $\leq$ 30 ppm. To arrive at the final procedure, tests were conducted to optimize the parameters of the pre-polymerization and the final polymerization. The tests conducted can be divided as follows:

- Optimization of the amount of primary initiator: to create a viscous prepolymer that facilitates the formation of a mechanical dispersion of NPs in MMA, the use of primary initiators such as 2,2'-Azobis(2-methylpropionitrile) (AIBN) [70], whose structure is illustrated in figure 3.13. Typically, the monomer, after being filtered from the inhibitor, is heated and AIBN is added when a certain temperature is reached. The heating has a dual purpose: on the one hand, to favor the increase in viscosity, on the other, since AIBN develops gas while it acts, to speed up the time in which it is consumed, to prevent the residual AIBN from developing gas during the final polymerization, thus leading to defects in the final product. Tests were carried out varying the concentration of AIBN, starting from $1\%_w$, however, such a high concentration led to very rapid polymerizations, but the final products had a very high number of defects, probably induced by the residual AIBN which had not been consumed in the pre-polymerization phase. The possibility of not using the primary initiator, but limiting oneself to the secondary (which does not develop gas), was also examined, but in this case the polymerization was too slow. Finally, it was seen that with 100 ppm of AIBN (calculated with respect to the mass of MMA), satisfactory results were achieved.

- After the pre-polymerization step, a viscous product is obtained, which facilitates the mechanical dispersion of the NPs. To further increase the viscosity, it is possible to carry out a further step, namely quenching, which involves rapidly cooling the prepolymer in a water and ice bath. This can be very useful in case of polymerization from dry powders (section 3.3.1), but it is instead useless in case of polymerization from solution (section 3.3.2). In the final procedure, this step was not implemented.

- In line with what was found in the literature for AIBN, Luperox (lauroyl peroxide, see structure formula in figure 3.14) was chosen as the secondary initiator. Which is added to the prepolymer before going on to the final polymerization. This initiator, unlike AIBN, does not develop gases that affect the quality of the product, therefore the time in which it is consumed

is less critical. Tests have been carried out to optimize the quantity of this initiator, varying its concentration between 400 ppm and 600 ppm (calculated with respect to the mass of the monomer). Following these trials, it was found that 600 ppm is the optimum amount for us, as it results in shorter times for final polymerization.

- Another important parameter is the temperature at which polymerization takes place. There is a vast literature on this subject [76]. including studies on high-temperature polymerizations [77], but in this case the procedure must be simple enough to be scaled up to industry. Furthermore, it is necessary to find a polymerization strategy that is fast enough not to allow the sedimentation of the NPs, but not excessively fast that any residual solvent abruptly evaporates (section 3.3.2), which could lead to defects in the final product. Polymerization tests were carried out at different temperatures (from room temperature up to 80°C). Too high temperatures led to very bubbly samples being obtained, while polymerizations at low temperatures required very long times (in the order of days), and led to completely inhomogeneous samples from the point of view of NPs dispersion. Finally, it was found that the optimum polymerization temperature for our purposes is 55°C. The polymerizations were then carried out in a suitable oven. In order to know the average molecular mass of the polymer obtained with this procedure, viscosimetry measurements were carried out (reported in section 4.5).

- Finally, in the context of liquid polymerization, the amount of solvent (i.e. 2-butanone) and the moment of incorporation of the suspension into the monomer were investigated. A too-high quantity of solvent could be a problem, in fact, since the boiling point of 2-butanone is equal to 80°C, therefore the polymerization temperature (referred to in the previous point) is not high enough to allow evaporation of the solvent, and would therefore lead to final products with residual solvent. Any solvent residues during cooling in cryogenic liquids could cause defects and cracks and compromise the mechanical properties of the object. Numerous tests were therefore carried out (in conjunction with the refinement of the polymerization temperature), polymerizing the product at different temperatures and incorporating the NPs suspension at different times: before and after the pre-polymerization. In the end, it was found that the best solution consists in incorporating the suspension before pre-polymerization, as the high temperatures reached in this phase favor the evaporation of the solvent. Furthermore, the amount of solvent was varied (volumes of 2-butanone equal to those of the monomer were used, until they were progressively reduced). In the end, it has been seen that by keeping the quantity of solvent equal to about 1/4 of that of the monomer, satisfactory products

are obtained with little residual solvent (for more information on this point, see section 4.1)

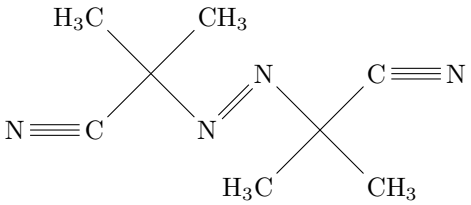

Figure 3.13 – Structure formula of 2,2'-Azobis(2-methylpropionitrile).

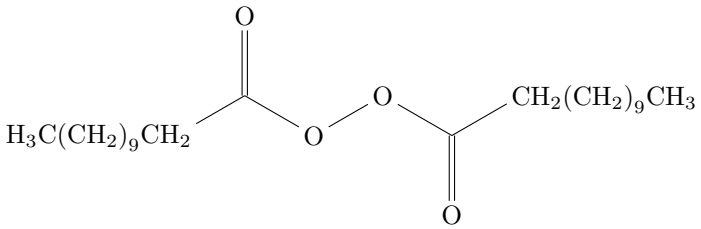

Figure 3.14 – Structure formula of lauroyl peroxide.

The developed procedure foresees the following steps:

1. To remove the inhibitor, the raw MMA is passed through a column containing alumina (Al_2O_3)

2. The monomer is then placed in a becker on a heating plate, where it is brought to 80°C

3. At that point, a quantity equal to 100 ppm of AIBN (purchased by Merck) are added.

4. Since the AIBN develops gas, in order to minimize any bubbles in the final polymer, the solution is brought to about 100°C (i.e. the boiling point of MMA) and left to boil for a few minutes, since AIBN has a half-life of one hour at 85°C (five hours at 70°C) [78]

5. After heating the monomer and consuming the AIBN, it is possible (although not mandatory) to subject the mixture to quenching. This promotes the increase in viscosity and brings the mixture to a syrup-like consistency

6. Afterwards, 600 ppm of the secondary initiator of the polymerization reaction are added (Luperox, by Merck).

7. In the end, the mixture is placed in a muffle furnace at 55°C for 24 hours

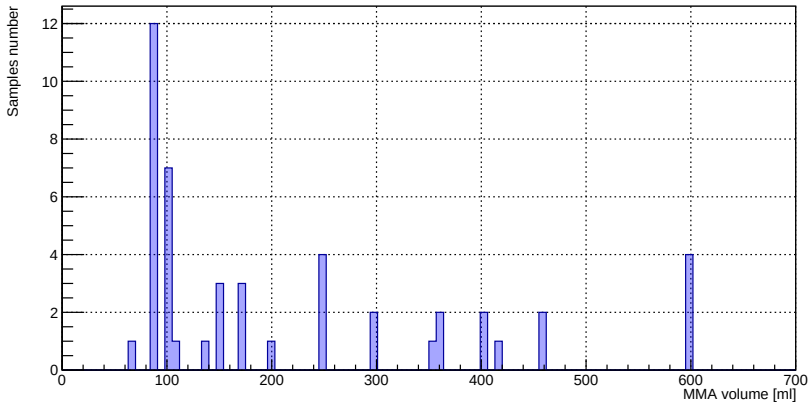

Figure 3.15 – Some laboratory scale samples, depicted according to the volume of liquid MMA used.

During this R&D several samples were produced, varying the mass of the sample. An overview of some of the samples (depending on the amount of MMA used), is shown in figure 3.15.
Note that the introduction of gadolinium oxide is not mentioned in this procedure. This is because all the tests that led to the development of this procedure can be classified into two macro-categories: the polymerization tests starting from powders or starting from solution (following the mixing procedures described in section 3.2).
The polymerization temperature was selected after several investigations (starting from higher temperatures, i.e. 80°C, that led to the formation of many defects in the final products, because the reaction was not under control at these temperatures). In the next paragraphs, I will distinguish the two categories by describing the two different possible strategies.

3.3.1 Polymerization from dry powders

First of all, the path of polymerization of powders produced with the mixing strategy described above was undertaken. These powders i.e. treated and dried gadolinium oxide NPs, were incorporated into a small amount of MMA, subjected to sonication to promote homogeneity, and, finally, this mixture was incorporated into the prepolymer (produced thanks to the procedure illustrated in section 3.3) after quenching, i.e. when the maximum viscosity of the prepolymer was reached. At that point, the viscous solution was stirred manually to promote homogeneity. Later, referring back to the procedure of section 3.3, the solution was placed in the oven in a suitable container, after the insertion of the Luperox. With this procedure, samples were produced starting from powders consisting

of both raw gadolinium oxide and oxide treated with octylphosphonic acid and Igepal. As expected, crude gadolinium oxide undergoes sedimentation, despite the increased viscosity of the prepolymer. The treatment with octylphosphonic acid, despite actually forming a coating on the surface of the NPs, is not sufficiently effective in counteracting sedimentation (since, as in the previous case, there is a marked separation in the concentration of NPs between the bottom and the surface of the sample, to the optical inspection only). For this reason, the mixing procedure with octylphosphonic acid was abandoned after the very first attempts at polymerization.
Regarding Igepal, it was found that the NPs treated with it were more uniformly distributed in the final polymer samples. However, in the samples produced according to the procedure illustrated in the first part of section 3.2.2, there was still a greater tendency to sedimentation, thus confirming what was seen with IR (infrared) spectroscopy, i.e. that the washes in acetone led to the removal of almost all of the surfactant. As regards the polymeric samples produced starting from dried powders, those treated with Igepal and not subjected to washing in acetone were the best. However, the result was still not satisfactory, as concentration gradients were still observed along the height of the sample on visual inspection alone. However, some polymer samples have been characterized to get a quantitative idea of this concentration gradient, as will be illustrated below (see chapter 4).

3.3.2 Polymerization from solutions

Following what was illustrated in the previous paragraph, it was decided to adopt a different procedure, which actually included the integration of a solution containing the NPs treated with the prepolymer. As illustrated in the second part of section 3.2.2, the most satisfactory samples from the point of view of the functionalization of the NPs were prepared by combining the surfactant and the NPs in a suitable solvent; the choice fell on 2-butanone. During the R&D several samples were produced, varying the total mass, the shape, the method, and the concentrations of Gd_2O_3 and Igepal. An overview of some of the produced samples is shown in figure 3.16. The integration of the solution to the MMA was tested at two different points in the procedure illustrated in section 3.3: after quenching the prepolymer and at the beginning, i.e. before heating.
In the first case, in order to obtain a more rigid structure, it was necessary to increase the residence time in the oven or the temperature of the latter, since there was a greater probability of finding butanone trapped in the polymeric structure, which gave the sample a consistency more rubbery. Butanone tended to evaporate from the structure, but the evaporation time was proportional to the mass and dependent on the geometry of the sample. Therefore, it was considered preferable to integrate the solution containing NPs from the beginning, i.e. before

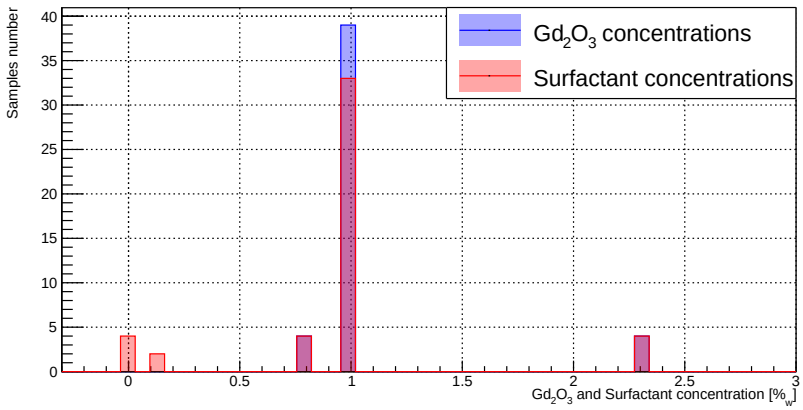

Figure 3.16 – Some laboratory scale samples, depicted according to the concentration of Gd_2O_3 and Igepal used.

the start of heating on the plate. In fact, butanone has a boiling temperature of 80°C, therefore the heating cycle in our polymerization procedure led to the evaporation of a large part of the solvent. Therefore, the final procedure developed for the realization of PMMA samples loaded with gadolinium oxide goes through the following steps:

1. the creation of a colloidal solution composed of gadolinium oxide NPs, Igepal, and 2-butanone (according to our procedure, the butanone used is approximately $1/4$ compared to the volume of MMA)
2. Sonication of the solution for 15 minutes
3. Incorporation of the solution to the monomer previously contacted with alumina to remove the inhibitor
4. Heating the liquid up to 80°C
5. Addition of the first polymerization initiator, the AIBN
6. Vigorous boiling of the solution for several minutes, to consume the AIBN after starting the polymerization reaction
7. Addition of the second initiator of the polymerization reaction after removing the sample from the heating plate
8. Polymerization in a muffle furnace at 55°C for about 24 hours

During the R&D project, several samples were produced (see figure 3.16), with different concentrations of gadolinium oxide and Igepal, different shapes, and different heights (up to 21 cm, see figure 3.17). The reference values reported in

Figure 3.17 – One of the most satisfactory samples produced during the R&D: a 23 cm height sample with a uniform concentration of $1\%_w$ Gd_2O_3.

the DarkSide-20k Technical Design Report [46], require sheets with dimensions of $360\times160\times17$ cm^3, with a gadolinium concentration between $0.5\%_w$ and $1\%_w$ (therefore, as it can be seen, a gadolinium oxide concentration equal to $1\%_w$ was taken as a reference), while as regards the surfactant it was decided to keep it in concentrations as low as possible, in order not to introduce any sources of radiopurity background.
At the end of these steps, there is still some residual butanone inside the solid structure. It is possible to facilitate its removal by extending the residence time in the oven or with subsequent heating cycles of the sample.

Chapter 4

Characterization of the composite material

Due to the novelty of the hybrid material developed for the DarkSide-20k experiment, and because this experiment requires specific characteristics (introduced in section 2.3.2), (such as radiopurity, homogeneity of the gadolinium distribution and resistance to cryogenic temperatures), many characterizations have been carried out. The characterizations have both the purpose of verifying the compliance with the requirements of the DarkSide-20k experiment, and also to investigate the properties that are interesting for the development of the material itself, even though they are not strictly related to the needs of the experiment. In the next sections, I will illustrate some of the results of the characterizations performed on the samples, grouped into some categories:

- Thermal characterizations, i.e. tests aimed at investigating the influence of the NPs on the glass transition temperature, at verifying the homogeneity of our material, and at verifying the material's resistance to cryogenic temperatures
- Viscosimetric properties, not strictly linked to the DarkSide-20k requirements, but that are interesting for the development of this hybrid material
- Mechanical properties, crucial for the purpose of the experiment, aimed, also in this case, to verify the influence of the NPs on the material, comparing them with the standard performances of pure PMMA
- Radiopurity tests, to verify that each component which is used in the realization of the samples does not affect the cleaning of the finished product, in order not to introduce background sources in the DarkSide-20k detector.

Given the large mass of material required for the final production, these characterizations are to be considered only preliminary, and must therefore be compared with the characterizations of the samples produced in the company, which are illustrated in the chapter 6. All the samples used for the following characterizations and their synthesis conditions are reported in table 4.1, in order of appearance in the sections of this chapter. The samples in question

Sample	Gd_2O_3 conc. [$\%_w$]	Igepal conc. [$\%_w$]	Polym. T [°C]	Solvent amount [V/V]	Quench. [y/n]	Incorpor. [bef/af]	Character.
25-05-1	1	1	55	1/3	no	bef	Mass monit.
13-12-1	1	0.01	55	1/4	no	bef	Mass monit.
05-07-1	1	1	55	1	no	bef	Mass monit.
08-03-1	1	1	55	1/2	no	bef	DSC/TGA
24-03-1	1	1	55	1/2	no	bef	DSC/TGA
08-02-4	1	-	55	-	yes	af	TGA
12-02-1	1	1	80	1.2	no	af	TGA
04-03-1	1	10	80	1/2	yes	af	TGA
16-03-1	1	1	60	1/2	no	af	TGA
13-04-2	1	1	55	1/2	no	bef	TGA
09-06-1	1	1	55	1/4	no	bef	Calc.
19-05-2	1	1	55	1/2	no	bef	Calc.
20-05-1	1	1	55	1/3	no	bef	Calc.
13-10-1	2.3	2	55	1/5	no	bef	Calc.
03-11-1	1	0.1	55	1/4	no	bef	Calc.
05-10-1	2.3	2	55	1/4	no	bef	Calc.
29-09-1	1	1	55	1/4	no	bef	Calc.
26-05-1	1	1	55	1/4	no	bef	Calc.
09-12-2	1	0.02	55	1/4	no	bef	Calc.
26-05-2	1	1	55	1/4	no	bef	Calc.
09-12-1	1	0.1	55	1/4	no	bef	Calc.
13-04-3	1	1	55	1/2	no	bef	Cooling
10-02-1	1	1	80	1.2	yes	af	Cooling
12-02-2	1	2	80	1.2	no	af	Cooling
16-06-2	-	-	55	-	-	-	Viscos.
08-06-1	1	1	55	1/3	no	bef	Viscos.
03-06-1	1	1	55	1/3	no	bef	YM

Table 4.1 – Overview of the samples named during the characterizations in the next sections and of the synthesis procedures associated with them. The Gd_2O_3 and Igepal concentration are calculated with respect to the mass of liquid monomer MMA. Sample 08-02-4 was synthesized without surfactant, while sample 16-06-2 is a PMMA with no NPs dispersion. Then the polymerization temperature is reported. The solvent amount is expressed as a volume ratio with respect to MMA. Then some additional details about the polymerization are reported, such as the use of the quenching, and when the incorporation of the NPs occurred: before or after the pre-polymerization. Finally, the characterizations that the samples underwent are reported. "Mass monit." indicates the mass monitoring which has been carried out in order to investigate the solvent residues in the final samples (section 4.1), while calc. stands for calcination. Viscos indicates the viscosimetry measurements and YM indicates the Young Modulus determination through mechanical tractions.

were made both during the refinement of the final procedure, reported in section

3.3.2, (samples 25-05-1, 05-07-1, 08-03-1, 24-03-1, 08-02-4, 12-02-1, 04-03-1, 16-03-1, 13-04-2, 19-05-2, 20-05-1, 13-10-1, 13-04-3, 10-02-1, 12-02-2, and 08-06-1) and after its development (samples 13-12-1, 09-06-2, 03-11-1, 05-10-1, 29-09-1, 26-05-1, 09-12-2, 09-12-1, and 03-06-1).

4.1 Mass monitoring

As mentioned in section 3.3.2, the residual butanone in the polymerized samples naturally tends to evaporate, according to a function that is dependent on the initial butanone mass and on the shape of the container used in the polymerization phase. The presence of solvent in the finite samples can be dangerous, because any bubble caused by the trapped gas can cause defects during the cooling, due to the shrinkage. Therefore, it was decided to study the solvent evaporation in our samples. The evaporation law of butanone is of the exponential type, specifically, according to the equation 4.1.

$$f(x) = c_1 \cdot e^{-\frac{x}{c_2}} + c_3 \tag{4.1}$$

Where c_3 coincides with the final mass of the sample when all the residual butanone has evaporated. A good part of the samples made in the laboratory was monitored over time. Here I will show just a couple of examples of samples with very different masses, made in different containers. The mass values were noted at a certain time in the morning or in the afternoon, and the balance's uncertainty is taken into account in the fit. For convenience, the time elapsed since the end of polymerization is reported on the abscissa axis. In the first case, I illustrate sample 25-05-1 (see table 4.1), with a total initial mass of approximately 115 g (see figure 4.1).

The fit was performed with the CERN ROOT toolkit [79], and the fit parameters are reported in the table 4.2.

Parameter	Value
c_1	$8.221 \pm 5{\cdot}10^{-3}$
c_2	$67.62 \pm 8{\cdot}10^{-2}$
c_3	$105.002 \pm 2{\cdot}10^{-3}$

Table 4.2 – Fit parameters of the plot reported in figure 4.1

In the second case, I illustrate the variation in the mass of sample 13-12-1 (see table 4.1), with a mass approximately 4 times higher, polymerized in a container with different dimensions (see figure 4.2 and the fit results in table 4.3).

As mentioned in section 3.3.2, the butanone can be forced to evaporate through a heating cycle following polymerization. This was done on some

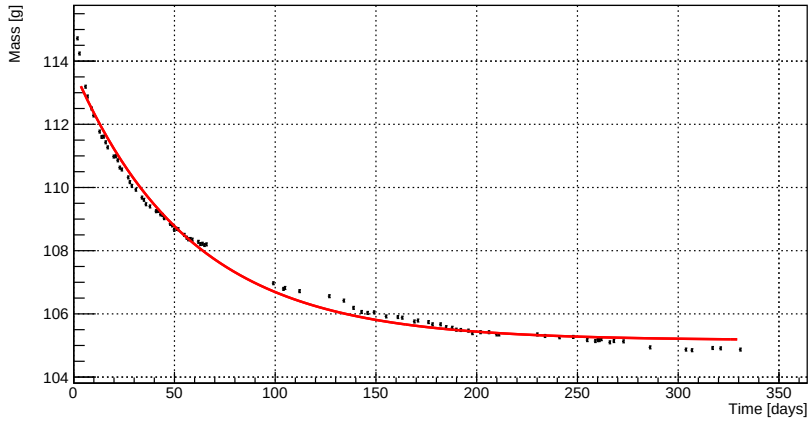

Figure 4.1 – Fit of the mass values of sample 25-05-1, measured with a balance having an accuracy of $\pm$ 0.01 g

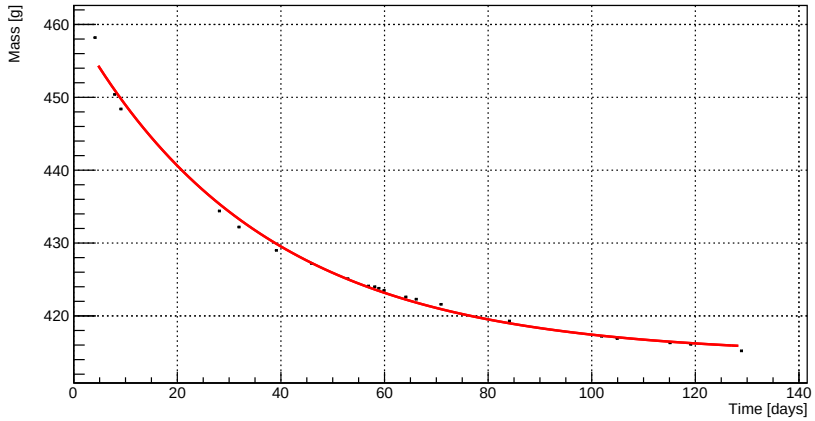

Figure 4.2 – Fit of the mass values of sample 13-12-1, measured with a balance having an accuracy of $\pm$ 0.1 g

Parameter	Value
c_1	$45.2 \pm 1{\cdot}10^{-1}$
c_2	$36.8 \pm 2{\cdot}10^{-1}$
c_3	$414.40 \pm 5{\cdot}10^{-2}$

Table 4.3 – Fit parameters of the plot reported in figure 4.2

samples, including the one shown in figure 4.3 (which is sample 05-07-1, see table 4.1). In the first part of the graph, the usual decreasing exponential trend is observed. The green dashed line shows when the sample was heated. From

that moment on, almost all the butanone is evaporated, therefore the trend of the mass as a function of time is linear, according to equation 4.2.

$$f(x) = c_4 \tag{4.2}$$

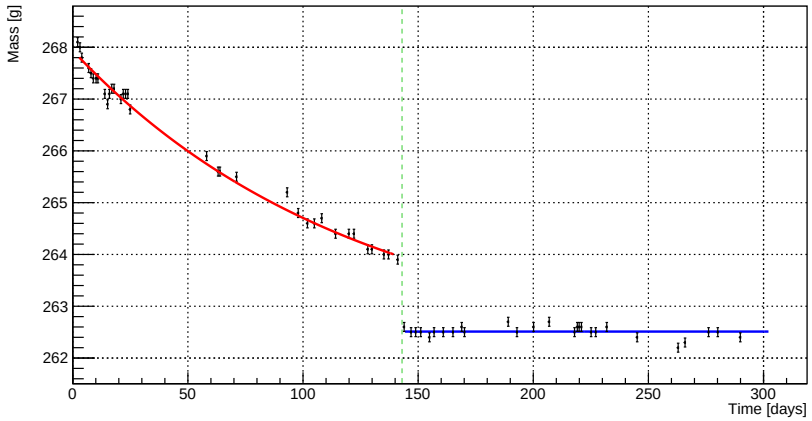

Figure 4.3 – Fit of the mass values of sample 05-07-1, measured with a balance having an accuracy of $\pm$ 0.1 g

Therefore, in the figure, you can see the two types of fit: the red one, is of a decreasing exponential type, while the blue one is linear. The parameters of both fits are shown in table 4.4.

Parameter	Value
c_1	$6.3 \pm 3{\cdot}10^{-1}$
c_2	146 ± 12
c_3	$261.5 \pm 3{\cdot}10^{-1}$
c_4	262.51 ± 0.02

Table 4.4 – Fit parameters of the plot reported in figure 4.3. Parameters c_1, c_2 and c_3 are relative to the red curve, while c_4 is referred to the blue curve.

The difference between c_3 and c_4 is assumed to be due to the systematics. The type of heating to which the sample is subjected is closely related to the mass and geometry of the sample itself.
As already mentioned above, this type of consideration assumes relevance by virtue of the fact that, in the final products (i.e. the PMMA panels loaded with Gd_2O_3 for the DarkSide-20k experiment), the possible presence of trapped gas could have serious consequences in phase cooling. Therefore, it is necessary to have under control the evaporation mechanisms of any solvents. In any case, as will be seen in the 6 chapter, for the industrial samples it was decided to avoid the use of additional solvents, therefore this problem no longer exists.

4.2 Glass transition temperature measurements

Given the nature of this hybrid material, one of the salient points for its characterization is the measurement of the glass transition temperature (T_g). In particular, the possible impact of NPs on T_g was evaluated by comparing samples loaded with Gd_2O_3 with the reference values of the pure PMMA. The T_g of PMMA usually is around 110°C, with fluctuations (of the order of tens of degrees) depending on the molecular weight, the activity, and, therefore, on the polymerization method and on the polymerization initiators used during this procedure [80].

For the purpose of evaluating the homogeneity of the samples, some of them were characterized with the Differential Scanning Calorimetry. DSC is the most suitable technique for measuring T_g, as it measures the response of the polymer to heat fluxes, producing heat difference versus temperature plots as output. The measurement is made by comparing the response of the polymer, contained in a suitable crucible, and using an identical but empty crucible as a reference [81]. The measurements were often repeated in different sections of the same sample. The portions subjected to DSC measurements were taken by carrying out coring of the samples. By construction of the instrument (DSC1 Star^e System by Mettler Toledo [82]), the mass of the portions analyzed was around ten milligrams.

Typically, one of the most standard heating cycles for polymers involves thermal ramps of speeds equal to 10°C/min [83]. Usually, a thermal interval is chosen such as to obtain the T_g approximately at the center of this interval. Knowing therefore the typical reference values for PMMA, a thermal range between -50°C and 250°C was chosen. First, an initial heating of the sample is carried out between room temperature and 250°C, after which the sample is cooled down to -50°C (thanks to a system that uses liquid nitrogen), and finally, it is heated again up to 250°C. The first ramp of heating typically highlights the aging of the polymer, any residual solvent, and the thermal history of the sample. For glass transition measurement, the second heating ramp is considered [84]. In the plots shown in this section, the second heating (i.e. the third and last thermal ramp) is depicted.

First, the uniformity of the properties along the same (08-03-1) sample was evaluated. An example is shown in figure 4.4. The T_g measured on the two portions shows small fluctuations, but they are considered negligible, therefore the measurement confirms the homogeneity of the T_g along the same sample. Despite the imperfect homogeneity of the Gd_2O_3 dispersion (see sections 4.3.1 and 4.3.2), the thermal properties of the composite material do not vary within the same sample. Furthermore, these values are compatible with those of pure PMMA [85]. Therefore these measurements suggest that doping with NPs does not induce changes in the thermal properties of the composite material. The glass transition temperature values are calculated by the instrument's Star^e System

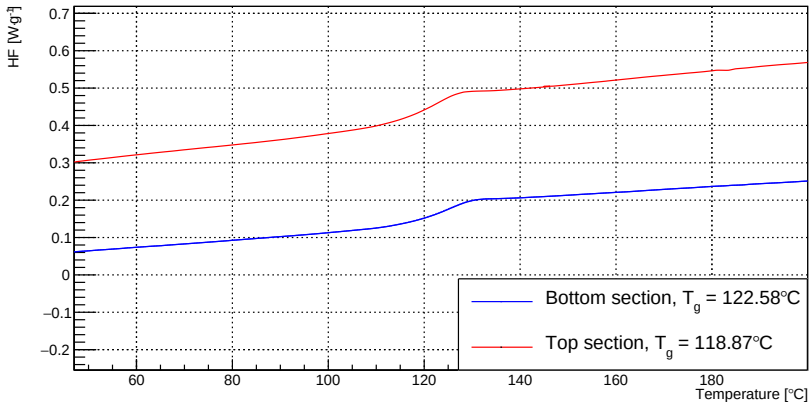

Figure 4.4 – Evaluation of the uniformity of T_g in sample 08-03-1 (see 4.1). The mass of the sample in question is around 100 g and was synthesized according to the final procedure with a NPs concentration equal to $1\%_w$ and surfactant concentration equal to $1\%_w$.

software, which calculates the derivative of the curve in a certain range defined by the user.
After that, the possible variability of T_g between different samples (08-03-1 and 24-03-1) was investigated. An example is shown in figure 4.5. In both cases,

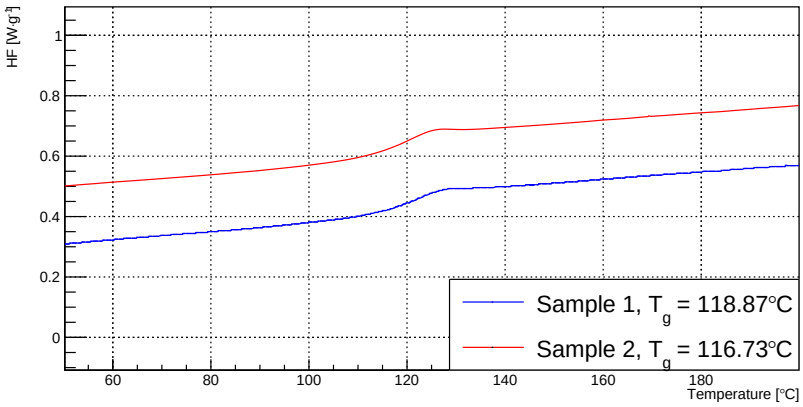

Figure 4.5 – Evaluation of the uniformity of the T_g between two different samples (08-03-1 and 24-03-1, see table 4.1), both produced with the final procedure with a NPs concentration equal to $1\%_w$ and surfactant concentration equal to $1\%_w$, to evaluate the reproducibility.

the T_g is compatible with pure PMMA values. Differences in the order of a few degrees are considered negligible for our purposes and have not been investigated. Therefore, also in this case it can be stated that there are no significant

variations of the T_g introduced by the NPs. The T_g values reported in the figures come from the software supplied with the instrument. Therefore, the accuracy of these values derives only from the sensitivity of the instrument's temperature sensors, but the systematic is not taken into consideration: given the imperfect punctual uniformity in the distribution of Gd_2O_3 between, it was not possible to evaluate the systematicity.

4.3 Gadolinium oxide distribution homogeneity

The homogeneity of the distribution of the Gd_2O_3 inside the polymeric matrix is the most crucial aspect of this work. Particular care was taken in the selection of the technology that could provide us with precise indications of the quality of our composite material. In this sense, two techniques were used: one for less massive samples (which allowed us to acquire a good knowledge of this type of analysis), and a more large-scale one: thermogravimetric analysis and calcination. In both cases, the goal was to characterize different portions of the sample, at different heights, and heat them to remove all inorganic components. By doing so it was therefore possible to trace the mass, and therefore the concentration, of Gd_2O_3. The results of these characterizations are reported in the next sections.

4.3.1 Thermogravimetric analysis

Thermo-Gravimetric Analysis (TGA) is a technique that involves measuring the mass of a polymer while the latter is subjected to a specific thermal cycle. This cycle typically takes place in a controlled atmosphere [86]. The most volatile components (absorbed moisture, residual solvents, additives, or oligomers) usually evaporate by reaching 300°C. As regards the less massive samples, some Thermo-Gravimetric Analysis (TGA) measurements were carried out. This technique was used in a peculiar way: since, as reported in table 3.1, the melting temperature of Gd_2O_3 is 2420°C, by heating the samples up to temperatures of about 800°C it is possible to make sure that all the organic components are decomposed so that only the oxide is obtained. By dividing a sample into several portions along its height, it is possible to obtain information on the concentration of the Gd_2O_3 NPs along the thickness. The instrument used for this analysis is the TGA/DSC1 Star^e System by Mettler Toledo. Each measurement is done by taking core samples of the samples, in a completely identical way to the DSC (see section 4.2), portions of about ten milligrams are then analyzed.
In this case, heating is carried out from a temperature set at 25°C, up to 800°C, the temperature at which all the organic substances have been consumed and the only part of the sample that remains are the NPs. The heating ramp is 10°C/minute, and is carried out in a nitrogen atmosphere up to 600°C, where

the gas is changed into air or O_2, which facilitates the removal of the ashes of the organic substances. Unlike what is usually carried out in these analyzes, it was necessary to focus on the terminal part of the curve of the output plots of the measurement, i.e. in the part at high temperatures, where only the inorganic part of our composite material remains. A typical characterization of a sample is reported in figure 4.6a, where it is possible to see results of sample 12-02-1, carrying 1%$_w$ for both NPs and surfactant. The results of the analyses are reported in table 4.5 In this figure it can be seen that, in the interval between

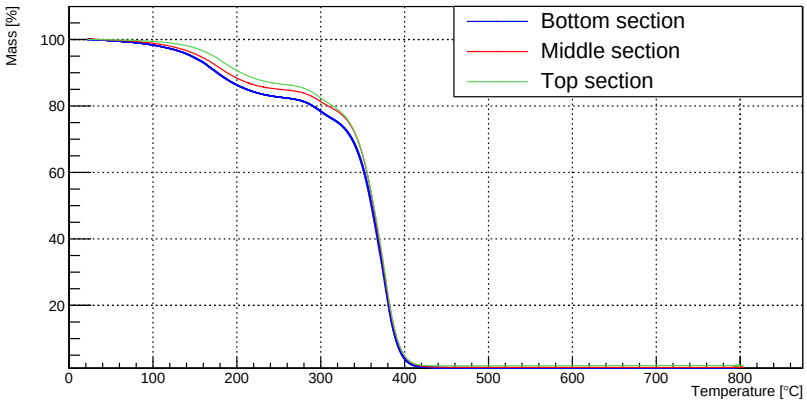

(a) TGA curves of three sections of the same sample.

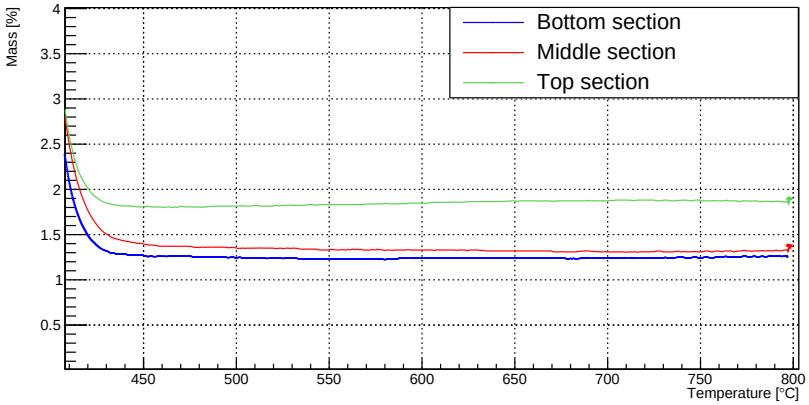

(b) Zoom of 4.6a at high temperatures.

Figure 4.6 – Results of a TGA measurement. The asymptotic value in figure 4.6b is the percentage by mass of Gd_2O_3 relative to that particular section of the sample.

the ambient temperature and 300°C, there are peaks relating to the evaporation of the more volatile organic substances. Then, between 300°C and 400°C, all organic substances are burned. From about 400°C onwards, only the inorganic component remains. At high temperatures (typically around 600°C), there is a

gas switch (from nitrogen to air or O_2), to carry away the organic ashes that are produced following combustion, which would therefore affect the reading of residual values in our measurements. Figure 4.6b shows an enlargement of figure 4.6a for high temperatures, highlighting the residual mass values. Notice how the percent mass values are higher than the nominal ones. This is due to the partial evaporation of the monomer during the preparation of the prepolymer. The values obtained confirm the imperfect homogeneity in the distribution of the NPs, but in any case, the values in each section are compatible with the requirements of the DarkSide-20k experiment. Some of the analyzes carried out are shown in table 4.5 (for the details about the samples' synthesis see 4.1). The

Sample	Section	Nominal Gd_2O_3 concentration [$\%_w$]	Measured Gd_2O_3 concentration [$\%_w$]	Surfactant concentration [$\%_w$]
08-02-4 (raw Gd_2O_3)	Bottom	1	4.33 ± 0.05	-
	Middle	1	0.00 ± 0.05	-
	Top	1	0.05 ± 0.05	-
12-02-1	Bottom	1	1.31 ± 0.05	1
	Middle	1	1.37 ± 0.05	1
	Top	1	1.90 ± 0.05	1
04-03-1	Bottom	1	0.73 ± 0.05	10
	Middle	1	0.36 ± 0.05	10
	Top	1	1.32 ± 0.05	10
08-03-1	Bottom	1	2.43 ± 0.05	1
	Middle	1	1.65 ± 0.05	1
	Top	1	1.89 ± 0.05	1
16-03-1	Bottom	1	0.60 ± 0.05	1
	Middle	1	1.16 ± 0.05	1
	Top	1	1.03 ± 0.05	1
24-03-1	Bottom	1	1.98 ± 0.05	1
	Top	1	1.94 ± 0.05	1
13-04-2	Bottom	1	1.05 ± 0.05	1
	Top	1	1.12 ± 0.05	1

Table 4.5 – Mass residue values obtained from the TGA curves of different samples, produced with different techniques (in particular, the surfactant concentration varied). The values were obtained by taking the last point of each curve.

errors shown in the table refer to the sensitivity of the instrument's balance. The samples reported in this table belong to the refinement phase of the synthesis procedure reported in chapter 3: first of all, the function of the surfactant was verified, in fact sample 08-02-4, produced without the surfactant, was compared with other samples (that were synthesized with the surfactant), and the results show that in sample 08-02-4 a complete sedimentation of the NPs took place, while in other samples (like 12-02-1) a satisfactory uniformity was achieved. Subsequently, the surfactant concentration (sample 04-03-1) was increased by a

factor of 10 to investigate its effect on uniformity. The sample shows a uniformity completely comparable with that shown by the other samples. Further trials, by decreasing the surfactant concentration, are given in section 4.3.2. Samples 08-03-1, 16-03-1, 24-03-1, and 13-04-2 belong to the last phase of refinement of the synthesis procedure, during which parameters such as the polymerization temperature were fine-tuned. The variation of these parameters, as can be seen from table 4.5, does not affect the uniformity of the samples, but only affects the quality of the final product (presence of bubbles and other mechanical defects). Sample 13-04-2 was made with the definitive procedure, reported in section 3.3. Once the synthesis procedure had been established, In any case, once the heating procedure was refined, our interest was more focused on the production of larger sample masses. Therefore the little samples' masses investigated with the TGA were considered too little representative of the sample. Furthermore, these measurements were in fact a rather crude test, since the residual values (fractions of a milligram) were at the limit of the sensitivity of the balance supplied with the instrument. By virtue of these considerations, it was decided to a more representative technique, reported in section 4.3.2.

4.3.2 Calcination

Calcination is a technique that consists in heating a sample to remove all the volatile components [87]. In our specific case, it was decided to use a tubular oven positioned in an inclined position under an extraction hood, to facilitate the release of organic fumes. The samples were therefore no longer taken with coring, but first divided into several sections (according to figure 6.6), and then roughly cut into squares, which were then placed in suitable alumina crucibles, in turn inserted into the tubular furnace (Carbolite, by Tersid s.r.l.).

The furnace was set to 600°C, since it was sufficient for our purposes. Given the impossibility of programming thermal ramps, a manual thermal cycle has been developed as follows:

- First of all, the initial heating from room temperature to 300°C was carried out. The samples were then kept at this temperature for about 15 minutes. At this stage, the sample squares begin to swell and have a spiky consistency.
- After that the samples were brought to 430°C, and again they remained there for 15 minutes. At the end of this temperature stay in the crucible only the oxide and black ashes remain.
- Finally, they were raised to 600°C and again waited for 15 minutes. At this point, the ashes are no longer there, but only the Gd_2O_3 dust remains.
- Since the oven did not have its own cooling system, but simply cooled by leaks, a temperature of 250°C was first set. After a permanence at this

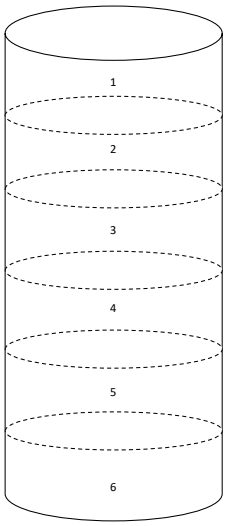

Figure 4.7 – Sectioning of the laboratory samples for the homogeneity characterizations with the calcination technique.

temperature (in order not to introduce excessive stress to the alumina crucibles), the oven was set to room temperature.

With this technique, it was possible to characterize sample portions of approximately 5-10 g at a time. Knowing the initial mass of the portions and weighing the final residue it was then possible to calculate the percentage by mass of Gd_2O_3 in that section of the sample under examination. A large number of samples were analyzed. An overview of these analyzes is shown in table 4.6 (for the details about the synthesis of each sample, see table 4.1).

Sample	Section	Nominal Gd_2O_3 concentration [$\%_w$]	Measured Gd_2O_3 concentration [$\%_w$]	Surfactant concentration [$\%_w$]
09-06-1	Section 1	1	1.491 ± 0.003	1
	Section 2	1	1.185 ± 0.003	1
19-05-2	Section 1	1	1.115 ± 0.001	1
	Section 2	1	0.914 ± 0.004	1
	Section 3	1	1.503 ± 0.003	1
20-05-1	Section 1	1	0.979 ± 0.003	1
	Section 2	1	0.855 ± 0.003	1
	Section 3	1	1.288 ± 0.003	1
13-10-1	Section 1	2.3	2.662 ± 0.003	2
	Section 2	2.3	2.585 ± 0.004	2
	Section 3	2.3	2.624 ± 0.003	2

Table 4.6 continued from previous page

	Section 4	2.3	2.570 ± 0.003	2
	Section 5	2.3	1.453 ± 0.003	2
03-11-1	Section 1	1	1.076 ± 0.003	0.1
	Section 2	1	1.308 ± 0.003	0.1
05-10-1	Section 1	2.3	2.838 ± 0.003	2
	Section 2	2.3	2.544 ± 0.002	2
	Section 3	2.3	2.455 ± 0.003	2
	Section 4	2.3	2.605 ± 0.004	2
29-09-1	Section 1	1	1.296 ± 0.003	1
	Section 2	1	1.208 ± 0.002	1
	Section 3	1	1.041 ± 0.002	1
	Section 4	1	1.290 ± 0.003	1
26-05-1	Section 1	1	1.070 ± 0.003	1
	Section 2	1	0.995 ± 0.002	1
	Section 3	1	1.014 ± 0.003	1
	Section 4	1	1.146 ± 0.002	1
09-12-2	Section 1	1	1.104 ± 0.004	0.02
	Section 2	1	0.999 ± 0.004	0.02
	Section 3	1	1,036 ± 0.004	0.02
	Section 4	1	1.029 ± 0.007	0.02
26-05-2	Section 1	1	1.081 ± 0.002	1
	Section 2	1	1.020 ± 0.004	1
	Section 3	1	0.995 ± 0.003	1
	Section 4	1	1.130 ± 0.004	1
09-12-1	Section 1	1	1.037 ± 0.002	0.1
	Section 2	1	1.132 ± 0.002	0.1
	Section 3	1	1.140 ± 0.002	0.1
	Section 4	1	1.266 ± 0.002	0.1
	Section 5	1	1.230 ± 0.003	0.1
	Section 6	1	1.314 ± 0.002	0.1

Table 4.6 – Some of the calcinations carried out on samples produced in the laboratory. The methodology adopted for the synthesis is the same for all the mentioned samples, but in some cases (like samples 13-10-1, 03-11-1, 13-10-1, and 05-10-1) the concentration of the NPs and of the surfactant varied. This analysis, in fact, was used to evaluate the effectiveness of the synthesis strategy by increasing the concentration of Gd_2O_3 and, subsequently, decreasing the concentration of surfactant (for radiopurity reasons. See chapter 5). Moreover, the stability of the procedure was evaluated on different thicknesses of the samples, to reach dimensions in line with the specifications of DarkSide-20k (section 2.3.2). Sample 09-12-1 represents our best candidate.

The errors reported in the table are obtained starting from the sensitivity of the balance used for weighing. Some of these characterizations were repeated to

test the reproducibility of the method (samples 09-06-1, 19-05-2, and 20-05-1). Then, three other aspects were evaluated:

- the goodness of the synthesis methodology with higher concentrations of NPs and surfactant (samples 13-10-1 and 05-10-1). These samples were prepared with a concentration equal to 2.3%$_w$ of Gd_2O_3 (corresponding to 2%$_w$ of Gd), and 2%$_w$ of surfactant. The homogeneity obtained for these samples shows that the procedure is robust even for samples bearing more than double the concentration of NPs.

- the possibility to scale the thickness of the samples up to the specifications of the DarkSide-20k veto sheets (i.e., 17 cm thick). Therefore, several specimens bearing increasing thicknesses were produced (29-09-1, 26-05-1, 26-05-2), leading to satisfactory results in terms of homogeneity.

- finally, the effect of the reduction in the surfactant concentration on the samples' homogeneity. Samples 03-11-1, 09-12-2 and 09-12-2 were synthesized, respectively, with 0.1%$_w$, 0.02%$_w$, and 0.1%$_w$ of surfactant. This surfactant reduction is due to radiopurity reasons (this aspect is deepened in chapter 5). The results show good homogeneity for all the samples. Sample 09-12-1 is the best candidate: despite the one order of magnitude reduction of surfactant, it has a satisfactory homogeneity for 20 cm of thickness (thus exceeding the requirements of the veto sheets).

Following these analyzes, it was considered that the method developed for mixing and polymerization leads to the creation of samples that are sufficiently homogeneous and therefore satisfactory for the requirements of DarkSide-20k. In conclusion, it is possible to state that the synthesis procedure is satisfactory for the DarkSide-20k experiment homogeneity requirements.

4.4 Annealing and cooling tests

One of the crucial parameters to be tested in our material is its resistance to cold. Therefore, it was considered optimal to retrace the various steps that the final plates will undergo: after polymerization and mechanical processing (which did not occur on all the laboratory samples, but just a few), the plates will undergo an annealing cycle and finally to a cooling cycle in Liquid Nitrogen (LN_2), to simulate the cooling cycle that the final plates will undergo inside DarkSide-20k when it is filled with liquid argon. As for the annealing cycle, it was developed by experts within the DarkSide collaboration, who already had experience with liquid argon-based DM experiments such as DEAP-3600 [88], therefore the annealing is carried out in a suitable oven in this way:

1. First of all, the sample undergoes gentle heating (10°C per hour) from room temperature until it reaches 85°C
2. Afterwards, the sample is maintained at 85°C for 20 hours
3. In the end, a very slow cooling (up to room temperature) is performed (5°C per hour).

All the samples subjected to LN_2 cooling tests were previously annealed.
Several cooling tests in LN_2 were carried out inside suitable cryostats. The objective of these tests was to search for any cracks or other defects induced by the contractions of the material at low temperatures. Furthermore, variations in the mechanical properties of the samples induced by cooling cycles were investigated (see section 4.6). During the cooling tests, the temperature was recorded with Pt100 sensors positioned on the samples and connected to a temperature controller (LakeShore 218). One of the sensors was placed on the bottom of the dewar, two other sensors were placed on the plates on which the samples were glued, and the other sensors were placed on the different samples that were subjected to the cooling cycle (the samples reported in this data taking are: 13-04-3, 10-02-1 and 12-02-2, see table 4.1). For clarity, see figure 4.8 An example of a typical cooling cycle is reported in figure 4.9. During the cooling, particular attention was paid to the thermal gradient to which the samples were subjected (trying to keep it around a few tens of degrees at most).
Once the samples with the relative sensors were positioned inside the dewar, the latter was filled with liquid nitrogen, monitoring the liquid level through the sensors. Once the filling was complete, the dewar was left to slowly heat up until the nitrogen evaporated completely.
Numerous tests were carried out on various samples of different geometries and thicknesses, and none of them showed signs of damage induced by thermal cycles.

4.5 Viscosimetric properties

For the purposes of the characterization of our composite material, it was considered appropriate to evaluate the influence of NPs on the viscosimetric properties. Therefore measurements were carried out using an Ostwald viscometer (illustrated in figure 4.10). A certain amount of polymeric material is taken and dissolved in a suitable organic solvent (2-butanone in our case). Then, the efflux time of this sample is measured through a portion of the capillary of the viscometer, comparing this time with that used by the pure solvent. Then the sample is diluted and the measurement is repeated at various concentrations, for each concentration value 3 or 4 measurement repetitions are carried out, to better estimate the systematic errors. The viscometer, for the whole duration of

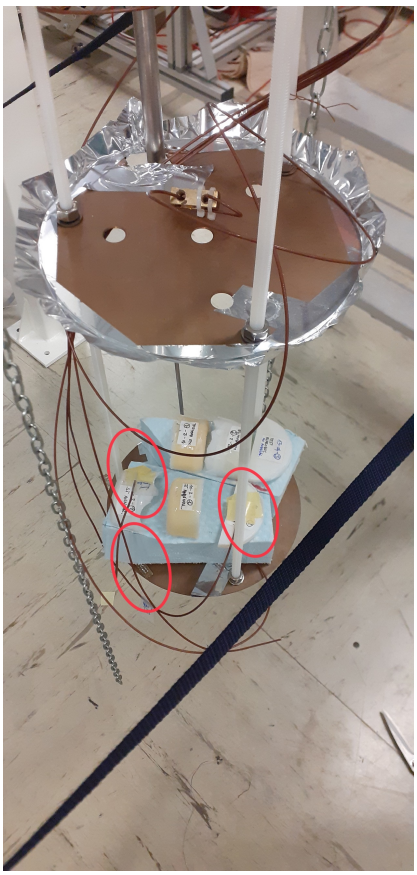

Figure 4.8 – Experimental setup for the cryogenic tests performed on the samples. The blue supports are made of an expanded material that avoids direct contact of the samples with the copper plate, to limit thermal shocks during cooling. The red circles indicate the position of the thermal sensors.

the measurements, is immersed in a thermostated bath kept at a temperature of 25°C [89]. Once the efflux times have been obtained for some concentration value, intrinsic viscosity values can be calculated [90]. First, the specific viscosity values are obtained, through the equation 4.3:

$$\eta_{sp} = \frac{t - t_0}{t_0} \tag{4.3}$$

Where t_0 is the travel time of the pure solvent along the viscosimeter section, and t is the travel time of the solution. Starting from the specific viscosity it is possible to calculate the reduced viscosity, through the equation 4.4:

$$\eta_{red} = \frac{t - t_0}{t_0 c} = \frac{\eta_{sp}}{c} \tag{4.4}$$

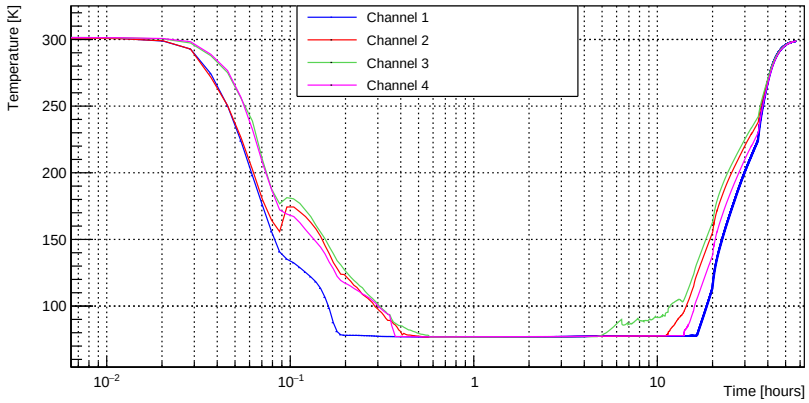

Figure 4.9 – Cooling cycle of some laboratory-scale samples. The time scale shown on the abscissa refers to the time elapsed since the start of cooling.

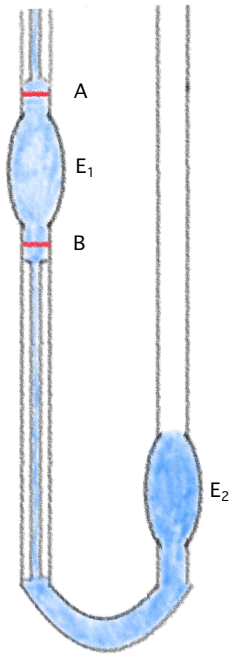

Figure 4.10 – Schematic of an Ostwald viscometer. The sample is entered in the right column, and settles into the enlargement E_2. The liquid is brought to the top of the left column with a Peleus ball, then it is expected to flow to point A (above the enlargement E_1): at that moment a timing is started, which ends when the liquid reaches the point B.

Where c is the concentration of the solution. At last, it is possible to graph the specific viscosity values as a function of the concentration, thus obtaining a

straight line. By making a fit of this line, it is possible to obtain the intercept values, i.e. intrinsic viscosity $[\eta]$, according to the equation 4.5:

$$\lim_{c \to 0} \eta_{red} = [\eta] \tag{4.5}$$

In the first place, therefore, the effect of NPs on the composite material was evaluated by comparing the values obtained by characterizing a sample of pure PMMA with one loaded with Gd_2O_3. The results are shown in figure 4.11. The

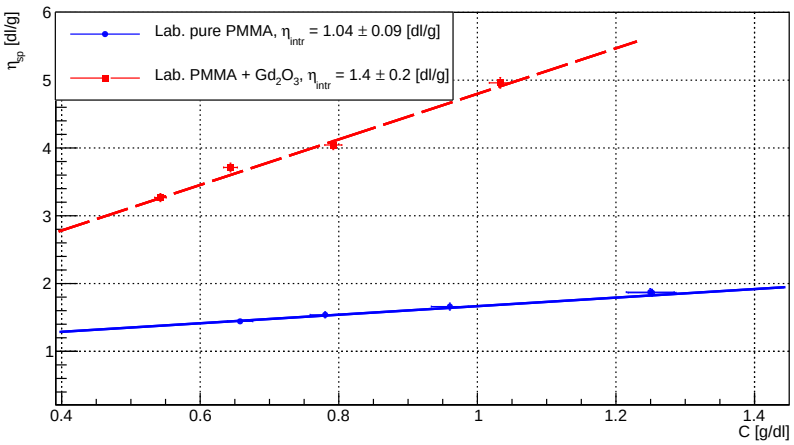

Figure 4.11 – Specific viscosity values for a sample of raw PMMA (16-06-2) and one of PMMA additivated with Gd_2O_3 (08-06-1, see table 4.6).

fits (red lines) shown in the figure were carried out according to equation 4.6, and the intercept values shown in the legend have been obtained from these fits.

$$f(x) = a \cdot x + M_\nu \tag{4.6}$$

Where M_ν is the mean molecular mass of the polymer. From a first quick test, the variations induced by the NPs are compatible with the error associated with the measurement. Not being a critical parameter for the DarkSide-20k experiment, these properties have not been further investigated. The intrinsic viscosity is related to the mean molecular mass M_ν according to the Mark-Houwink-Sakurada law, reported in equation 4.7.

$$[\eta] = K \cdot M_\nu \tag{4.7}$$

Where K and a are strictly dependent on the solvent used and the temperature. In the case of butanone and at a temperature equal to 25°C, K and a equal respectively to $6.8 \cdot 10^3$ ml/g and 0.72 (a being dimensionless) [91]. Therefore, the latter quantity was calculated both for our PMMA and for the pure PMMAs

of two partner companies selected for the final production of the plates for the veto of DarkSide-20k. The mean molecular mass values are shown in table 4.7.

PMMA	M_ν
Our sample	$(6 \pm 1)\cdot 10^5$
Clax s.r.l.	$(9 \pm 1)\cdot 10^5$
DonChamp	$(9 \pm 3)\cdot 10^5$

Table 4.7 – Mean molecular mass measurements on different PMMA samples.

4.6 Mechanical properties

Given the hybrid nature of the material developed in this work and since it is an innovative material, it was considered appropriate to test its mechanical properties to verify that the NPs had a significant influence on these, since large variations from the typical mechanical properties typical of PMMA could be a problem for the DarkSide experiment, given the large mass involved and the function of the material as a structural part of the TPC.
The properties that were investigated during this work are Young's modulus, the ultimate tensile strength, and the coefficient of thermal contraction. The first two properties were investigated through tensile tests, while the last was investigated with shrinkage tests. The tests mentioned are reported in the next sections.

4.6.1 Tensile tests

The samples were characterized with an Instron polymeric sample puller. From the samples produced in the laboratory, specimens with a thickness of about 1 mm and a length of 6 cm were obtained. The samples were then constrained by two clamps at the ends and, finally, pulled, with a programmed speed of 0.06 mm/s. Starting from the output data, the stress-strain curves were then studied to derive Young's modulus and the ultimate tensile strength. A typical stress-strain curve is shown in figure 4.12, which was obtained by the characterization of sample 03-06-1 (see table 4.1). The curve in question was obtained from a laboratory sample with a surfactant concentration equal to $1\%_w$ and a surfactant concentration equal to $0.1\%_w$. It is emphasized that, although the laboratory samples are not representative of the final production methodology (reported in section 6.1), they have been characterized in the course of the R&D work, to investigate the influence of NPs on the properties of the composite material. The characterizations of the most representative samples, (i.e. the ones produced on an industrial scale and with the surfactant concentration of the final mixing recipe), are reported in section 6.2.4. In any case, the value of Young's modulus

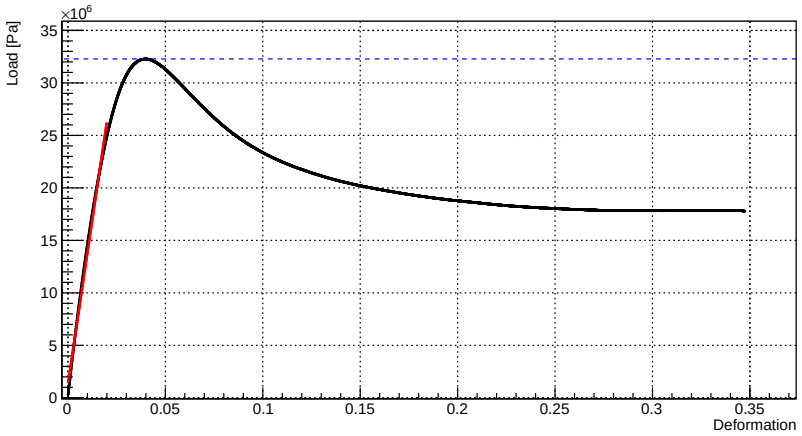

Figure 4.12 – Stress-strain curve obtained for a laboratory sample showing a concentration of Gd_2O_3 equal to $1\%_w$ and a concentration of surfactant equal to $0.1\%_w$. The red line was used to fit the curve in its linear region for the calculation of Young's modulus, while the blue dashed line refers to the ultimate tensile strength of the sample.

was obtained by fitting the curve in its linear range with the ROOT software by CERN. The Young's modulus and ultimate tensile strength of the sample shown in figure 4.12 are shown in table 4.8. These results are compatible with the

Property	Value
Young modulus	(1.3± 0.1) GPa
Ultimate tensile strength	(32.28 ± 0.04) MPa

Table 4.8 – Mechanical properties of a laboratory-scale sample.

typical values of the pure PMMA [92]. Therefore, since the laboratory scale samples exhibit mechanical properties in line with DarkSide-20k requirements, our procedure is suitable for transfer to an industry capable of final production of the veto walls.

Chapter 5

Development of a mitigation strategy for the ^{40}K contamination in the surfactant

In this chapter, I will illustrate the problems related to contamination by radioactive isotopes encountered during my thesis work, and the strategies to mitigate the contamination. All the radiopurity measurements reported were performed by experts of the collaboration or, in some cases, by specialized technicians of the Chemistry Department of the University of Genoa. For rare events physics, small contaminations by some isotopes may be sufficient for a material to be deemed unsuitable. As mentioned in section 2.3.1, some of the most dangerous isotopes for these applications are ^{238}U, ^{232}Th, and ^{40}K. Typically, the contaminations are expressed in the form of the specific activity of the isotope in question, defined according to equation 5.1.

$$a_{sp} = \lambda \cdot N = \frac{N_a \cdot \ln(2)}{T_{\frac{1}{2}} \cdot M} \tag{5.1}$$

Where N is the number of atoms, λ is the decay constant, N_a is the Avogadro number, $T_{1/2}$ is the half-life of the isotope and M is the molar mass. Specific activity a_{sp} is expressed in Bq/kg (or, more typically, mBq/kg).
One way to evaluate the a_{sp} of some dangerous isotopes is to perform screenings with a High Purity germanium (HP-Ge) detector, which is a semiconductor diode which detects traces of unstable isotopes thanks to γ-ray spectroscopy: the γs emitted during the decay chains interact with the Ge semiconductor,

with consequent generation of electron-hole pairs, which are then measured. The number of generated electron-hole pairs is proportional to the energy of the deposited γ. Due to its high atomic number, Ge is the best choice for γ spectroscopy [93].
Due to its energetic resolution, a HP-Ge detector is sensitive to specific parts of the decay chains of the isotopes. For example, it is susceptible to the middle part of the decay chains of ^{238}U and ^{232}Th. Therefore, referring to figure 2.9 and figure 2.10, the ^{226}Ra-^{214}Po part. Moreover, it is very sensitive to the γs emitted during ^{40}K decay [94]. To understand if the specific activity values comply with the DarkSide-20k requirements, we look at the decay and the number of particles produced for each isotope. The output of a HP-Ge measurement is expressed in terms of the specific activity. The conversion factors from the specific activity to a concentration unity strictly depend on the isotope's characteristics. In order to calculate them, one has to apply equation 5.1, but calculating N (number of atoms) considering the abundance of the isotopic species in question. Therefore, these conversion factors for ^{238}U, ^{232}Th and ^{40}K are shown in table 5.1 [95].
The choice of starting materials for the realization of our composite was based

Isotope	Conversion
^{238}U	1 Bq/kg = 81 ppb U
^{232}Th	1 Bq/kg = 246 ppb Th
^{40}K	1 Bq/kg = 32.3 ppm K

Table 5.1 – Conversion factors for ^{238}U, ^{232}Th and ^{40}K.

on the radiopurity requirements. Gadolinium oxide, among the gadolinium-containing compounds, can be produced with a degree of radiopurity compatible with the requirements of the DarkSide-20k experiment.
First, vendors of gadolinium oxide were selected, and some samples of their products were screened for radiopurity with a HP-Ge detector. In the end, the Japanese company ShinEtsu was found to be the manufacturer most compliant with radiopurity requirements (see table 5.2 [46]).

The corresponding concentration values for the U, Th, and K elements are reported in table 5.3. As it can be noticed, just minor contaminations are sufficient to produce a high activity, especially if we consider having to multiply the values of specific activity by the total mass of Gd_2O_3 in the veto, which is 112 kg. For what concerns these samples of gadolinium oxide, the rate of events produced by the interaction of particles must remain low enough to maintain the background level at a level of about $1/3 \cdot 10^{-1}$ neutrons events/200 t·year. As illustrated above (see section 2.3.1), some of the most abundant isotopes for this type of experiment are the decay chains of ^{238}U and ^{232}Th (which can emit neutrons by reactions (α, n) and the isotope ^{40}K, which emits β-particles (as anticipated in section 2.3.1). The results shown in the table, given the specific

Isotope	ShinEtsu sample 1 activity [mBq/kg]	ShinEtsu sample 2 activity [mBq/kg]	ShinEtsu sample 3 activity [mBq/kg]
^{238}U-^{234m}Pa	$<1.2{\cdot}10^{3}$	<637	<99
^{238}U-^{226}Ra	13.6±3.0	6.6±1.8	2.68±0.47
^{232}Th-^{228}Ac	<30	<24	<6.0
^{232}Th-^{228}Th	<27	<19	2.31± 0.68
^{235}U-^{235}U	<51	<25	<1.5
^{235}U-^{227}Ac	<82	<57	<6.5
^{40}K	<37	<23	<13
^{60}Co	<2.5	<1.3	<0.62
^{137}Cs	<4.0	<2.2	<0.70
^{138}La	<3.2	<2.0	<0.71
^{176}Lu	12.9± 2.6	12.1 ±2.1	2.33 ±0.35

Table 5.2 – Assay results of raw Gd_2O_3 samples, performed by DarkSide collaborators with a Germanium detector.

Sample	U		Th		K	
	^{238}U a_{sp} [mBq/kg]	U conc. [ppb]	^{232}Th a_{sp} [mBq/kg]	Th conc. [ppb]	^{40}K a_{sp} [mBq/kg]	K conc. [ppm]
Shin-Etsu 1	13.6 ± 3.0	1.10 ± 0.24	<27	<7	<37	<1.2
Shin-Etsu 2	6.6 ± 1.8	0.53 ± 0.15	<19	<5	<23	<0.7
Shin-Etsu 3	2.68 ± 0.47	0.22 ± 0.04	2.31 ± 0.68	0.6 ± 0.2	<13	<0.4

Table 5.3 – U, Th and K contamination levels from table 5.2. For every specific activity value, the corresponding concentration of the element is reported, using the conversion factors reported in table 5.1.

activity values obtained, were deemed satisfactory for our requirements.

Due to the stringent constraints on radiopurity, as already mentioned in the previous section, it is necessary to subject each component introduced into the DarkSide-20k experiment to strict radiopurity screening. These screenings were also carried out on the surfactant used in the mixing procedure of Gd_2O_3. First of all, a screening was performed using the Inductively Coupled Plasma Mass Spectrometer (ICP-MS) technique (table 5.4). The sample is acceptable as

Element	Concentration [ppb]	Specific activity [mBq/kg]
Th	< 0.01	<0.041
U	< 0.01	<0.12

Table 5.4 – U and Th determination via Inductively Coupled Plasma Mass Spectrometer (ICP-MS) measurement on a Igepal sample. The specific activity values were obtained using the conversion factors reported in table 5.1

regards U and Th contamination. Afterward, another screening was performed

using a HP-Ge detector, following which a very activity high due to the ^{40}K isotope was found (see table 5.5). This activity is probably due to the use of potassium salts in the industrial synthesis of Igepal, the procedure of which, however, is not disclosed to the public. The ^{40}K isotope decays according to the

Isotope	Specific activity HP-Ge [mBq/kg]
^{235}U	<51
^{238}U-^{234m}Pa	$<4.8{\cdot}10^{3}$
^{238}U-^{214}Pb	<55
^{238}U-^{214}Bi	<55
^{232}Th-^{228}Ac	<105
^{232}Th-^{212}Pb	<43
^{232}Th-^{208}Tl	<60
^{40}K	$(31.9{\pm}3.2){\cdot}10^{3}$
^{137}Cs	<28
^{60}Co	<23

Table 5.5 – HP-Ge measurement performed on an Igepal CO-520® batch performed at the facilities of Laboratori Nazionali del Gran Sasso. When no decays associated with a specific isotope are seen during the screening, an upper limit is set, which is related to the sensitivity of the detector to that particular isotope.

scheme illustrated in figure 5.1 [94], [96].

Note that among the decay mechanisms, there is one with the emission of γ rays,

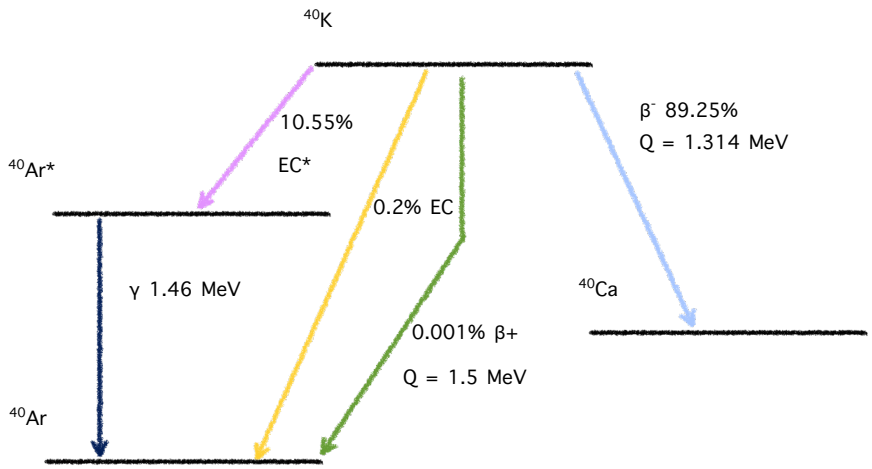

Figure 5.1 – Decay mechanisms of the ^{40}K isotope, with their probability. The Q values refer to the endpoint energy of the corresponding process.

which therefore would affect the performances of the experiment (see section

2.3.1). The rate of γ in the DarkSide-20k detector is calculated by the Materials working group screening results, so taking into account all the contributions coming from the isotopes detected during the screening. In the event that the report for a given isotope reports an upper limit, that limit is taken as a reference value for the calculation of the γ rate.
Given the screening results of the surfactant, the ^{40}K activity was considered unacceptable for the radiopurity requirements of the experiment. Therefore, in order to minimize the γ rate, the following strategies were explored, in parallel:

- The reduction in the surfactant concentration in our mixing and polymerization procedure
- The purification of the surfactant from the K, by removing most of it before the starting of the mixing and polymerization procedure.

5.1 Surfactant reduction

During the R&D work, it was decided to explore the possibility to use a reduced concentration of surfactant in our procedure, that is, compared to the original procedure (which used an Igepal concentration equal to $1\%_w$ with respect to the mass of PMMA, i.e. the same concentration as Gd_2O_3), the surfactant concentration was reduced to $0.1\%_w$ with respect to the mass of the PMMA. The obtained samples had a homogeneity compatible with the one with $1\%_w$ surfactant concentrations: an example is reported in table 5.6 (whose values are taken from table 4.6 in section 4.3.2). From these results, it is possible to state

Sample	Nominal Gd_2O_3 NPs concentration [$\%_w$]	Igepal concentration [$\%_w$]	Sample thickness [cm]	Measured Gd_2O_3 concentration [$\%_w$]
09-12-1	1	0.1	21	1.037 ± 0.002 1.132 ± 0.002 1.140 ± 0.002 1.266 ± 0.002 1.230 ± 0.003 1.314 ± 0.002

Table 5.6 – Gd_2O_3 distribution homogeneity in a sample carrying a reduced Igepal concentration.

that the mixing and polymerization procedure can be brought to fruition also with a reduced surfactant concentration.

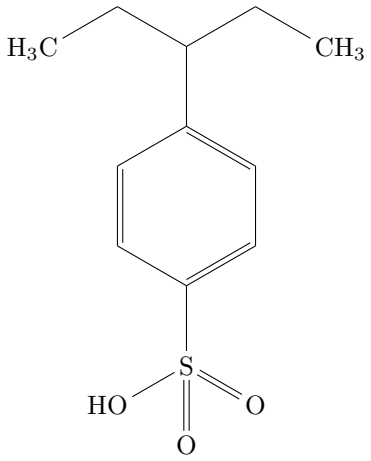

Figure 5.2 – Structure formula of Dowex 50WX8 resin.

5.2 Surfactant purification

Additionally, it was decided to develop an Igepal purification procedure, suitable for the removal of most of the potassium. The procedure developed involves putting the Igepal in contact with a suitable ion exchange resin, which in fact exchanges potassium ions with hydrogen ions, purifying the Igepal from potassium. The resin selected is AmberChrom® 50WX2, whose composition is not disclosed to the public, but its structure is similar to the molecule reported in structure formula 5.2 [97]. The resin works by exchanging cations in non-ionic surfactants such as in the case of our Igepal. The reaction scheme is illustrated in equation 5.2 [98].

$$M^+ + X^- + N + [RSO_3^- H^+] \rightleftharpoons H^+ + X^- + N + [RSO_3^- M^+] \tag{5.2}$$

Where M^+ is the surfactant cation, X^- is the surfactant anion, the group $[RSO_3^- H^+]$ represents the cation exchange resin and N is the non-ionic agent. The resin comes in the form of brownish spheres with a moist consistency.
The procedure investigated for the removal of the potassium is the following:

- First of all, a quantity of resin equal to 5%$_w$ or 10%$_w$ is taken with respect to the quantity of surfactant to be purified.
- The resin is first washed with ethanol in three different steps. This step, necessary to remove some impurities from the resin, could, however, affect its properties.
- Therefore, the resin is then reactivated using 3M HCl.
- Consequently, it is re-washed with deionized water.

- Then, it is placed in contact with the surfactant and the contact is maximized through magnetic stirring for a variable time.
- Finally, after the stirring, the surfactant and the resin are separated through a centrifuge process or with a filtering process through a Büchner filter.

Several samples were then produced, following slightly different procedures and varying the contact time of the resin with the surfactant. Table 5.7 provides an overview of the samples produced and the different procedures they underwent.

Sample	Igepal content [ml]	Resin content [$\%_w$]	Contact time	Filtration	Notes
Sample 2	20	5	10 min	Büchner filter	No washing. Left to filter for a weekend
Sample 3	20	5	20 min	Büchner filter	No washing. Left to filter for a weekend
Sample 4	20	5	40 min	Büchner filter	No washing. Left to filter for a weekend
Sample 5	20	10	20 min	Büchner filter	No washing. Left to filter for a weekend
Sample 6	20	5	20 min	Büchner filter	Washed. Left to filter for a weekend
Sample 7	50	5	20 min	Büchner filter	Washed. Filtration carried out with the aid of a water pump
Sample 9	20	10	20 min	Büchner filter	No washing. Left to filter for a weekend
Sample 10	20	10	20 min	Büchner filter	Washed. Left to filter for a weekend
Sample 11	20	15	20 min	Büchner filter	Washed. Left to filter for a weekend

Table 5.7 continued from previous page

Sample 12	20	10	20 min	Centrifuge	Washed. Before stirring, resin let dry overnight
Sample 13	20	10	20 min	Centrifuge	Washed.
Sample 14	20	10	30 min	Centrifuge	Washed. Before stirring, resin let dry for 20 min
Sample 15	20	10	2 h	Centrifuge	Washed. Before stirring, resin let dry for 20 min
Sample 16	20	10	22 h 30 min	Centrifuge	Washed. Before stirring, resin let dry for 20 min
Sample 17	20	10	3 days	Centrifuge	Washed. Before stirring, resin let dry for 1 h.
Sample 18	20	10	1 week	Centrifuge	Washed. Before stirring, resin let dry for 15 min.
Sample 19	100	10	1 week	Centrifuge	Washed. Before stirring, resin let dry for 15 min.

Table 5.7 – Igepal samples produced during the development of the filtration technique. Also, some raw Igepal samples were realized, in order to evaluate the degree of contamination in the Igepal lots. The washing procedure named in the last column is referred to as the first treatment with ethanol. The centrifugation parameters are strictly dependent on the amount of surfactant and resin to separate.

These samples were then characterized by Inductively Coupled Plasma Atomic Emission Spectroscopy (ICP-AES), which provides information about the concentration of the element to be identified (therefore, the overall potassium concentration, including all the isotopes present), at the laboratories of the Chemistry Department of the University of Genoa. Furthermore, some samples were characterized with the collaboration facilities, at the Laboratori Nazionali

del Gran Sasso (LNGS) and the Laboratorio Subterráneo de Canfranc (LSC). As for the LNGS measurements, an ICP-MS was used. The output of these measurements is a potassium concentration. As can be seen, with the purification method

Sample:	K conc. ICP-AES Genova [mg/kg]	K conc. ICP-MS LNGS [mg/kg]	^{40}K activity ICP-AES Genova [mBq/kg]	^{40}K activity ICP-MS LNGS [mBq/kg]
1	605±29	575±30	$(1.87\pm0.09)\cdot10^4$	$(1.78\pm0.09)\cdot10^4$
2	155±14	-	$(4.8\pm0.4)\cdot10^3$	-
3	205±15	-	$(6.4\pm0.5)\cdot10^3$	-
4	150±13	-	$(4.6\pm0.4)\cdot10^3$	-
5	80±6	85±5	$(2.5\pm2)\cdot10^3$	$(2.6\pm0.2)\cdot10^3$
6	335±21	-	$(1.04\pm0.07)\cdot10^4$	-
7	495±28	-	$(1.53\pm0.09)\cdot10^4$	-
8	-	610±31	-	$(1.9\pm0.1)\cdot10^4$
9	168±1	165±8	$(5.20\pm0.03)\cdot10^3$	$(5.1\pm0.3)\cdot10^3$
12	590±6	-	$(1.83\pm0.02)\cdot10^4$	-
13	188±1	-	$(5.82\pm0.03)\cdot10^3$	-
14	-	325±16	-	$(1.01\pm0.05)\cdot10^4$
15	-	210±11	-	$(6.5\pm0.3)\cdot10^3$
16	-	280±14	-	$(8.7\pm0.4)\cdot10^3$
17	10±2	-	$(3.2\pm0.6)\cdot10^2$	-
18	4±1	-	$(1.3\pm0.3)\cdot10^2$	-

Table 5.8 – Spectroscopical measurements performed on raw Igepal and on purified samples. The table shows both analyses performed at the Chemistry department in Genova and at LNGS by the Materials working group of the DarkSide collaboration. In the fourth and fifth columns are reported the corresponding values of specific activity due to the ^{40}K isotope, obtained through conversions. Sample 1 and sample 8 are raw Igepal coming from different batches, in order to estimate the variation of K amount in different lots.

developed, thanks to this strategy, it was possible to reduce the potassium concentration by roughly two orders of magnitude. A final screening, conducted with a HP-Ge detector on sample 19, is reported in table 5.9.

The aim of the purification strategy was to reduce as much as possible the K content, in order to minimize its contribution to the γ rate inside the detector. Starting from the values reported in table 5.8, it is possible to calculate the γ rate respectively in the veto and in the TPC of the DarkSide-20k experiment. Table 5.10 shows different scenarios (with different potassium concentrations in the surfactant) in terms of γ rate. The values were kindly provided by a collaborator of the DarkSide-20k material working group. The table is built starting from two reports of the DarkSide material working group: the first, shown in table 5.5, relates to the raw Igepal. In the second case, the very same radioactivity values were taken into account, but the mass of the surfactant was reduced by an order

Isotope	Specific activity [mBq/kg]
^{235}U	<9.4
^{238}U-^{234m}Pa	$<1.5 \cdot 10^3$
^{238}U-^{226}Ra	<19
^{232}Th-^{228}Ac	<43
^{232}Th-^{228}Th	<12
^{40}K	129 ± 24
^{137}Cs	<4.4
^{60}Co	<3.3

Table 5.9 – HP-Ge measurements performed on a purified Igepal CO-520 HP-Ge measurements done on the purified Igepal CO-520® sample 19 performed at the facilities of Laboratorio Subterráneo de Canfranc.

	Contribution to γ bkg [Hz]					
	Igepal not purified $1\%_w$		Igepal not purified $0.1\%_w$		Igepal purified $0.1\%_w$	
Contributor	TPC	Veto	TPC	Veto	TPC	Veto
Gd_2O_3	0.4	0.9	0.4	0.9	0.4	0.9
Igepal	104	200	10.4	20	0.5	1.4
PMMA	9.7	19.5	9.7	19.5	9.7	19.5
Total contribution from Gd-PMMA	114.1	220.4	20.5	40.4	10.6	21.8

Table 5.10 – Different gamma background scenarios induced by the effect of the Igepal. In this table are listed only the contributors related to our hybrid material. In the first case, the raw Igepal is considered, in a concentration equal to the one of Gd_2O_3, that is $1\%_w$ with respect to the PMMA. The second scenario foresees the raw Igepal in a concentration of an order of magnitude less than in the previous case. The last case represents the cleanest scenario: a concentration of $0.1\%_w$ of purified surfactant.

of magnitude. In the last case, the values reported in table 5.9 were used, still with the reduced surfactant mass.

For what concerns the U and Th activity in the first two case scenarios, the values obtained with the ICP-MS were taken as a reference, since they set a more stringent limit. These values correspond to what is reported in the last column of table 5.5.

As it can be seen, the developed procedure is capable of strongly reducing the γ rate both in the veto and in the TPC, bringing us into a situation in which the γ background is dominated by PMMA (whose radioactivity levels are in any case adequate to the requirements of the experiment) and no longer by surfactant.

Chapter 6

Industrial production

For the production of the components that constitute the veto (and the walls of the TPC) for the DarkSide-20k experiment, it is necessary to contact a company specialized in the production of large masses of polymeric material. The company must be equipped with all the infrastructures suitable for handling slabs of large volume and mass, it must also operate in an environment that is as clean as possible (from the radioactivity and chemical point of view), to avoid contamination of materials, and must have machinery capable of working the pieces at very high precision, reaching sub-millimetric mechanical tolerances. Moreover, the starting materials must be radiopure enough for our purposes.
The gadolinium-loaded PMMA components that must be produced for the experiment are eight side walls (which make up the veto/TPC walls) and a series of bricks that make up the endcaps. The walls have dimensions equal to 360x160x17 cm^3, afterward they will be subjected to machining and will reach the final thickness of 15 cm. A scheme of these walls is illustrated in figure 6.1a. On the other hand, the dimensions of the bricks vary according to their position

(a) Gd-PMMA barrel wall scheme. The Gd-PMMA part is drawn in green, while the part with blue lines represents the field cage (see section 1.4).

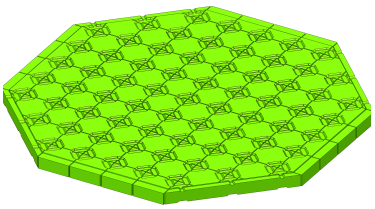

(b) Scheme of the Gd-PMMA endcap and of the bricks that make it up.

Figure 6.1 – Schematic of the main parts of the DarkSide-20k veto.

on the endcap (see figure 6.1b). Roughly, it can be stated that about 11 tons of material must be produced.

6.1 Industrial scale procedure

Given the novelty of this hybrid material, for the final production of the veto slabs it was necessary to collaborate with an industry specialized in the production of large slabs of PMMA, which was willing to modify a production line to make the material according to our procedure.
For the two different R&D projects (i.e. based on Gd_2O_3 NPs and $Gd(MAA)_3$), two partner industries were selected: the Chinese industry DonChamp [99] (which already has experience in building materials with high radiopurity standards, since it was the company that built the vessel for the JUNO experiment [100]) and the Italian industry Clax s.r.l. [101].
To adapt to industrial production, our procedure has undergone some changes. Since October 2021, eight samples have been produced, following different approaches. The most delicate aspect is to produce 17 cm thick PMMA plates, with dimensions roughly 160×360 cm^2, maintaining a homogeneous distribution of gadolinium oxide. As a first step 4 cm thick sheets were produced, but the samples showed non-uniformity in the Gd_2O_3 distribution. Consequently, both the mixing and the polymerization procedure were modified, to drastically increase the viscosity in the early stages of the process.
The final procedure involves a first phase of mixing when the Gd_2O_3 and the Igepal are incorporated in a small quantity of MMA and subjected to mechanical agitation. Then the mixture is added to the final amount of MMA and the pre-polymerization stage is performed in a dedicated reactor (heated container with a mechanical stirrer). Finally, the high-viscosity syrup is injected into a glass mold which is kept under high pressure during the polymerization in the autoclave. These are the key steps of our industrial production, but in the industrial tests several parameters were tuned to find the optimal mixing strategy for our purposes. Note that the use of butanone as solvent is no longer needed, further simplifying the procedure. The key quantities can be found in table 6.1, where the produced samples are schematized.

During the refining of the industrial process, different approaches were exploited, as follows:

- Clax 1-1: A sample produced following exactly our laboratory procedure. A solution with Gd_2O_3 and Igepal in 2-butanone was sent to the industry, where it was added to liquid MMA. The pre-polymer was kept at a

Sample name	Surface [cm^2]	Thick. [cm]	Gd_2O_3 [$\%_w$]	Igepal [$\%_w$]	T [°C]	P [bar]	Solv. [y/n]	Visc. [cP]
Clax 1-1	40x40	4	1	1	Std	Std	yes	400
Clax 1-2	40x40	4	1	1	Std	Std	yes	400
Clax 1-3	40x40	4	1	1	Std	Std	no	400
Clax 2-1	50x50	12	1	0.1	≈50	10	no	1000
Clax 2-2	50x50	12	1	0.1	≈50	10	no	1000
Clax 2-3	50x50	12	1	0.1	≈50	10	no	1000
Clax 2-4	50x50	12	0.80	0.1	≈50	10	no	400
Clax 2-5	50x50	12	0.85	0.1	≈50	10	no	400

Table 6.1 – An overview of the samples produced at Clax Italia s.r.l. For what concerns viscosity, the standard value is around 400 Centipoise, while the enhanced values for temperature and pressure correspond to, respectively, 50-52°C and 10 bar.

standard level of viscosity (400 Centipoise). The polymerization was then performed using our initiators (AIBN and Luperox), with standard values for temperature and pressure. The mixture was filtered in order to remove any contaminants such as dust. The polymerization time was around 80 hours.

- Clax 1-2: A sample produced starting from a solution identical to the one used in the previous point (Gd_2O_3 and Igepal in Butanone). The solution was then incorporated in MMA and polymerization was induced using the initiator normally used in the company, with standard values for temperature, pressure, and viscosity of the pre-polymer. The polymerization time was around 80 hours. Also in this case, the mixture was filtered.

- Clax 1-3: In this case, a sample was produced without the use of the butanone. So, the Igepal and the Gd_2O_3 were incorporated in MMA and then polymerized with the initiators of the company, skipping the mixing procedure. Also in this case, the reaction was carried out with standard values for temperature, pressure, and viscosity of the pre-polymer. The polymerization time was around 80 hours. Also in this case, the mixture was filtered.

- Clax 2-1: The Gd_2O_3 ($1\%_w$ with respect to MMA), was incorporated to 3 kg of MMA (at T=25°C). Then, the mixture was subjected to mechanical mixing and, after a few minutes, $0.1\%_w$ of surfactant was added. After, also a solution of 400 g of MMA with the secondary initiator was added one hour before the immission in the mold. In this case, a pre-polymer with the highest possible value of viscosity (1000 Centipoise) was transferred into a mold without any filtration process. The polymerization time was around 12 days.

- Clax 2-2: The procedure was quite similar to the latter (with the same amounts of Gd_2O_3 and surfactant), but in this very case it was decided to increase the amount of secondary initiator of the polymerization reaction. Since also in this case a pre-polymer with the highest value of viscosity was used, there was no filtering of the mixture.

- Clax 2-3: Also in this case, it was decided to use a high-viscosity pre-polymer but, in addition, it was used a cross-linking reagent (polyethylene glycol diacrylate, see structure formula in figure 6.2), whose purpose is to induce links between polymeric chains, increasing further the viscosity. The amounts of Gd_2O_3 and Igepal were left unaltered.

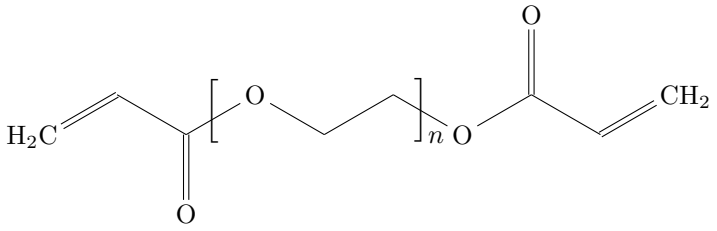

Figure 6.2 – Structure formula of polyethylene glycol diacrylate.

- Clax 2-4: In this case, a concentration of $0.85\%_w$ of Gd_2O_3 was used, while the Igepal concentration was kept at $0.1\%_w$. It was decided to use a pre-polymer with standard viscosity, filtering the whole mixture properly.

- Clax 2-5: At last, it was decided to use a high-conversion pre-polymer (that is a pre-polymer containing an amount between 16% and 18% of the final polymer, obtained by increasing the amount of the first initiator). This sample contains a Gd_2O_3 concentration of $0.85\%_w$ and a surfactant concentration once again of $0.1\%_w$. The viscosity, this time, was maintained at the standard level (400 Centipoise). Also a mercaptan (see structure formula reported in figure 6.3), was added, as a chain transfer.

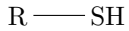

Figure 6.3 – Structure formula of a generic mercaptan.

In samples Clax 2-4 and Clax 2-5, smaller amounts of Gd_2O_3 NPs were used. This was due to a lack of enough raw material. The first three samples (Clax 1-1, Clax 1-2, and Clax 1-3) were produced at the end of 2021. Already starting from the visual inspection, it was possible to notice the sedimentation of the NPs on the bottom of the plates, in all three cases (see figure 6.4). The slabs were in any case characterized by the calcination technique, which confirmed what was observed through visual inspection.

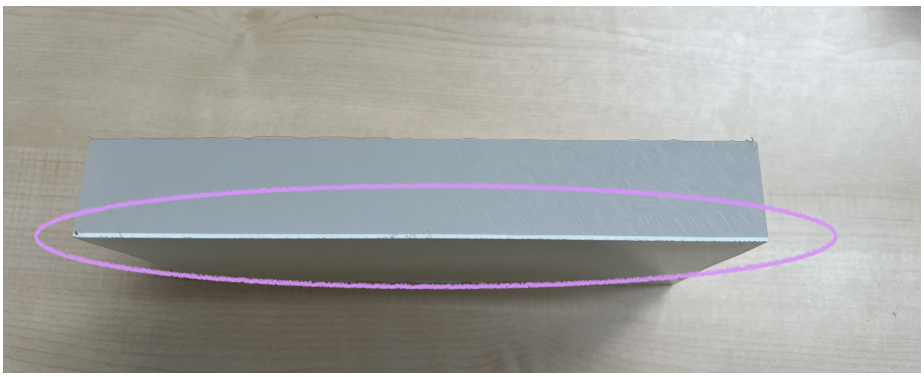

Figure 6.4 – Industrial sample Clax 1-1. The lavender oval shows the NPs sedimentation on the bottom of the sheet. This phenomenon happened equally also for Clax 1-2 and Clax 1-3.

The next five samples (Clax 2-1, Clax 2-2, Clax 2-3, Clax 2-4, and Clax 2-5) were produced in February 2022, in an autoclave, to set specific pressure and temperature values. The appearance of these plates was very different from those of the previous one. production batch: all five were apparently much more homogeneous and of a yellowish color towards the center (see figure 6.5). Clax

Figure 6.5 – Industrial samples Clax 1-1, Clax 1-2, Clax 1-3, and Clax 1-4. As can be seen, all have a yellowish color towards the center. On the side faces it is possible to notice the signs of the standard mechanical processes (not optimized for the experiment) that the company operates after production.

2-5 plate was not characterized, as it had bubbled during the curing process and, therefore, it was decided to exclude that procedure from our possible choices for the final production. The following paragraphs illustrate the characterizations carried out on the industrial samples, which retrace what was carried out on the laboratory scale samples (see chapter 4). As regards the choice of the methodology for the final production, following the characterizations it was decided to opt for what was done for the Clax 2-3 sample (therefore using the PEG diacrylate), since it was the only one completely free of mechanical defects (air bubbles formed during polymerization).

6.2 Characterization of industrial samples

First of all, it was decided to check the Gd_2O_3 uniformity distribution along the industrial scale samples, both to verify the compliance with the requirements of DarkSide-20k and to identify the most suitable method for the final production. Afterward, as for the second production lot, it was decided to check the uniformity of the samples also from a chemical point of view, and the thermal properties uniformity along the samples' thickness. Moreover, some HP-Ge screenings were performed on the materials, to check the radiopurity of the products. Finally, also some thermal and mechanical tests were carried out, to check the mechanical properties of the samples and their resistance to thermal stresses.

6.2.1 Gadolinium oxide distribution homogeneity

For what concerns the first samples lot, from each sample a piece was cut which was in turn divided into three parts, each about 1 cm thick.
As for the second batch, each portion was divided into six sections of about 2 cm each, as illustrated in figure 6.6.
The results of the calcinations are shown in table 6.2. As expected, the samples

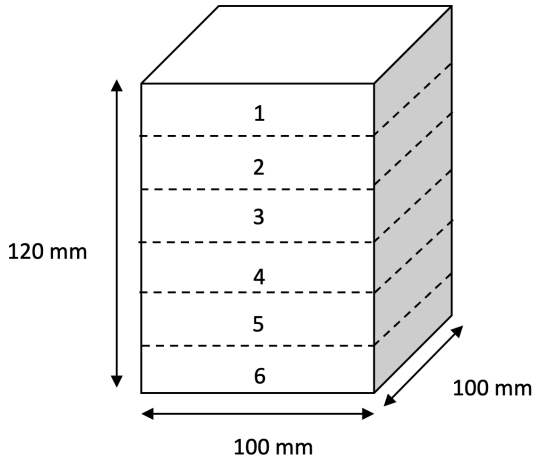

Figure 6.6 – Sectioning of the portions taken from the samples produced in the second lot.

from the first lot were completely inhomogeneous, all the NPs were sedimented on the bottom of the slab. As for the second lot samples, all of them look pretty homogeneous.

Sample	Section	Nominal Gd_2O_3 concentration [$\%_w$]	Measured Gd_2O_3 concentration [$\%_w$]
Clax 1-1	Section 1	1	0.019 ± 0.003
	Section 2	1	0.023 ± 0.003
	Section 3	1	2.588 ± 0.002
Clax 1-2	Section 1	1	0.048 ± 0.002
	Section 2	1	0.014 ± 0.004
	Section 3	1	3783 ± 0.004
Clax 1-3	Section 1	1	0.058 ± 0.002
	Section 2	1	0.020 ± 0.002
	Section 3	1	2.797 ± 0.002
Clax 2-1	Section 1	1	0.80 ± 0.07
	Section 2	1	0.85 ± 0.06
	Section 3	1	0.85 ± 0.07
	Section 4	1	0.85 ± 0.01
	Section 5	1	0.85 ± 0.02
	Section 6	1	0.85 ± 0.01
Clax 2-2	Section 1	1	0.90 ± 0.03
	Section 2	1	0.87 ± 0.05
	Section 3	1	0.87 ± 0.11
	Section 4	1	0.88 ± 0.05
	Section 5	1	0.88 ± 0.03
	Section 6	1	0.91 ± 0.02
Clax 2-3	Section 1	1	0.78 ± 0.04
	Section 2	1	0.84 ± 0.05
	Section 3	1	0.87 ± 0.06
	Section 4	1	0.88 ± 0.04
	Section 5	1	0.89 ± 0.04
	Section 6	1	0.77 ± 0.08
Clax 2-4	Section 1	0.8	0.46 ± 0.01
	Section 2	0.8	0.52 ± 0.04
	Section 3	0.8	0.52 ± 0.02
	Section 4	0.8	0.47 ± 0.03
	Section 5	0.8	0.60 ± 0.08
	Section 6	0.8	0.52 ± 0.01

Table 6.2 – Calcinations tests performed on each section of the company's samples. The samples coming from the first production lot (Clax 1-1, Clax 1-2, and Clax 1-3) were cut into 3 sections, since they were just 4 cm thick. All the other samples were cut into 6 sections because they were 12 cm thick. All results show a Gd_2O_3 concentration lower than that expected due to the presence of a submillimetric deposit which is much higher in the first lot of production.

The homogeneity of the slabs, therefore, meets the requirements of DarkSide-20k and is better illustrated in figure 6.7. As can be seen, the most homogeneous

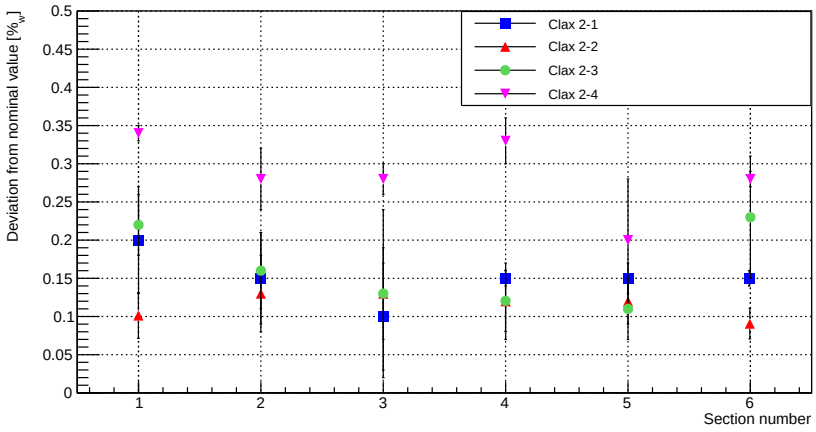

Figure 6.7 – Deviation from the nominal value in the concentration of Gd_2O_3 in the various sections of some industrial slabs subjected to calcination.

slab is Clax 2-2. However, the sample in question was inspected and some mechanical defects (bubbles) were found; therefore, although it was not the best in terms of uniformity, it was decided to opt for the recipe used to prepare the Clax 2-3 slab, as it was free from mechanical defects and in any case has satisfactory uniformity values.

6.2.2 Chemical properties uniformity

As a prototype of the final material, the most suitable candidate of the industrial samples was also subjected to infrared spectroscopy characterizations to verify the uniformity of the chemical composition (and properties) throughout the thickness of the sample itself. As mentioned above, the ideal candidate is the one called Clax 2-3, as it has no mechanical defects. Some sections obtained for the calcinations (see figure 6.6) were then analyzed with the same spectrophotometer used for the validation of the mixing procedure (see section 3.2). Figure 6.8 shows the IR spectra associated with the different sections analyzed. The three spectra present perfectly overlapping peaks, therefore the chemical properties remain the same along the thickness of the sample, in spite of the inhomogeneity of composition. It is important to underline that in this case, any intensity variations in the spectrum do not constitute quantitative measurements.

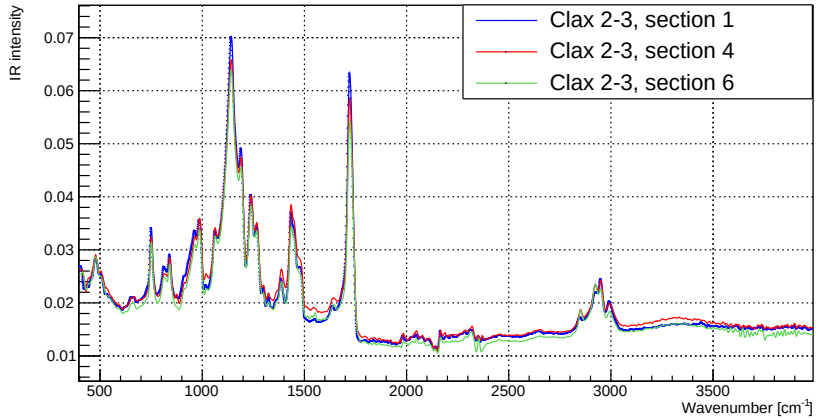

Figure 6.8 – IR spectra of three different sections of the sample Clax 2-3. Section 1 is the bottom part, section 4 is the middle part, and section 6 is the upper part.

6.2.3 Glass transition temperature measurements

As for the previous section, it was considered necessary to ensure that the samples exhibited comparable properties along the thickness of the samples themselves. This was also verified for the thermal properties and, in this case, for the T_g. Therefore, of the second series of tests in the company, two samples (Clax 2-2 and Clax 2-3, the most promising) were analyzed, in various sections, while the others (Clax 2-1 and Clax 2-4), they were analyzed in only one section (i.e. a central section). In figure 6.9 are reported the DSC curves performed on the best candidate, i.e. Clax 2-3. The DSC thermal ramps have been performed exactly according to the procedure used for laboratory samples, see section 4.2. Once again, the accuracy of the T_g values derives only from the sensitivity of the instrument's temperature sensors, but the systematic errors are not taken into consideration. As mentioned above, the uniformity of the T_g was also investigated in the sample called Clax 2-2. This sample, as observed in section 6.2.1, is the most homogeneous in the distribution of Gd_2O_3 NPs, but it is not our best candidate due to the presence of some mechanical defects. In any case, the DSC curves of some of its sections (the same investigated for the Clax 2-3 sample) are shown in figure 6.10. For what concerns the other samples of the second production lot, just one section was characterized (specifically section 3). Once again, the sample named Clax 2-5 was not characterized, since it presented a very high degree of defectiveness due to reboiling in the production phase.
All the results of the middle section of these four samples are reported in table 6.3. Ultimately, all the T_g measured in the various sections are comparable to each other. Anyway, these measured values are compatible with the typical range of the pure PMMA [80]: it is reasonable to conclude that the NPs (for

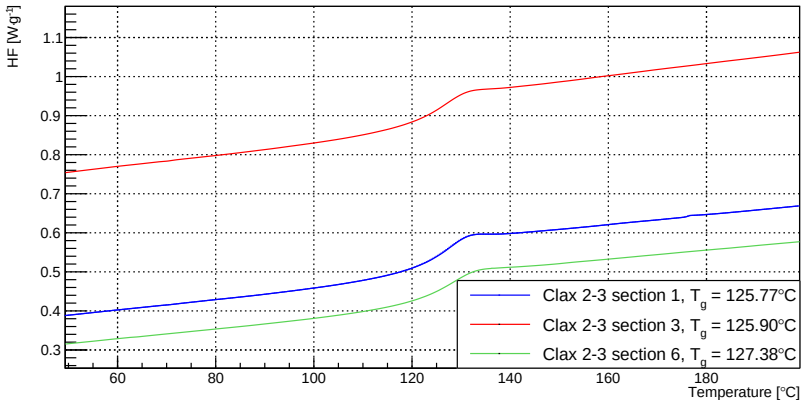

Figure 6.9 – DSC curves different sections of the sample Clax 2-3. Notice how the T_g variations are quite small, thus compatible along the sample's thickness.

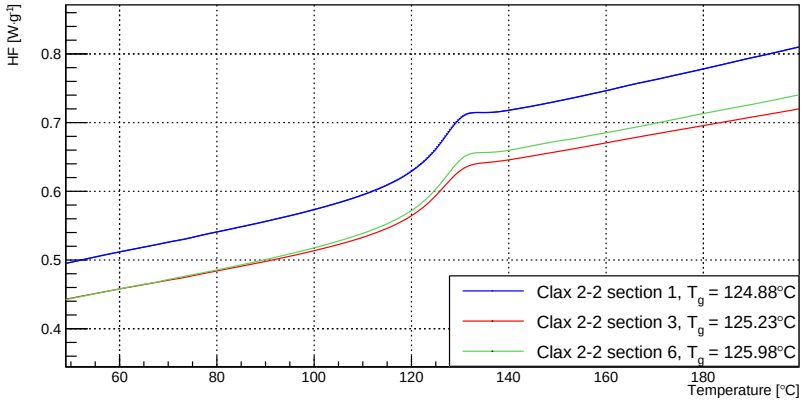

Figure 6.10 – DSC curves of sample Clax 2-2. Also in this case, the T_g variations are quite small

Sample	T_g [°C]
Clax 2-1	124.37
Clax 2-2	125.23
Clax 2-3	125.90
Clax 2-4	124.61

Table 6.3 – T_g values for the middle section of each sample produced in the industry during the first months of 2022.

these concentration values) do not affect the thermal properties of the composite material, as they are dominated strongly by PMMA.

6.2.4 Mechanical tests

Retracing what was done and illustrated in section 4.6.1, the industrial samples were subjected to mechanical tests to determine some properties such as Young's modulus, tensile stress, and thermal expansion coefficient.

Young Modulus

As in the other previous cases, the Clax 2-3 sample was characterized. From this sample various specimens were produced, with a thickness of about 1 mm, in order to carry out tensile tests. The results produced with these tests explored two different characteristics, namely:

1. Verify the effect of cryogenic tests on the mechanical properties of the sample, by comparing the stress-strain curve of a specimen subjected to cryogenic tests with that of a specimen not subjected to cryogenic tests.

2. Verify the influence of NPs on the mechanical properties of the composite material. This was roughly verified simply by comparing a sample of the Clax 2-3 sample with a sample obtained from one of the samples of the first production batch (in this case Clax 1-1), in a section where the concentration of Gd_2O_3 was approximately zero. This rather unusual method derives from the fact that the procedures adopted by the company to produce the material were quite unique, therefore it was not possible to obtain a sample of pure PMMA that had been subjected to the same procedure for making the comparison.

For what concerns the first point, the result is reported in figure 6.11. Two specimens were taken from the sample Clax 2-3 and labeled "Clax 2-3 a" and "Clax 2-3 b". After the annealing (performed as shown in the section 4.4), one specimen was subjected to a cooling cycle in LN_2 (Clax 2-3 a), while the other one didn't. Both specimens were then have been subjected to tensile tests. Figure 6.11 also reports Young's modulus values for both specimens and calculates as usual by performing a linear fit in the elastic region with the CERN toolkit ROOT. The Young's modulus values shown in the figure are compatible with the range of typical values for PMMA, therefore stresses induced by the cooling tests do not introduce significant variations for our application purposes.
For what concerns the second point, that is to verify any changes in the mechanical properties induced by the presence of NPs, results are reported in figure 6.12. As can be noticed, also in this case the values of the Young modulus of the two specimens are compatible.
In table 6.4 the tensile test results of all produced specimens are reported.

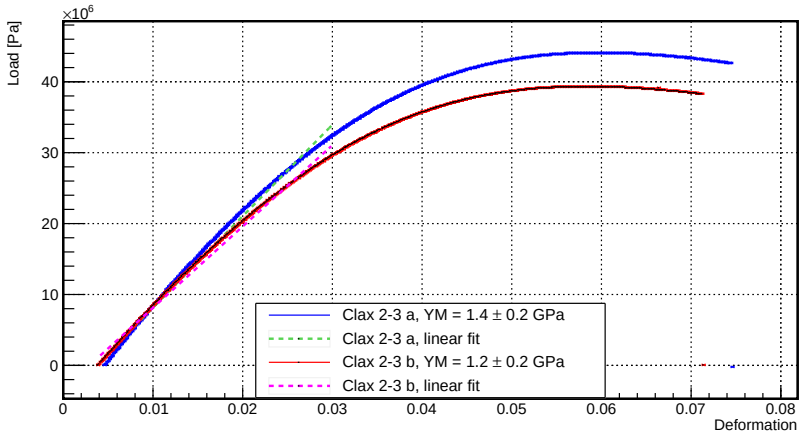

Figure 6.11 – Tensile tests on specimens taken from the Clax 2-3 sample.

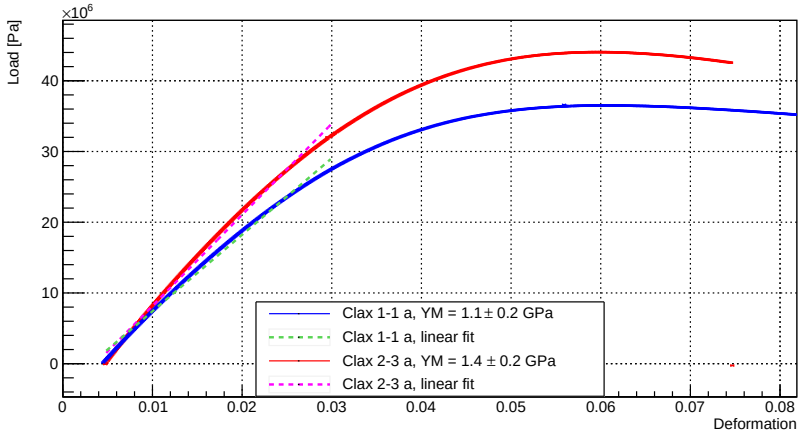

Figure 6.12 – Tensile tests on specimens from samples belonging to two different production lots: Clax 1-1 (the blue line) from the first production lot, Clax 2-3 from the second production lot (red line).

Thermal contraction

Given the structural role of the veto plates, it is necessary to know their thermal contraction coefficient and, moreover, the formulation of adequate mechanical tolerances to ensure the flatness of the anode, which rests on the plates. To calculate the thermal contraction coefficient, two methods were used: the first test consists in cooling a fairly homogeneous sample of PMMA doped with Gd_2O_3 in LN_2, which is then left to thermalize for a few hours. Then the dimensions of this sample are measured with a caliper, after having quickly extracted it from the cryogenic bath. The dimensions are then compared to those that had been measured at room temperature, prior to cooling. This measurement was made

Specimen	Young modulus [GPa]	Ultimate tensile strength [MPa]
Clax 1-1 a	1.1 ± 0.2	36.44 ± 0.05
Clax 1-1 b	1.2 ± 0.2	37.11 ± 0.05
Clax 1-2 a	1.2 ± 0.2	35.96 ± 0.05
Clax 1-2 b	1.2 ± 0.2	36.82 ± 0.05
Clax 1-3 a	1.1 ± 0.2	35.41 ± 0.05
Clax 1-3 b	1.3 ± 0.3	36.37 ± 0.05
Clax 2-3 a	1.4 ± 0.2	44.05 ± 0.05
Clax 2-3 b	1.2 ± 0.2	39.29 ± 0.04

Table 6.4 – Young modulus values for all the characterized specimens taken from the Clax samples.

on a parallelepiped taken from the Clax 2-3 industrial sample. All the faces of the parallelepiped were measured, along the two axes, as shown in figure 6.13. Then, the coefficient of linear thermal expansion (CLTE) was calculated

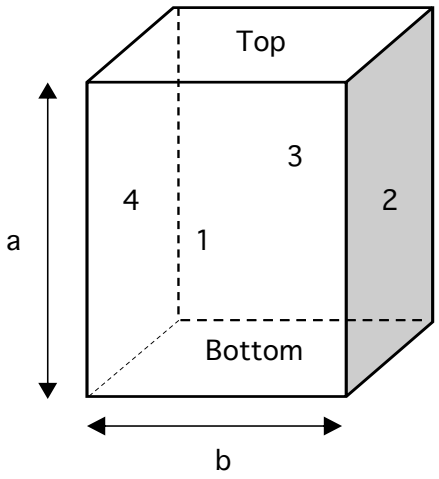

Figure 6.13 – Labeling of the faces of the sample for the thermal contraction measurement.

according to the equation 6.1.

$$\alpha_L = \frac{1}{L} \cdot \frac{dL}{dT} \tag{6.1}$$

The results are reported in table 6.5. After that, the average value of all the measurements was calculated to obtain an estimate of the contraction coefficient,

Face:	Side:	Lenght (T_{amb}) [mm]:	Lenght (T=LN_2) [mm]:	α_L [K^{-1}]:
Bottom	a	104.7	103.95	$(3.24 \pm 0.06)\cdot10^{-5}$
	b	107.53	106.62	$(3.83 \pm 0.06)\cdot10^{-5}$
Top	a	105.24	103.68	$(6.7 \pm 0.07)\cdot10^{-5}$
	b	107.58	106.43	$(4.84 \pm 0.07)\cdot10^{-5}$
1	a	117.86	116.24	$(6.22 \pm 0.07)\cdot10^{-5}$
2	a	117.88	116.37	$(5.80 \pm 0.07)\cdot10^{-5}$
3	a	117.81	116.64	$(4.49 \pm 0.06)\cdot10^{-5}$
4	a	117.87	116.62	$(4.80 \pm 0.06)\cdot10^{-5}$

Table 6.5 – Thermal contraction measurements on a specimen taken from the industrial sample Clax 2-3.

which is equal to (4.99 ± 0.02) K^{-1} 10^{-5}, in line with what is reported in the literature for the pure PMMA [102]. Following this preliminary test, more accurate measurements were performed to estimate the CLTE. These measurements were carried out by experts at the University of Bologna, where the shrinkage of some rectangular-based prism specimens in liquid nitrogen was measured. Thanks to the instrumentation (DMA 242E Artemis, operating in tensile deformation mode), it was possible to carry out more accurate measurements, without the need to extract the specimens from the cryogenic liquid. The measurement results are shown in figure 6.14. In the figure, it is possible to see the contraction

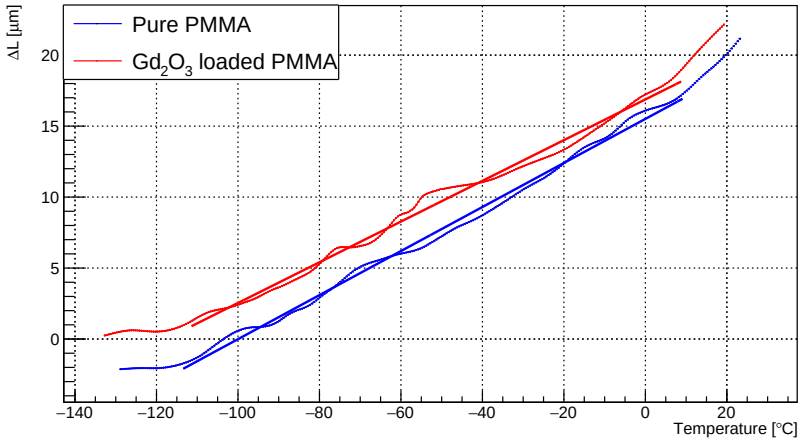

Figure 6.14 – CLTE measurement for two samples: one of pure PMMA (blue dots) and one of Gd_2O_3 doped PMMA, coming from industrial sample Clax 2-3. The two lines are the linear fits performed to calculate the CLTE.

of the sample versus the temperature for a pure PMMA sample and a Gd_2O_3 doped PMMA sample. For both samples, the data were linearly fitted using the CERN ROOT toolkit. The fit parameters of both curves are reported in table

6.6. Since in this case the fitted values didn't have associated errors, the ROOT

Sample	Slope [μm/°C]	Intercept [μm]
Pure PMMA	0.1547 ± 0.0007	15.47 ± 0.05
Gd_2O_3 loaded PMMA	0.1409 ± 0.0007	16.76 ± 0.05

Table 6.6 – Fit parameters of the curves shown in figure 6.14. The last column, NDf, is for the degrees of freedom of the fit.

software evaluated the fit parameters with an uncertainty calculated with a specific algorithm [103].
For this analysis, the systematics of measures are not taken into account, which would lead to larger error ranges.
Once the fit parameters have been calculated, it is possible to trace the CLTE using the formula reported in equation 6.2.

$$\text{CLTE} = \frac{S}{L_0} \tag{6.2}$$

Where S is the slope and L_0 is the initial length of the specimen, which in this case was equal to 4 mm. This leads to the CLTE values reported in table 6.7. The results obtained are also in this case compatible with the range for the pure

Sample	CLTE [°C^{-1}]
Pure PMMA	$(3.87 \pm 0.02) \cdot 10^{-5}$
Gd_2O_3 loaded PMMA	$(3.88 \pm 0.02) \cdot 10^{-5}$

Table 6.7 – CLTE values for a pure PMMA sample and a Gd_2O_3 loaded PMMA sample. As can be seen, the results are compatible.

PMMA CLTE reported in the literature. From the measurements carried out, it is therefore possible to conclude that the presence of the Gd_2O_3 NPs does not influence the thermo-mechanical properties of the polymeric matrix.

6.2.5 Measurement of resistance to cryogenic temperatures

As shown in section 4.4, also the industrial samples were subjected to a cooling test to test their resistance to thermal stresses. For this purpose, some portions were cut from the industrial sheets, for the formation of both macroscopic samples (10x10x12 cm^3 parallelepipeds) and thin slices for tensile tests (see section 6.2.4). In figure 6.15 are reported the cooling test on the parallelepipeds. The curves are quite similar to what is reported in section 4.4 for the laboratory-scale samples. For the tensile tests, some specimens were subjected to cooling tests, to verify the impact of the thermal stresses on the mechanical properties.

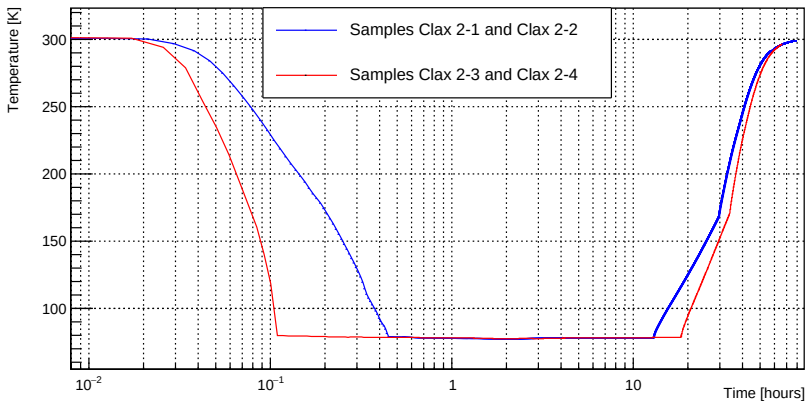

Figure 6.15 – Cooling tests on the samples. The cooling tests were performed with two samples at a time.

These samples have dimensions approximately equal to 60x15x1 mm^3. Despite the different sizes, none of the samples suffered obvious damage following cryogenic tests.

6.2.6 Radiopurity

As mentioned before, any component that is going to be used inside the DarkSide-20k detector must undergo a severe screening process. For what concerns our production procedure for the Veto sheets, the components are, basically:

- Starting monomer, MMA
- The Gd_2O_3 NPs, already screened (as shown in chapter5) and considered enough pure for our purposes
- The surfactant, whose purification strategy was illustrated in section 5.2
- Any additives, such as initiators, crosslinking agents, etc. used by industry

The liquid monomer coming from the industry was screened by the collaboration facilities with the ICP-MS technique. Results are reported in table 6.8. These

Element	Specific activity [mBq/kg]	Concentration [ppb]
Th	$<$0.041	$<$ 0.01
U	$<$0.12	$<$ 0.01

Table 6.8 – U and Th determination via Inductively Coupled Plasma Mass Spectrometer (ICP-MS) measurement on a MMA sample from Clax s.r.l. company.

results are preliminary and should be considered indicative since, due to the

lack of an adequate mass of the industrial sample, it was not possible to perform a HP-Ge screening on industrial MMA. It was therefore decided to take as a reference some HP-Ge screenings carried out on the finished samples (listed later in this section), whose activity contains the sum of the various contributions of each component, as well as a possible contribution of recontamination due to the industrial process (contact with surfaces that are not perfectly clean, the introduction of dust, contact with air, etc.).
The first sample screened belongs to the first production lot. Results are reported in table 6.9. It should be emphasized that these results refer to a sample

Isotope	A [mBq/kg]
^{235}U	< 0.80
^{238}U/^{234m}Pa	< 75
^{238}U/^{226}Ra	1.80 ± 0.27
^{232}Th/^{228}Ac	< 2.5
^{232}Th/^{228}Th	< 1.3
^{40}K	148 ± 16
^{137}Cs	< 0.54
^{60}Co	< 0.43

Table 6.9 – Screening performed with HP-Ge detector on Clax gadolinium loaded PMMA. The sample that has been screened is Clax 1-2.

obtained with a procedure that is not the definitive one and that the surfactant concentration in this sample is one order of magnitude higher than in the samples of the second production batch. From table 6.9, in fact, it is possible to notice that there is still a high activity due to ^{40}K, and this is due to the fact that this sample was produced with an amount of 1%$_w$ of not-purified surfactant at that time, for practical reasons. However, the amount of uranium (third line of the table) is higher than the sum of the components, therefore there is recontamination due to a not perfectly clean environment. So, in addition to the purification processes, it is necessary to perform the cleanliness of all the containers involved in the production. The final production procedure is shown in figure 6.16. Therefore, the containers that need to be cleaned are the mixing apparatus, where the Gd_2O_3, the Igepal, and some MMA are mixed together, the pre-polymerization vessel, the incorporation vessel (where the pre-polymer and the colloidal solution are incorporated) and the glass mold where the polymerization occurs. As regards the second batch of industrial production, table 6.10, shows the results of another screening, carried out on the industrial sample Clax 2-3, which represents the best candidate for the creation of veto sheets. As expected, the ^{40}K activity is reduced by a factor ten, in accordance with an order of magnitude reduction in surfactant concentration.

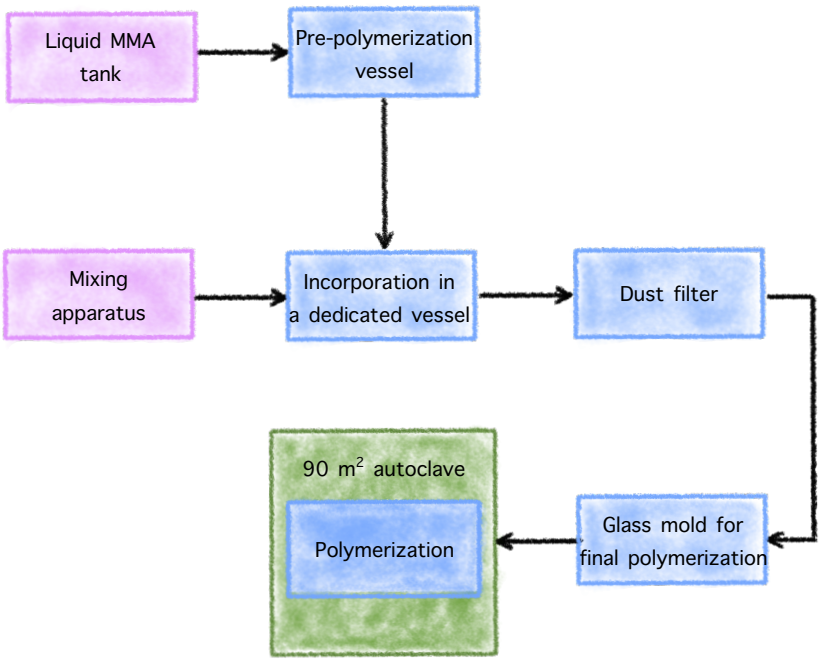

Figure 6.16 – Diagram of the production line at the Italian company Clax s.r.l.

Isotope	A [mBq/kg]
^{235}U	< 0.64
^{238}U/^{234m}Pa	< 17
^{238}U/^{226}Ra	< 0.26
^{238}U/^{234}Th	< 11
^{232}Th/^{228}Ra	0.4 ± 0.2
^{232}Th/^{228}Th	0.4 ± 0.2
^{40}K	14 ± 3
^{137}Cs	< 0.24

Table 6.10 – The HP-Ge screening of the best industrial sample, Clax 2-3, performed at LNGS facilities.

Chapter 7

Characterization of commercial organic scintillators in cryogenic environments

The aim of this thesis work is the study of different materials for applications in the new generation of detectors of rare event physics. In this context, in addition to the work carried out for the development of a neutron veto for the DarkSide-20k experiment, an activity has been carried out aimed at verifying the performance of some organic scintillators in cryogenic environments.
The use of organic scintillators is a well-established technique for particle detection. Thanks to the light yield of about 10^4 photons/MeV in case of energy released by an electron [104] and the possibility to realize them in different shapes, they could be used as particle taggers in different scenarios. One example is the use of these materials as scintillating optical fibers inside a liquid argon veto included in the GERDA experiment [105] and foreseen in the future LEGEND experiment [106]. Other applications in experimental physics range from the time of flight apparata [107] to calorimetry (like the ATLAS sampling calorimeter [108]). At the moment, the devices developed for the SuperNEMO experiment [109] are the state of the art in terms of radiopure organic scintillators. A subsequent upgrade in the experiments of rare events could lead to the total absence, in the experimental setup, of "passive" materials (i.e. without any particle detection function). For this purpose, one could therefore think of vetoes consisting of scintillating molecules dispersed in a polymeric matrix (therefore an organic scintillator).
The PESCE (Plastic Economic Scintillators in Cryogenic Environment) project,

financed by INFN for the years 2019, 2020, and 2021, aims to test commercial organic scintillators at cold (LN_2 and LHe), since to date, there is no information in the literature on the performance of these scintillators under these thermal conditions. The scintillators that were tested were purchased by the Eljen Technology company [110]. The main characteristics of these scintillators are reported in table 7.1. The scintillators are mainly made up of a polyvinyl

Scintillator	Anthracene [%]	Light yield [γ/1 MeV e^-]	Light attenuation length [cm]	Emission wavelenght [nm]
EJ-200	64	10000	380	425
EJ-208	60	9200	435	408
EJ-230	64	9700	120	391
EJ-240	41	6300	240	430
EJ-244	56	8600	270	434
EJ-248	60	9200	250	425

Table 7.1 – Main characteristics of the commercial organic scintillators studied during the PESCE project.

toluene (see the structure formula reported in figure 7.1) matrix with the addition of a scintillating molecule, namely anthracene (see structure formula in figure 7.2).

All of these scintillators had been characterized by the vendor in a thermal

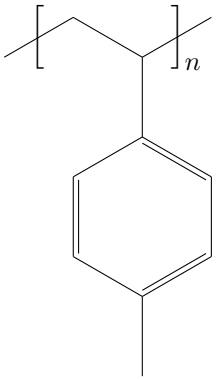

Figure 7.1 – Structure formula of polyvinyl toluene.

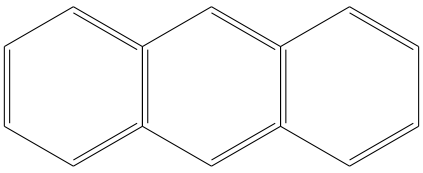

Figure 7.2 – Structure formula of anthracene.

range between -20°C and 60°C there were no data for lower temperatures. What was stated is that there were no changes in the light output from -60°C to 20°C.

7.1 Experimental set-up

The tests were conducted in a double-wall cryostat by Oxford Instruments, which was provided with a copper rod (cold finger) to place the scintillator in thermal contact with a cryogenic liquid bath. The vacuum was maintained within the cryostat walls with a rotary pump Leybold Scrollvac 18 plus (capable of bringing the pressure to 10^{-2} mbar), which was kept continuously running due to the high losses of the cryostat. The vacuum level was measured thanks to a Leybold Ionivac ITR200S meter read by the Leybold Graphix controller. The experimental set-up involved the use of two scintillators: one NaI crystal doped with Tl, by Scionix, 51B51/2M-E12", coupled with a PMT, and the other was the organic scintillator to be tested. The organic scintillator was coupled to a PMT (Philips XP2262B), and both the PMTs were connected to a digitizer (CAEN v1731). Some Pt-100 sensors and DT-670 diodes were installed to monitor the temperature both of the cold finger and of the surface of the organic scintillator under test. The temperature sensors were read and recorded through a LakeShore 218 temperature monitor or a Cryocon 18i in a different configuration of the slow monitoring system. To characterize the light yield of the scintillator, a 1.26 kBq ^{60}Co-based source was used, which emits two simultaneous γs, with energies of 1.17 MeV and 1.33 MeV, respectively (figure 7.3) [111]. The acquisition of the

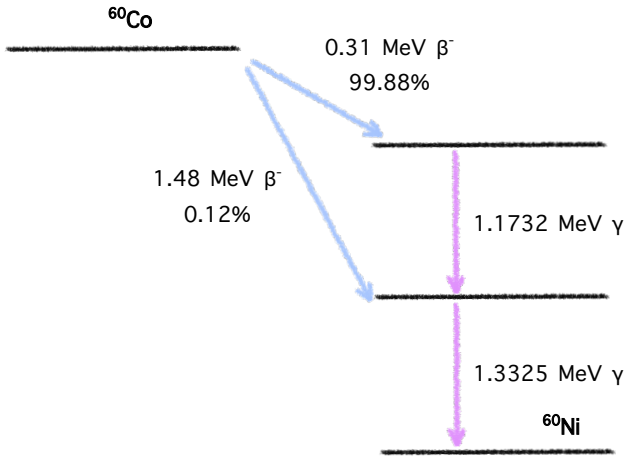

Figure 7.3 – Decay scheme of the ^{60}Co isotope.

signals of the two scintillators was carried out by triggering on the NaI signal: which means that if the signal detected by this scintillator reaches a certain amplitude threshold, an acquisition window of 8 μs was opened for the organic scintillator, which is long enough to identify the signal, the background noise level, and any accidental coincidences.
The signal of the two PMTs was then recorded as waveforms by a customized data acquisition system developed using LabView software [112]). Data files are transferred from a local computer to a scientific computation farm, where raw data has been reconstructed in the final file using the CERN ROOT [79] toolkit. The reconstructed file contains all the information needed for data analysis of the event (e.g. amplitude and charge) as well as slow monitoring parameters (e.g. temperature).
The scheme of the experimental set-up is illustrated in figure 7.4. The duration

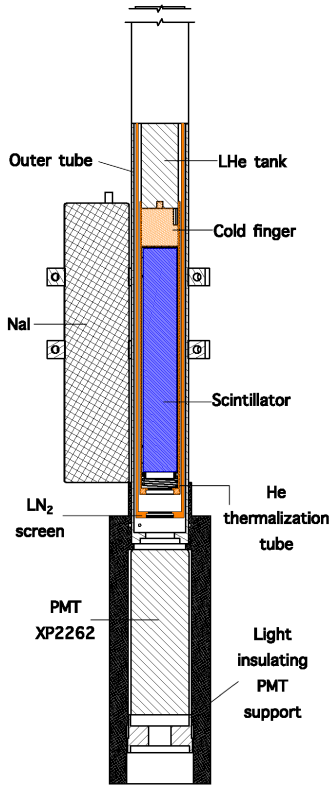

Figure 7.4 – Schematic of the components of a part of the experimental apparatus of PESCE. The cold finger is in direct contact both with the organic scintillator and with the cryogenic bath in the cryostat. On the NaI scintillator there is a dedicated PMT, as for the organic scintillator.

of cooling with cryogenic liquids is strictly dependent on the goodness of the

thermal coupling between the scintillator and the cold finger. In the first test, the cold finger was placed in contact with a Teflon layer, but this led to unsatisfactory results, as the scintillator reached temperatures close to those of liquid nitrogen in a rather long time (see blue curve in figure 7.5a).

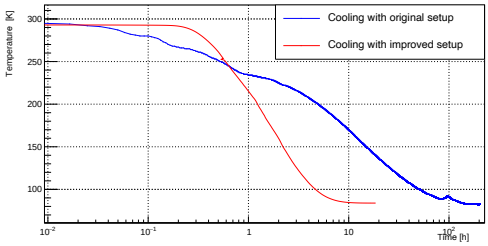

(a) Difference in cooling time between different thermal links.

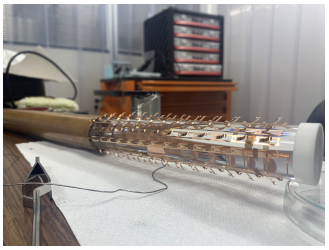

(b) Placing of copper-beryllium strings along the scintillator profile.

Figure 7.5 – Different cooling set-up for PESCE cooling data taking. Figure 7.5a shows the consistent difference in the cooling time between the two different set-ups. In figure 7.5b, instead, an example of the typical configuration of the lamellae on the organic scintillator is reported.

After that, the thermal coupling was optimized by thinning the Teflon layer and placing on the surface of the scintillator some copper-beryllium strings (see figure 7.5b) that favored thermalization. As can be seen from the red curve in figure 7.5a, the cooling time has been significantly reduced as a result of this upgrade.

7.2 Data taking

The light yield variation of each scintillator sample from ambient to cryogenic temperature has been studied by comparing spectra (i.e. the number of events recorded as a function of energy) acquired during different runs.

A typical example is reported in figure 7.6, where the spectra of the EJ-200 sample at room temperature are reported, with and without the radioactive source. Each spectrum is normalized to the total duration of the respective acquisition run. For reference, the single photoelectron region lies around 12 mV. Each spectrum is typically made up of three parts:

- a steep drop in the (0.00-0.01) V, due to electronic noise and accidental coincidences with dark counts.
- a shoulder in the region (0.01-0.05) V produced by the ^{60}Co source (absent in the spectrum with no source).
- a shoulder in the (0.05-0.5) V range, due to cosmic muons.

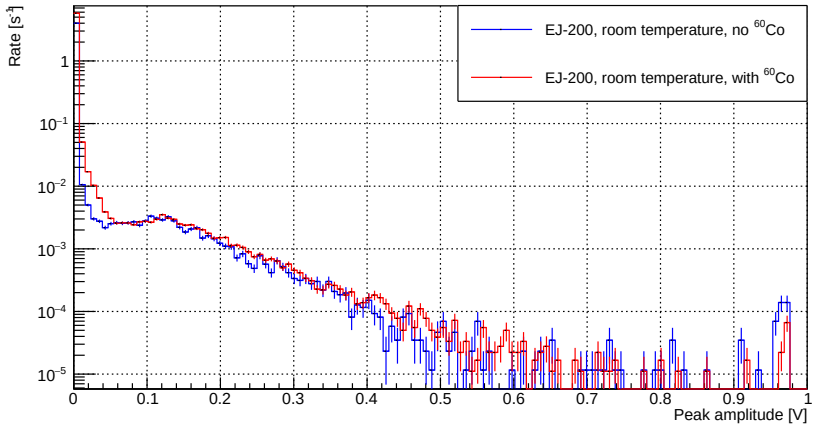

Figure 7.6 – A typical signal plot for the PESCE experiment for the EJ-200 scintillator. The blue curve represents the background: it was acquired without the ^{60}Co source, and this curve is characterized by fewer events with a low peak amplitude. The red curve, on the other hand, was acquired in the presence of the ^{60}Co source, and its effect is in fact visible via a low-energy shoulder, where the two curves are no longer superimposable. At high energies, in both cases, the contribution of the muons can be seen.

As it can be seen, the presence of the ^{60}Co source modifies the spectrum at low voltages. Therefore, any consideration on the scintillation efficiency was done evaluating the low energies. Once familiar with the study of the spectra, the cooling tests in LN_2 were made for all the scintillators (see section 7.2.1).

7.2.1 Tests in cryogenic environments

Cooling tests in LN_2 were made for all the scintillators in Table 7.1. The effect of the temperature on the rate of scintillation events was different for each scintillator, as shown in figure 7.7. This was expected, since they carry different concentrations of the scintillating molecule. In view of the results obtained cooling the scintillators in LN_2 (whose results are reported in section 7.4), it was decided to characterize in LHe the three scintillators that most of all showed a good light yield and a high light attenuation length at the same time.
The modulation of the attenuation length is a relevant parameter in the construction of an apparatus for the physics of rare events. A shining example is a study conducted by Legend-200 [113], which led to the creation of devices with an attenuation length of about 6 cm. To realize larger apparatuses it is advisable to modulate the attenuation length accordingly.
The chosen scintillators for this purpose are EJ-200, EJ-244, and EJ-248. The plots are illustrated in figure 7.8. Even at such low temperatures, no drastic decreases in efficiency are noted for these scintillators, since the curves relating

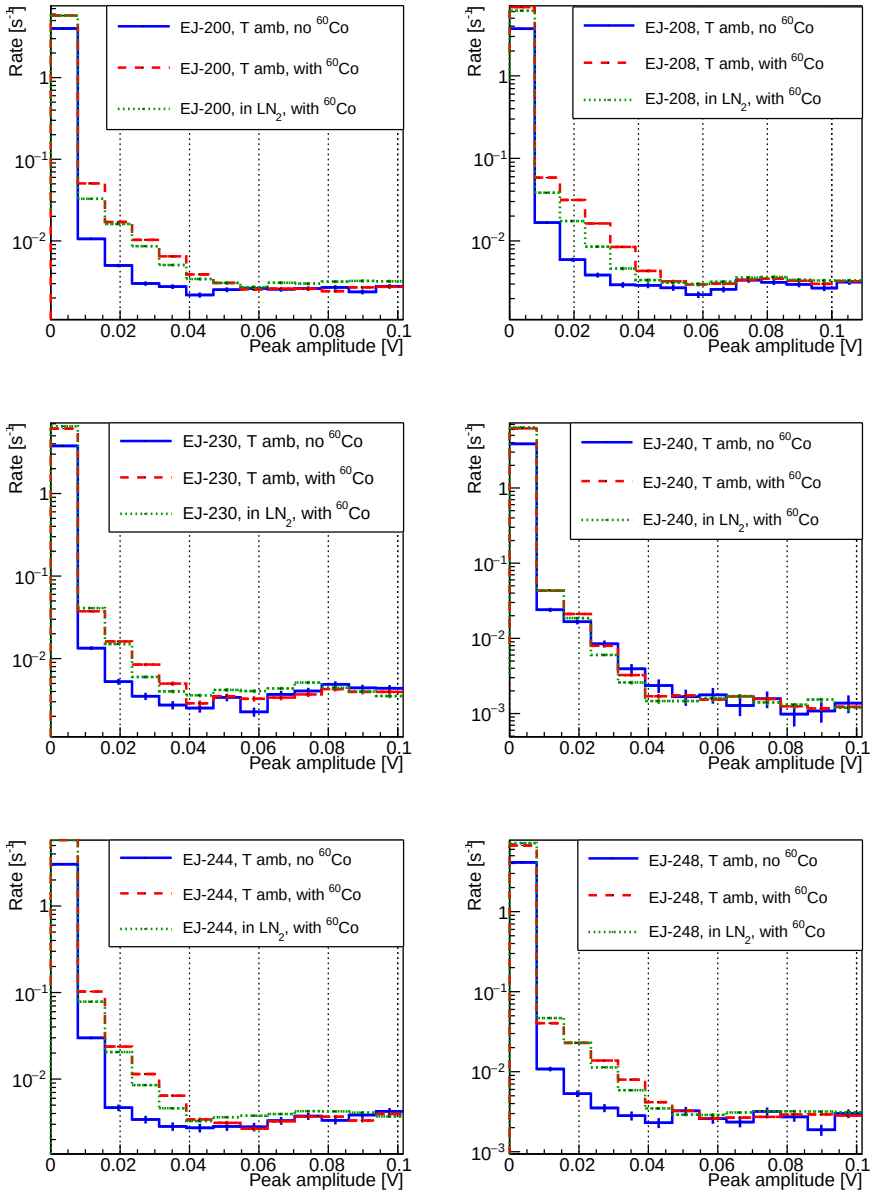

Figure 7.7 – Comparison of the efficiency of all scintillators at room temperature and at temperatures close to those of nitrogen liquefaction. The blue curve shows, for all devices, a run performed in the absence of the γ source at room temperature. The dashed red curve represents a run acquired at room temperature in the presence of the γ source. Finally, the green dotted curve shows a run in the presence of the γ source acquired in a liquid nitrogen environment.

to the acquisition at LHe do not seem to show variations compared to the data that were taken at LN_2 (dashed red and dotted green curves).

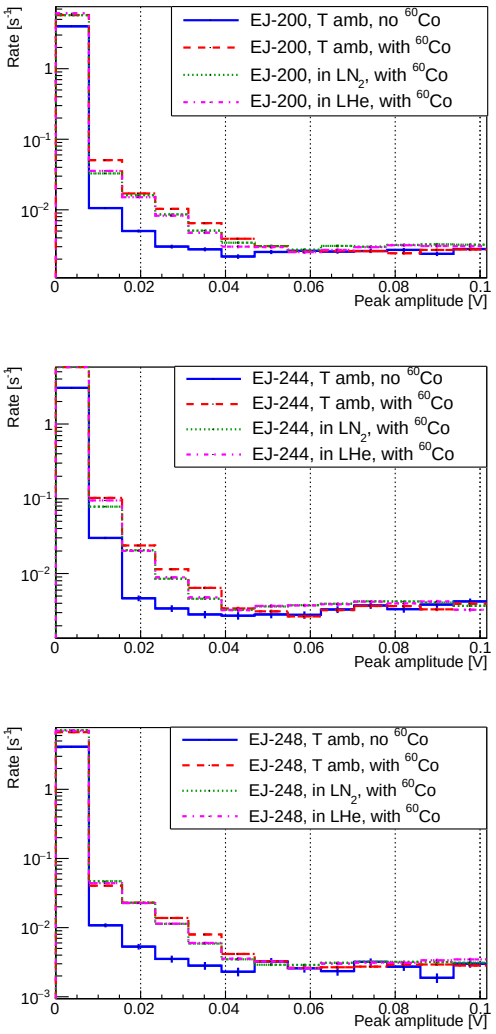

Figure 7.8 – Overview of the performances of the scintillators of EJ-200, E-J244, and EJ-248 at room temperature, in a liquid nitrogen environment, and in a liquid helium environment (dashed and dotted magenta curves).

A detailed analysis of scintillator performance at cryogenic temperatures is reported in section 7.5.

7.3 Organic scintillators synthesis

In order to gain more knowledge on this type of scintillator, attempts have also been made to synthesize scintillators consisting of a polymer matrix doped with a scintillating molecule in the laboratory. Thanks to the skills acquired during the R&D of gadolinium oxide for the DarkSide-20k experiment, tests were carried out with a PMMA matrix, since it is well-known that through MMA it is possible to achieve good radiopurity levels, and this would open the door to interesting applications in the physics of rare events, following what has already been achieved in the NEMO-3 experiment [114]. The scintillating molecules considered for these tests were anthracene, which is the molecule used by Eljen Technology, and naphthalene (structure formula reported in figure 7.9).
Rapid tests were carried out, which included:

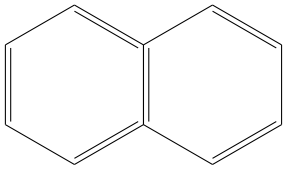

Figure 7.9 – Structure formula of naphthalene.

1. verify that the molecule in question was soluble in MMA for quantities comparable to those declared by Eljen Technology

2. polymerization of MMA additivated with the molecule with a different procedure than that developed for DarkSide-20k, which includes:

    - Dispersion of the molecule in the liquid monomer
    - Inducing polymerization with the addition of the initiator Luperox (used as secondary initiator in the polymerization procedure developed for DarkSide-20k.)

It has been found that anthracene, with concentrations between 1%$_w$ and 10%$_w$, is not soluble in MMA, while it shows greater solubility in other common organic solvents. As for naphthalene, on the other hand, it is soluble in MMA (samples with concentrations up to 30%$_w$ were prepared and polymerized). Following the polymerization attempts, homogeneous and transparent samples were obtained. This could pave the way for the fabrication and characterization of custom-made scintillators, which however goes beyond the scope of this thesis work.

7.4 Data analysis and conclusions

The goal of the data analysis was to quantify the light yield variation between ambient and cryogenic temperatures for each scintillator sample. Looking at the spectra reported in figures 7.7 and 7.8, it is possible to notice that at cryogenic temperatures the spectra of all scintillators look compressed with respect to the corresponding spectra at room temperature (see figure 7.10). The data analysis

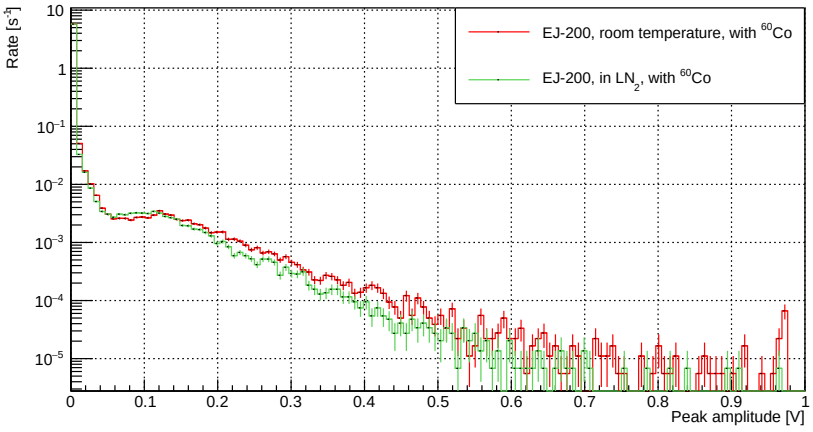

Figure 7.10 – Typical trend of a scintillator's light yield at room temperature and in LN_2. As can be seen, a sort of compression seems to happen between the two curves.

aims to quantify this compression factor (called α) for each scintillator, as a proxy variable for the light yield. The spectral form was modeled due to the radioactive source and the cosmic muons with an eight-degree polynomial:

$$\sum_{k=0}^{8} p_k x^k \tag{7.1}$$

The room temperature spectrum is then fitted with the polynomial, with the p_k coefficient left as free parameters of the fit. The spectral form at cryogenic temperatures is modeled with the same polynomial (including the p_k values fixed by the previous fit) except for two scaling factors as free parameters, one on the vertical axis N (to account for the different number of events) and one on the horizontal axis (α), which represents the relative change in light yield:

$$N \sum_{k=0}^{8} p_k \left(\frac{1}{\alpha} x\right)^k \tag{7.2}$$

The fit range is chosen by varying both the lower limit (between 0.01 and 0.03 V, with steps of 0.001 V) and the upper limit (between 0.1 and 0.3 V, with steps

Scintillator	α_{LN_2}	α_{LHe}
EJ-200	$0.90 \pm 0.01 \pm 0.05$	$0.90 \pm 0.01 \pm 0.05$
EJ-244	$0.89 \pm 0.01 \pm 0.01$	$0.93 \pm 0.01 \pm 0.03$
EJ-248	$0.89 \pm 0.01 \pm 0.01$	$0.91 \pm 0.01 \pm 0.01$
EJ-208	$0.83 \pm 0.01 \pm 0.02$	-
EJ-230	$0.81 \pm 0.01 \pm 0.04$	-
EJ-240	$0.90 \pm 0.01 \pm 0.02$	-

Table 7.2 – Evalutation of the α_{LN_2} and α_{LHe} factors for the tested commercial scintillators.

of 0.01 V) and selecting the fit with the smallest reduced χ^2. The distribution of the results of the less performant fits is used to estimate the systematic error on the α parameter. The α factors for the liquid nitrogen (α_{LN_2}) coolings were evaluated for all the scintillators, while the factors for liquid helium (α_{LHe}) were evaluated only for scintillators that have been characterized at those temperatures, namely EJ-200, EJ-244 and EJ-248. The results are reported in table 7.2. It is also possible to see from the table that the α factors for LN_2 and LHe are substantially identical, meaning that there is no significant change in light yield. The scintillator that seems the most promising is EJ-200, which, in fact, carries a higher concentration of the scintillating molecule. In conclusion, it was possible to characterize these scintillators in a cryogenic environment, obtaining a satisfactory light yield even at low temperatures and the efficiency comparisons of the scintillators are consistent with what was expected.

7.5 Discussion

The scintillator EJ-200 is the most efficient: the light emitted during the scintillation process does not seem to be affected by the temperature decrease, as it can be seen from the cooling plots in figure 7.8 and from its α_{LN_2} and α_{LHe} values. In fact, as seen from the spectra, the curves at room temperature, in LN_2 and LHe almost superimposable. This was expected because this is the scintillator that carries the highest concentration of scintillating dye (see table 7.1).
The scintillator EJ-208 shows instead a clear decrease in light collection efficiency when the system is at temperatures close to that of liquid nitrogen. This trend is easily visible macroscopically from figure 7.7, and is confirmed by the α_{LN_2} value in table 7.2.
For what concerns the scintillator EJ-230, no significant differences are noted in the scintillation efficiency at different temperatures macroscopically, but the α_{LN_2} value is quite low (compared with the one of a good candidate such as EJ200). Moreover, as reported in table 7.1, this is the worst sample in terms of

nominal light attenuation length.
The scintillator EJ-240 has the worst behavior: even though the α_{LN_2} is equal to the one of the scintillator EJ-200, from figure 7.7 can be seen that, macroscopically, the effect of the ^{60}Co is slightly noticeable (see blue and red dashed curves). On the other hand, this scintillator has the lowest concentration of scintillating molecule, as reported in table 7.1, explaining this behavior.
As for the scintillator EJ-244, there is a reduction in terms of efficiency between the spectrum at room temperature and the cold spectrum (curves dashed red and dotted green in figure 7.8), but, unlike the previous case, the effect of the source is well visible. Its α_{LN_2} and α_{LHe} values (tab 7.2) are also very similar to the ones of the best candidate, EJ-200. Moreover, the light attenuation length (table 7.1) is quite high (second only to the EJ-200 scintillator). At last, the scintillator EJ-248 shows just a small decrease in light-gathering efficiency in the region between 0.02 V and 0.04 V (figure 7.8). Since it is a very small reduction (also confirmed by its α_{LN_2} and α_{LHe} values in table 7.2), this device is still considered one of the best candidates.
In conclusion, the α factors for LN_2 and LHe are practically unchanged for the tested devices. The scintillator that seemed most promising is EJ-200, which carries a higher concentration of the scintillating molecule, and this is consistent with the goodness of the α factor. In conclusion, it was possible to characterize these scintillators in a cryogenic environment, obtaining a more than satisfactory light yield even at low temperatures and the efficiency comparisons of the scintillators are consistent with what was expected.
As regards the synthesis tests in the laboratory, further tests are necessary to verify the scintillation efficiency of these devices, but in the first instance, a synthesis methodology was found that leads to the production of homogeneous and defect-free samples (to a first visual inspection) with rather high concentrations of the scintillating molecule.

Conclusions

The aim of this work was the development of innovative materials for the future generation of rare-events physics experiments such as those aiming at observing interactions by dark matter particles with ordinary matter. In particular, for the DarkSide-20k experiment, my contribution consisted in the realization of a hybrid material, or polymethyl methacrylate loaded with gadolinium oxide, suitable to moderate and capture neutrons and thus to be ideal for building the neutron veto for the DarkSide-20k experiment. The realization of mechanical components of such large dimensions represented a challenge and an outlet for future applications in the physics of rare events. This research work led to the identification of correct mixing and polymerization strategies and, subsequently, to the realization of industrial prototypes considered satisfactory for the requirements of the experiment, both from the point of view of homogeneity in the distribution of the oxide (section 6.2.1), both in terms of mechanical properties of the composite material (section 6.2.4), and in terms of radiopurity (section 6.2.6). Concerning this last part, each component of the developed procedure was subjected to strict radiopurity checks by DarkSide collaborators, and the analyzes conducted (chapter 5) led to the development of a purification technique for non-ionic surfactants. commercial from alkali metal ions (in our case potassium, section 5.2). The final materials were then subjected to a final screening which determined their suitability for the experiment. Finally, the resistance of these materials to cryogenic temperatures was tested, reproducing the environment that will be found within the DarkSide experiment, and it was observed that even in the most extreme conditions the materials do not show damage induced by cooling. Following the numerous characterizations, therefore, it is possible to conclude that the material developed during this thesis meets all the requirements, and it is possible to use it in the physics of rare events. This R&D work led to the filing of a patent on the hybrid material (application number 102021000028130), currently awaiting approval.
Regarding the characterization of organic scintillators for the PESCE experiment, what was observed with the laboratory tests demonstrates the possibility of using these devices in cryogenic environments, since the light yield does not undergo too significant variations with respect to what is observed at room temperature.

Tests in liquid nitrogen and liquid helium were successfully completed, thanks to an adequate thermal coupling system. Furthermore, the first tests conducted in the laboratory have shown that there is the possibility of creating devices that can meet the radiopurity criteria that require experiments of rare events.
The work carried out in this thesis paves the way for the use of an innovative material in future rare event physics experiments (as regards Gd-loaded PMMA), and for the development of innovative devices for application in aforementioned experiments. The development of innovative materials is of fundamental importance for this field of research, to minimize the number of passive materials and allow an adequate background check. The results achieved are very promising.

Appendix A

Other activities

During my Ph.D. work, I also contributed to other projects: the commissioning of the OARPAF (Osservatorio Astronomico Regionale Parco Antola Comune di Fascia) and the MOONLIght (MOON seismicity detection with ultra-stable Laser Interferometry) project.
For what concerns the OARPAF, my contribution consisted in the characterization of the newly-acquired CCD (Charge-Coupled devices) devices before their installation at the Observatory, and in the realization of a pipeline software for the manipulation of scientific images (taken during the observation sessions), in FITS format [115], by taking into account all instrumental backgrounds introduced by the solid-state detectors that constitute the sensitive part of the CCD.
In addition, the MOONLIght project was a signature approved for the two-year period 2020-2021 by INFN for the ICSM (Instrument Characterisation for Space Missions) project. The idea consisted of the development of optical fibers crossed by ultra-stable laser light for the detection of seismic events on space sites of interest to ESA. My contribution mainly consisted in providing guidance on the choice of the best materials to be used for the realization of optical fibers by using a Monte-Carlo software that simulates the extreme conditions found in space environments (such as intense cosmic ray bombardment), through the Geant4 [116] tool of the CERN.

Ringraziamenti

Il primo ringraziamento va al prof. Tosi, che mi ha presa per mano quando ero una matricola ignara di cosa fosse una derivata, e mi ha accompagnata per tutti questi anni. Il secondo va a Gemma, una relatrice in grado di impedire che un'intera collaborazione collassi mentre lucida piastrelle di ardesia nel suo giardino. Un ringraziamento anche al prof. Marco Pallavicini, coordinatore del gruppo, che ho incontrato due sole volte nella vita, ma che sono state sufficienti a stravolgere tutto ciò che pensavo di sapere sul mio futuro e sulla ricerca.

Grazie a tutta L202: Stefano (che mi ci ha trascinata dentro), Coppe, Matteo R., Matteo V., Ilaria, Silvia, Alice, Giuliano (grazie al quale ho capito che non esista problema che non si possa risolvere con una cravatta e una flangia), Roberto, Massimo, Sergio, Lea.

Un grazie in particolare ad Alessio, che mi ha seguita passo passo, cercando di insegnarmi quando occorra essere "spannometrici" e quando essere estremamente precisi, e spesso occorre farlo contemporaneamente. Grazie per avermi fatto toccare le vette del disagio quando mi hai detto di aver misurato la tua spanna per sapere esattamente come misurare le cose con le mani. Grazie per aver rivisto il tuo modo di spiegare, per aver padroneggiato (non senza il mio aiuto) la "scienza cafona" e per aver sopportato i miei squilibri mentre tentavo di capire come diavolo funzionasse un TCanvas. Grazie per avermi mandato 20 volte la catena di decadimento del ^{238}U. Grazie per avermi insegnato a "fittare istogrammi al volo". Grazie per esserti preoccupato del mio futuro e, soprattutto, grazie di non avermi uccisa quando ho confessato di essere estranea al concetto di trigger.

Bianca, tu richiedevi un ringraziamento a parte. Se dovessi tentare di mettere per iscritto tutto ciò che penso, probabilmente dovrei scrivere un'altra tesi. So che ti imbarazzerai, ma non mi importa. Ci siamo incontrate durante una pandemia, io mi sentivo abbastanza persa. Poi sei arrivata tu, con un entusiamo, una preparazione, una curiosità e una voglia di fare davvero incredibili. Sei stata semplicemente straordinaria, e sei la versione migliore di ciò che potrei

mai ambire a diventare. Mi hai insegnato tutto, a partire dalle mie timide domande in laboratorio (“ma come si rivela la materia oscura?”, “come funziona DarkSide?”, “cos’è una TPC?”), fino ai transfer di azoto liquido. Ogni momento passato in laboratorio con te, anche i più faticosi (si vedano i test viscosimetrici, i becker che quasi esplodono quando il butanone bolle, i DLS e le cuvette che improvvisamente cambiano stato di aggregazione) è stato incredibile, istruttivo e a tratti tragicomico. Sei sicuramente la persona più preparata e meritevole che conosca (in qualsiasi ambito, e infatti un po’ ti odio), e sei sicuramente stata uno dei lati migliori di tutto il dottorato. Mi mancherà terribilmente commentare ogni meeting con te in diretta. Mi aspetto di vederti spokesperson quanto prima, o magari presidente del consiglio.

Grazie a tutta la mia famiglia, per il sostegno e l’affetto. Grazie a Zorba, immancabile valvola di sfogo.

Grazie a Vittoria, che riesce sempre a riportarmi a quando eravamo delle liceali con molte speranze e con le vertebre schiacciate dal peso dei dizionari. Grazie per comprendere ciò che penso ancora prima che lo faccia io.

Grazie a Chiara, che ho conosciuto tra queste mura. Una delle persone più in gamba e con la schiena più a pezzi che questi dipartimenti abbiano avuto l’onore di ospitare

Grazie a Tommaso, che durante tutto questo travagliato percorso ha sempre scelto di starmi accanto.

References

[1] T. Masaharu, *et al.* Review of particle physics. *Phys. Rev. D*, 98:030001, Aug 2018. doi:10.1103/PhysRevD.98.030001.

[2] V. Rubin. The rotation of spiral galaxies. *Science*, 220(4604):1339–1344, 1983. doi:1126/science.220.4604.1339.

[3] B. Apurba *et al.* Atomic Hydrogen in Star-forming Galaxies at Intermediate Redshifts. *ApJL*, 882, September 2019. doi:10.3847/2041-8213/ab3656.

[4] Y. Sofue and V. Rubin. Rotation curves of Spiral Galaxies. *Annual Review of Astronomy and Astrophysics*, 39(1):137–174, sep 2001. doi:1146/annurev.astro.39.1.137.

[5] J. Wambsganss. Gravitational lensing in astronomy. *Living Reviews in Relativity*, 1(1), nov 1998. doi:12942/lrr-1998-12.

[6] M. Meneghetti *et al.* An excess of small-scale gravitational lenses observed in galaxy clusters. *Science*, 369(6509):1347–1351, sep 2020. doi:1126/science.aax5164.

[7] G. Bertone. *Particle Dark Matter: Observations, Models and Searches*. Cambridge University Press, 2010. doi:1017/CBO9780511770739.

[8] D. Boulware and S. Deser. Classical general relativity derived from quantum gravity. *Annals of Physics*, 89(1):193–240, 1975. URL: https://www.sciencedirect.com/science/article/pii/0003491675903024, doi:https://doi.org/10.1016/0003-4916(75)90302-4.

[9] Planck collaboration. Planck 2018 results. I. overview and the cosmological legacy of Planck. *Astronomy & Astrophysics*, 641:A1, Sep 2020. URL: https://doi.org/10.1051%2F0004-6361%2F201833880, doi:1051/0004-6361/201833880.

[10] European Space Agency. Planck's view of the cosmic microwave background. URL: https://www.esa.int/ESA_Multimedia/Images/2018/07/Planck_s_view_of_the_cosmic_microwave_background.

[11] G. Bertone and T. Tait. A new era in the search for dark matter. *Nature*, 562(7725):51–56, oct 2018. doi:1038/s41586-018-0542-z.

[12] T. Kibble. The standard model of particle physics. *European Review*, 23(1):36–44, 2015. doi:10.1017/S1062798714000520.

[13] J. Billard, *et al.* Direct detection of dark matter – APPEC committee report, 2021. doi:10.1088/1361-6633/ac5754.

[14] Borexino Collaboration. Measurements of extremely low radioactivity levels in Borexino. 18(1):1–25, aug 2002. doi:1016/s0927-6505(01)00179-7.

[15] G. D'Imperio. Dark matter search with the SABRE experiment, jan 2020. doi:10.1088/1742-6596/1342/1/012060.

[16] C. Alduino *et al.*, jul 2018. URL: https://dx.doi.org/10.1088/1742-6596/1056/1/012009, doi:10.1088/1742-6596/1056/1/012009.

[17] L. Baudis. Wimp dark matter direct-detection searches in noble gases. *Physics of the Dark Universe*, 4:50–59, 2014. DARK TAUP2013. URL: https://www.sciencedirect.com/science/article/pii/S2212686414000223, doi:https://doi.org/10.1016/j.dark.2014.07.001.

[18] H J Hilke. Time projection chambers. *Reports on Progress in Physics*, 73(11):116201, oct 2010. doi:10.1088/0034-4885/73/11/116201.

[19] Clevios f et data sheet. URL: https://www.heraeus.com/media/media/hep/documents_hec/data_sheets_hep/Clevios_F_ET.pdf.

[20] R. Santorelli, *et al.* Spectroscopic analysis of the gaseous argon scintillation with a wavelength sensitive particle detector. *The European Physical Journal C*, 81(7), jul 2021. doi:1140/epjc/s10052-021-09375-3.

[21] 3MT™Enhanced Specular Reflector (ESR). URL: https://multimedia.3m.com/mws/media/13892480/application-guide-for-esr.pdf.

[22] M. Bonesini *et al.* Detection of vacuum ultraviolet light by means of sipm for high energy physics experiments. *Nuclear Instruments and Methods in Physics Research Section A: Accelerators, Spectrometers, Detectors and Associated Equipment*, 912:235–237, 2018. New Developments In Photodetection 2017. doi:https://doi.org/10.1016/j.nima.2017.11.063.

[23] D. S. Akerib, *et al.* Snowmass2021 cosmic frontier dark matter direct detection to the neutrino fog, 2022. URL: https://arxiv.org/abs/2203.08084, doi:10.48550/ARXIV.2203.08084.

[24] LZ collaboration. First dark matter search results from the LUX-ZEPLIN (LZ) experiment, 2022. doi:48550/ARXIV.2207.03764.

[25] Xenon collaboration. Search for inelastic scattering of WIMP dark matter in XENON1T. *Physical Review D*, 103(6), mar 2021. doi:1103/physrevd.103.063028.

[26] Xenon collaboration. Dark matter search results from a one ton-year exposure of XENON1T. *Physical Review Letters*, 121(11), sep 2018. doi:1103/physrevlett.121.111302.

[27] Xenon collaboration. Projected WIMP sensitivity of the XENONnT dark matter experiment. *Journal of Cosmology and Astroparticle Physics*, 2020(11):031–031, nov 2020. doi:1088/1475-7516/2020/11/031.

[28] DarkSide collaboration. Light yield in DarkSide-10: A prototype two-phase argon TPC for dark matter searches. *Astroparticle Physics*, 49:44–51, sep 2013. doi:1016/j.astropartphys.2013.08.004.

[29] V.P. Zrelov. *Cherenkov radiation in high-energy physics*. U.S. Atomic Energy Commission. AEC-tr-7099. Jerusalem, Israel Program for Scientific Translations, 1970.

[30] DarkSide collaboration. DarkSide-50 532-day dark matter search with low-radioactivity argon. *Physical Review D*, 98(10), nov 2018. doi:1103/physrevd.98.102006.

[31] N. Canci. Long term operation with the DarkSide-50 detector. *Journal of Instrumentation*, 15(03):C03026, mar 2020. doi:10.1088/1748-0221/15/03/C03026.

[32] DEAP-3600 Collaboration. First results from the DEAP-3600 dark matter search with argon at snolab. *Phys. Rev. Lett.*, 121:071801, Aug 2018. doi:10.1103/PhysRevLett.121.071801.

[33] E. Aprile, *et al. Noble Gas Detectors*. Wiley-VCH Verlag GmbH & Co. KGaA, 2006.

[34] J. Atwood. Fluorescent sensors for biological metal ions. In *Comprehensive Supramolecular Chemistry II*, pages 295–317. Elsevier, Oxford, 2017. doi:https://doi.org/10.1016/B978-0-12-409547-2.12612-5.

[35] M. Akashi-Ronquest, *et al.* Triplet lifetime in gaseous argon. *The European Physical Journal A*, 55(10), oct 2019. doi:1140/epja/i2019-12867-2.

[36] B. Bottino. *Dark matter search with liquid argon in DarkSide: results with scientific and technological prototypes*. 2019.

[37] DarkSide collaboration. CALIS—a CALibration insertion system for the DarkSide-50 dark matter search experiment. *Journal of Instrumentation*, 12(12):T12004–T12004, dec 2017. doi:1088/1748-0221/12/12/t12004.

[38] E. Hogenbirk, *et al.* Precision measurements of the scintillation pulse shape for low-energy recoils in liquid xenon. *Journal of Instrumentation*, 13(05):P05016–P05016, may 2018. doi:1088/1748-0221/13/05/p05016.

[39] R. Saldanha, *et al.* Cosmogenic production of ^{39}Ar and ^{37}Ar in argon. *Physical Review C*, 100(2), aug 2019. doi:1103/physrevc.100.024608.

[40] P. Benetti *et al.* Measurement of the specific activity of ^{39}Ar in natural argon. *Nuclear Instruments and Methods in Physics Research Section A: Accelerators, Spectrometers, Detectors and Associated Equipment*, 574(1):83–88, apr 2007. doi:10.1016/j.nima.2007.01.106.

[41] J. Kostensalo, *et al.* Spectral shapes of forbidden argon decays as background component for rare-event searches. *Journal of Physics G: Nuclear and Particle Physics*, 45(2):025202, dec 2017. doi:1088/1361-6471/aa958e.

[42] DarkSide Collaboration. Results from the first use of low radioactivity argon in a dark matter search. *Phys. Rev. D*, 93:081101, Apr 2016. doi:10.1103/PhysRevD.93.081101.

[43] DarkSide Collaboration. Darkside-50: status of the detector and results. *PoS*, page 225, 2016. doi:10.22323/1.282.0225.

[44] V. Pesudo and the DarkSide-20k Collaboration. Measurement of the underground argon radiopurity for dark matter direct searches. *Journal of Physics: Conference Series*, 2156(1):012043, dec 2021. doi:10.1088/1742-6596/2156/1/012043.

[45] DarkSide collaboration. Separating ^{39}Ar from ^{40}Ar by cryogenic distillation with Aria for dark-matter searches. *The European Physical Journal C*, 81(4), apr 2021. doi:1140/epjc/s10052-021-09121-9.

[46] DarkSide collaboration. The DarkSide-20k technical design report, 2021.

[47] M. F. L'Annunziata. *Handbook of Radioactivity Analysis*. Elsevier Inc., 2012. doi:https://doi.org/10.1016/C2009-0-64509-8.

[48] J. Dobson, *et al.* Ultra-low background mass spectrometry for rare-event searches. *Nuclear Instruments and Methods in Physics Research Section A:*

Accelerators, Spectrometers, Detectors and Associated Equipment, 879:25–30, 2018. doi:https://doi.org/10.1016/j.nima.2017.10.014.

[49] M. Amman. High purity germanium based radiation detectors with segmented amorphous semiconductor electrical contacts: Fabrication procedures, 2022. doi:48550/ARXIV.2006.05471.

[50] N. Sethy, *et al.* A review of radio chemical analysis and estimation of 210po in soil matrices. *Journal of Radiation Research and Applied Sciences*, 8(4):590–596, 2015. doi:https://doi.org/10.1016/j.jrras.2015.07.001.

[51] W. R. Leo. *Techniques for nuclear and particle physics experiments: a how-to approach; 2nd ed.* Springer, Berlin, 1994. doi:1007/978-3-642-57920-2.

[52] V. Kudryavtsev, *et al.* Neutron production in (α,n) reactions. *Nuclear Instruments and Methods in Physics Research Section A: Accelerators, Spectrometers, Detectors and Associated Equipment*, 972:164095, 2020. doi:10.1016/j.nima.2020.164095.

[53] Borexino Collaboration. Modulations of the cosmic muon signal in ten years of borexino data. *Journal of Cosmology and Astroparticle Physics*, 2019:046–046, 02 2019. doi:1088/1475-7516/2019/02/046.

[54] M. Nurazila, H. Yazid, and M. Harun. Neutron attenuation and mechanical properties of polymer composites filled with boron carbide particles. *IOP Conference Series: Materials Science and Engineering*, 785:012005, 05 2020. doi:10.1088/1757-899X/785/1/012005.

[55] Lenin E. Cevallos-Robalino, Gonzalo F. García-Fernández, Alfredo Lorente, Eduardo Gallego, Hector Rene Vega-Carrillo, and Karen A. Guzmán-Garcia. Design by monte carlo method of a thermal neutron device using a 241am/9be source and high-density polyethylene moderator. *Applied Radiation and Isotopes*, 151:150–156, 2019. doi:https://doi.org/10.1016/j.apradiso.2019.05.040.

[56] Hans Th. J. Steiger. Design, Status and Physics Potential of JUNO. *PoS*, DISCRETE2020-2021:086, 2022. arXiv:2203.14087, doi:10.22323/1.405.0086.

[57] P. A. Amaudruz et al. First results from the DEAP-3600 dark matter search with argon at SNOLAB. *Phys. Rev. Lett.*, 121(7):071801, 2018. arXiv:1707.08042, doi:10.1103/PhysRevLett.121.071801.

[58] International Nuclear Data Committee. Thermal neutron capture cross sections resonance integrals and G-factors. *International Atomic Energy Agency*, 2003.

[59] S. Alameri and A. Alkaabi. Nuclear reactor technology development and utilization. Woodhead Publishing Series in Energy, pages 27–60. Woodhead Publishing, 2020. doi:https://doi.org/10.1016/B978-0-12-818483-7.00001-9.

[60] J. Lim, *et al.* Microstructure and fracture property of 1A grade duplex stainless steel with the addition of gadolinium. *Journal of Korea Foundry Society*, 36:24–31, 02 2016. doi:7777/jkfs.2016.36.1.24.

[61] H. E. Haber and L. S. Haskins. Supersymmetric theory and models. *Anticipating the Next Discoveries in Particle Physics*, 2018. doi:10.1142/9789813233348_0006.

[62] Shin-etsu chemical co. URL: https://www.shinetsu.co.jp/en/.

[63] National Center for Biotechnology Information. PubChem compound summary for CID 4559504, Gadolinium 4-hydroxypent-3-en-2-one. URL: https://pubchem.ncbi.nlm.nih.gov/compound/4559504.

[64] National Center for Biotechnology Information. PubChem compound summary for CID129866908, Gadolinium methacrylate. URL: https://pubchem.ncbi.nlm.nih.gov/compound/Gadolinium-methacrylate.

[65] National Center for Biotechnology Information. PubChem compound summary for CID 159427, Gadolinium(III) oxide. URL: https://pubchem.ncbi.nlm.nih.gov/compound/Gadolinium_III_-oxide.

[66] T. Tsuzuki *et al.* Mechanochemical synthesis of gadolinium oxide nanoparticles. *Nanostructured Materials*, 11(1):125–131, 1999. doi:https://doi.org/10.1016/S0965-9773(99)00025-2.

[67] J.L. Bridot *et al.* Hybrid gadolinium oxide nanoparticles: multimodal contrast agents for in vivo imaging. *Journal of the American Chemical Society*, 129(16):5076–5084, 2007.

[68] A. Rivera, *et al.* Detection of thermal neutrons using gadolinium-oxide-based nanocrystals. *Proceedings of SPIE - The International Society for Optical Engineering*, 8018, 04 2011. doi:1117/12.883646.

[69] S. Jorice, *et al.* Homogeneous dispersion of gadolinium oxide nanoparticles into a non-aqueous-based polymer by two surface treatments. *J Nanopart Res*, 13:2417–2428, 06 2011. doi:1007/s11051-010-0129-6.

[70] A. Colombo, *et al.* Nanoparticle-doped large area PMMA plates with controlled optical diffusion. *J. Mater. Chem. C*, 1:2927–2934, 2013. doi:10.1039/C3TC00767G.

[71] S. Sambhudevan, B. Shankar, S. Appukuttan, and K. Joseph. Evaluation of kinetics and transport mechanism of solvents through natural rubber composites containing organically modified gadolinium oxide. *Plastics, Rubber and Composites*, 45(5):216–223, 2016. doi:10.1080/14658011.2016.1165904.

[72] D. Boulerba and A. Zoukel. Poly(methyl methacrylate)/sio2 nanocomposites: Effects of the molecular interaction strength on thermal properties. *Polymers and Polymer Composites*, 29(9_suppl):S49–S56, 2021. doi:10.1177/0967391120985710.

[73] C. Jillings and DEAP Collaboration. Control of contamination of radon-daughters in the DEAP-3600 acrylic vessel. *AIP Conference Proceedings*, 1549(1):86–89, 2013. doi:10.1063/1.4818082.

[74] C. M. Nantais. *Radiopurity measurement of acrylic for the DEAP-3600 dark matter experiment*. 2014.

[75] Merck co. doi:https://www.merck.com.

[76] *et al.* P.K. Vallittu. Effect of polymerization temperature and time on the residual monomer content of denture base polymers. *Eur J Oral Sci.*, 1998. doi:10.1046/j.0909-8836.1998.eos106109.x.PMID:9527360.

[77] Philip Nising. High-temperature radical polymerization of methyl methacrylate in a continuous pilot scale process. 01 2006. doi:10.5075/epfl-thesis-3460.

[78] Chemistry LibreTexts. Basic stages of a radical chain reaction. URL: https://chem.libretexts.org/Bookshelves/Organic_Chemistry/Book%3A_Radical_Reactions_of_Carbohydrates_(Binkley)/I%3A_Structure_and_Reactivity_of_Carbohydrate__Radicals/02%3A_Chain_Reactions/II._Basic_Stages_of_a_Radical_Chain_Reaction.

[79] Root data analysis framework. URL: https://root.cern/about/.

[80] T. Hongxiang, *et al.* High glass transition temperatures of Poly(methyl methacrylate) prepared by free radical initiators. *Journal of Polymer Science Part A-polymer Chemistry - J POLYM SCI A-POLYM CHEM*, 47:315–317, 01 2009. doi:1002/pola.23154.

[81] G. Höhne, *et al. Differential Scanning Calorimetry*. Springer-Verlag Berlin Heidelberg, 1996.

[82] Mettler Toledo. URL: https://www.mt.com/int/en/home.html.

[83] M. Kumar Singh and A. Singh. *Chapter 9 - Thermal characterization of materials using differential scanning calorimeter*. The Textile Institute Book Series. Woodhead Publishing, 2022. doi:https://doi.org/10.1016/B978-0-12-823986-5.00006-3.

[84] J. Ahmed. *Glass Transition and Phase Transitions in Food and Biological Materials*. John Wiley & Sons Ltd, 2017. doi:10.1002/9781118935682.

[85] Properties of PMMA, 2018. URL: https://polymerdatabase.com/polymers/\polymethylmethacrylate.html.

[86] J.D. Menczel and R.B. Prime. *Thermal Analysis of Polymers: Fundamentals and Applications*. Wiley, 2009.

[87] R.J. Brook. Calcination. In *Concise Encyclopedia of Advanced Ceramic Materials*, pages 49–51. Pergamon, Oxford, 1991. doi:https://doi.org/10.1016/B978-0-08-034720-2.50023-X.

[88] DEAP collaboration. Design and construction of the DEAP-3600 dark matter detector. *Astroparticle Physics*, 108:1–23, mar 2019. doi:1016/j.astropartphys.2018.09.006.

[89] S. G. Sevim *et al.* Comparison tests for the determination of the viscosity values of reference liquids by capillary viscometers and stabinger viscometer SVM 3001. *Int. J. Metrol. Qual. Eng.*, 9:7, 2018. doi:1051/ijmqe/2018004.

[90] D. Pawcenis, *et al.* Mark–Houwink–Sakurada coefficients determination for molar mass of silk fibroin from viscometric results. sec-malls approach. *RSC Adv.*, 6:38071–38078, 2016. URL: http://dx.doi.org/10.1039/C6RA00871B, doi:10.1039/C6RA00871B.

[91] J.E. Mark. *Polymer Data Handbook*. Oxford University Press, 1999. URL: https://books.google.it/books?id=qFi5QgAACAAJ.

[92] S. Agrawal, *et al.* Investigation of thermo-mechanical properties of PMMA, 2010. doi:1063/1.3466571.

[93] N. Fourches and M. Zielińska and Gabriel Charles. High purity germanium: From gamma-ray detection to dark matter subterranean detectors. In Basim A. Almayah, editor, *Use of Gamma Radiation Techniques in Peaceful Applications*, chapter 5. IntechOpen, Rijeka, 2019. doi:5772/intechopen.82864.

[94] J. Carter, *et al.* Production of 40Ar by an overlooked mode of 40K decay with implications for K-Ar geochronology. *Geochronology, 2, 355–365*, 2020. doi:https://doi.org/10.5194/gchron-2-355-2020.

[95] Q. He. Radioactivity abundance in simulation. 2011. URL: http://kirkmcd.princeton.edu/dayabay/He/Radioactivity.pdf.

[96] A. Ridha. *Determination of Radionuclides Concentrations in Construction Materials Used in Iraq*. PhD thesis, 01 2013. doi:10.13140/RG.2.1.3815.0640.

[97] B. A. Masry, *et al.* Modeling and equilibrium studies on the recovery of praseodymium (III), dysprosium (III) and yttrium (III) using acidic cation exchange resin. *BMC Chemistry*, 2022. doi:1186/s13065-022-00830-0.

[98] M. E. Ginn and C. L. Church. New columnar and mixed-bed ion exchange methods for surfactant analysis and purification. *Analytical Chemistry*, 31(4):551–555, 1959. doi:1021/ac50164a028.

[99] DonChamp acrylic co.,ltde. URL: https://donchampacrylic.en.ecplaza.net.

[100] The JUNO collaboration. Juno physics and detector. *Progress in Particle and Nuclear Physics*, 123:103927, 2022. doi:https://doi.org/10.1016/j.ppnp.2021.103927.

[101] Clax s.r.l. URL: https://www.claxitalia.com.

[102] T. A. Osswald, *et al. International Plastics Handbook*. Hanser Publishers, Munich, 2006.

[103] URL: https://root.cern.ch/doc/master/classTGraph.html#aa978c8ee0162e661eae795f6f3a35589.

[104] Ł. Kapłon and G. Moskal. Blue-emitting polystyrene scintillators for plastic scintillation dosimetry. *Bio-Algorithms and Med-Systems*, 17(3):191–197, 2021. doi:10.1515/bams-2021-0088.

[105] M. Agostini, *et al.* Upgrade for Phase II of the Gerda experiment. *The European Physical Journal C*, 78, 11 2017. doi:10.1140/epjc/s10052-018-5812-2.

[106] M. Schwarz, *et al.* Liquid argon instrumentation and monitoring in legend-200. *EPJ Web of Conferences*, 253:11014, 01 2021. doi:10.1051/epjconf/202125311014.

[107] J. Berdugo. Latest Results of the Alpha Magnetic Spectrometer on the International Space Station. *Moscow Univ. Phys. Bull.*, 77(2):71–82, 2022. doi:10.3103/S0027134922020126.

[108] Martin Aleksa and Marcella Diemoz. Discussion on the electromagnetic calorimeters of atlas and cms. *Nuclear Instruments and Methods in Physics Research Section A: Accelerators, Spectrometers, Detectors and Associated Equipment*, 732:442–450, 2013. Vienna Conference on Instrumentation 2013. doi:https://doi.org/10.1016/j.nima.2013.05.195.

[109] A. Barabash (on behalf of the NEMO Collaboration). NEMO 3 double beta decay experiment: Latest results. *Journal of Physics: Conference Series*, 173(1):012008, jun 2009. doi:10.1088/1742-6596/173/1/012008.

[110] Eljen technology. doi:https://eljentechnology.com.

[111] E. Browne and J.K. Tuli. Nuclear data sheets for A = 60. *Nuclear Data Sheets*, 114(12):1849–2022, 2013. URL: https://doi.org/10.1016/j.nds.2013.11.002.

[112] Labview, by national instruments. URL: https://www.ni.com/it-it/shop/labview.html.

[113] L. Manzanillas, *et al.* Optical properties of low background PEN structural components for the Legend-200 experiment. *Journal of Instrumentation*, 17(09):P09007, sep 2022. doi:10.1088/1748-0221/17/09/p09007.

[114] M. Bongrand. Latest NEMO-3 results and status of SuperNEMO, 2015. 13th International Conference on Topics in Astroparticle and Underground Physics, TAUP 2013. doi:https://doi.org/10.1016/j.phpro.2014.12.034.

[115] Fits format. URL: https://www.loc.gov/preservation/digital/formats/fdd/fdd000317.shtml.

[116] Geant4 toolkit. URL: https://geant4.web.cern.ch.